OSTEOPROGENITOR CELL ADHESION AND GROWTH ON THE BIOACTIVE SILICON NITRIDE SURFACE FOR CRANIOFACIAL IMPLANTS APPLICATIONS

by

KAMAL AWAD

THESIS

Submitted in Partial Fulfillment of the Requirements for the Degree

Master of Science in Materials Science and Engineering at

The University of Texas at Arlington

May 2018

Arlington, Texas

Supervising Committee:

Pranesh B. Aswath, Supervising Professor

Venu Varanasi

Yaowu Hao

Bryan J. McEntire

Acknowledgements

The author wishes to express his deep appreciation and gratitude to Dr. Pranesh B. Aswath, Professor of Materials Science and Engineering at UTA, for his kind supervision, encouragement, and critical comments during the preparation of this thesis. Also, my deep gratitude and thanks to Dr. Venu Varanasi, Assistant Professor, Biomedical Sciences at Texas A&M, for his continuous encouragement, constructive comments, and suggestions to accomplish this project.

Deep thanks are also extended to Dr. Yaowu Hao, Materials Science and Engineering at UTA, and Dr. Bryan J. McEntire, Chief Technology Officer at Amedica Corporation, for being on my committee and being so encouraging and cordial.

I am also thankful to my colleagues Dr. Felipe Monte, Neelam Ahuja, and Ami Shah for being supportive and sharing their knowledge throughout my research.

My sincere acknowledgment to Dr Jeichao Jiang and David Yen for the all the support and training at the CCMB facility. My deepest words of appreciation to Beth and Natalie for helping through all the official matters and for their good wishes through all two years of my graduate studies.

Deep thanks are also extended to Fulbright, AMIDEAST, and the Egyptian government for the financial support during these two years through Fulbright scholarships. Also, sincere acknowledgment to the National Research Centre in Egypt.

Last but not least, my deep gratitude is due to my parents and my lovely wife for being very supportive and encouraging throughout my endeavor in the USA and my new area of expertise.

April 2018

Abstract

OSTEOPROGENITOR CELL ADHESION AND GROWTH ON THE BIOACTIVE SILICON NITRIDE SURFACE FOR CRANIOFACIAL IMPLANTS APPLICATIONS

Kamal Awad, MS

The University of Texas at Arlington, 2018

Supervising Professor: Pranesh B. Aswath

As a novel biomaterial, silicon nitride (Si_3N_4) has been used for orthopedic and spinal fusion applications. Its ability to promote continuity for structural support of missing bone, by in/on bone growth, gives it advantageous properties and potential for mandibular and craniofacial reconstruction applications. Yet, the surface properties of this material and its effect on the osteogenic properties have not been fully realized. Thus, the aim of this study was to evidently investigate the surface properties of the bioactive Si_3N_4 that enhance the calvarial osteoblasts cell adhesion, growth, and differentiation when compared to conventional implant materials such as titanium (Ti) and polyetheretherketone (PEEK).

This study tests the hypothesis that silicon nitride induces the nucleation of hydroxyapatite (HA) crystals and enhances the formation of biominerals on its surfaces in cell-free environments and in presence of osteoprogenitor cells as well. Comprehensive studies of the bare surface properties, HA and biomineral formations, and cell culture studies of osteoprogenitor cells were conducted. We present the results of surface properties that enhance the formation of biomineral and osteoprogenitor responses as compared to traditionally used Ti and PEEK. X-ray Absorbance Near Edge Structure Analysis (XANES) indicated the presence of Si-Si, Si-O, and Si-N bonding, which suggested random mixing of

these bonding structures. Atomic Force Microscopy (AFM), and optical and stylus profilometry successfully assessed the morphological features and the roughness parameters of the surfaces. The Sessile drop technique was used to study the surfaces' wettability, and the resultant contact angles were used to calculate the surface energy of each material. FT-IR and Raman spectroscopy were used to characterize mineral formations on the surface of all samples before and after in vitro studies. Each material was imaged for its respective surface morphology using an Ultra HR-SEM, and the elemental composition was determined by the energy-dispersive x-ray spectroscopy (EDS). X-ray diffraction was used to investigate the HA formation on sample surfaces after 7 days of immersion in α-MEM. Meanwhile, murine calvarial MC3T3-E1 osteoblast in vitro cell studies and quantitative polymerase chain reaction will illustrate the enhancing nature of silicon nitride to promote osteogenesis. Furthermore, comprehensive study of the extracellular matrix (ECM) deposition was conducted after 30 and 60 days of the MC3T3-E1 osteoblast in vitro cell culture. Our study concludes and illustrates the ability of silicon nitride to promote rapid hydroxyapatite formation in cell-free environments and induce rapid osteoblast adhesion, growth, and dense ECM deposition compared to the conventional implant materials (Ti) and (PEEK).

Keywords: Silicon nitride; craniofacial implants; hydroxyapatite nucleation; hydroxyproline; amide surface formation; matrix deposition.

Table of Contents

List of Illustrations

List of Tables

CHAPTER 1

GENERAL OVERVIEW

A recent market overview of bone grafts and substitutes procedures reported $2.4 billion in 2015, and this value is expected to reach $3.4 billion by 2022; furthermore, globally 4 million bone grafting procedures and nearly 600,000 in the USA are performed every year [1] . Within the bone grafts and substitutes market, craniomaxillofacial implants have become an important branch that is controlled by several factors. It is now generally accepted that an increase in the number of road accidents, trauma cases, the rate of congenital facial deformities, as well as, invasive reconstruction surgeries, and technological advancements increase the demand of craniomaxillofacial implants procedures [2].

Over the years, bone grafting involved the use of allografts, transplanted from a donor of the same species, and xenografts, transplanted from a donor of different species. On the one hand, the rejection rate of allograft and xenograft procedures became high due to ethical issues and religious affiliations [3]. A recent study has explored that 20 % of patients refuse the allograft under any circumstances [3]. On the other hand, polymers, ceramics, metals, and biomaterial grafts provide a reasonable solution for the current debates about the allografts and xenografts. Although, these biocompatible bone grafts do not face the issues of rejection from the host, reduce the implant failure, and enhance the rate of bone formation [1] [2], they still have minor issues and drawbacks.

To date, the vast majority of the work in craniofacial reconstruction has focused on polyether ether ketone (PEEK), and titanium (Ti) as more widely employed implant materials. Due to its biocompatibility, low elastic modulus close to the bone, colorlessness, resistance to simulated in vivo degradation, and inert nature, PEEK is used in a number of

orthopedic applications such as spinal fusion cages, trauma, and arthroplasty [4] [5]. Despite decades of research on PEEK, its use has been less than satisfactory due to its increasingly apparent limitations. PEEK's fundamental flaw is its lack of bioactivity which prevents any adequate biological or mechanical integration with bone. Its smoothness, poor wettability, and low surface energy limit osteoblastic differentiation and bone regeneration [6][7][8][9]. As a result, recent observations reported that PEEK's osseointegration is not always a straightforward biological process [4].

Titanium and titanium aluminum vanadium (Ti6Al4V) alloys have also been used in orthopedic, dental, skeletal, spine fusion procedures, and craniofacial reconstruction applications [6][10][11]. Due to its biocompatibility and inherent ability to osteointegrate, Ti implants have been selected in various orthopedic applications for many decades [10][11]. On the other hand, stress shielding effect, aseptic loosening [12][13][14], poor long-term stability, absence of antioxidant effects [15], and prolonged healing time remain as critical issues for Ti implants. Indeed, the previous issues and limitations make the use of PEEK and Ti implants for craniofacial reconstruction and orthopedic applications less than optimal for bone healing. Therefore, the use of an implant material in which its surface induces rapid osteoprogenitor growth is desirable.

Non-oxide silicon nitride (Si_3N_4) ceramic has a unique combination of material properties such as high strength and fracture toughness, low wear properties, inherent phase stability, low friction coefficient, hydrophilicity, and biocompatibility[16][17]. Furthermore, this relatively new bioactive Si_3N_4 has shown improved osteoconductivity, cytocompatibility, and biomineralization comparable to the non-stoichiometric natural hydroxyapatite[18][19]. These features make it a material of interest for orthopedic applications such as craniofacial and dental procedures[17][20]. In 2008, Si_3N_4 has been approved by the US FDA and EU regulatory agencies for intervertebral spacers implantation in cervical and

thoracolumbar spine stabilization[21]. Recent studies have indicated bioactive Si_3N_4 enhances biomineralization as well as the osteogenic differentiation of mesenchymal and osteoblast cells when compared to Ti and PEEK[10][16][18][22][23][24][25]. This was attributed to many facts related to the nature of bioactive Si_3N_4, including its hydrophilicity, surface chemistry with strong electronegative surface sites, that promoted cell attachment and migration when compared to HA, Ti, or PEEK [17][18][26].

1.1 Motivation for the Research

Due to the increase in the rejection rate of allografts and xenografts procedures, the need of synthetic biocompatible bone grafts for orthopedic applications has been increased. Furthermore, the drawbacks and limitations of the current implant materials (Ti, PEEK) for craniofacial reconstruction and orthopedic applications make the bioactive silicon nitride the subject of research in this area due to its unique properties. Ample evidences exist to prove that Si_3N_4 enhances biomineralization and osteogenic differentiation when compared to Ti and PEEK, but the correlation between osteoprogenitor adhesion and growth and Si_3N_4 surface activity is still poorly understood. So, this study seeks to correlate the osteoprogenitor adhesion and growth to surface roughness, surface energy, and surface functional group formation to identify differences in the osteogenic potential of Si_3N_4, Ti, and PEEK implant materials.

1.2 Objectives for the Research

The aim of this study was twofold. The first was to determine the effect of Si_3N_4 on the biomineral formation and hydroxyapatite (HA) crystals nucleation (free cells in vitro) when compared to conventional craniofacial reconstructive implant materials such as Ti and PEEK. Determining this effect focused on comprehensive evaluation of the surface properties for the three tested materials: Si_3N_4, PEEK, and Ti. XANES analysis, surface roughness and morphology, contact angle, and surface energy calculations were carried

out before and after the free cells in vitro study to understand the nature of each material's surface. Raman Spectroscopy, FT-IR analysis, X-ray diffraction, atomic force microscopy, and scanning electron microscopy were used to investigate the HA nucleation and bio-minerals formation after the in vitro studies.

The second aim was to assess the impact of Si_3N_4 on osteoprogenitor cell adhesion and growth and correlate it to the surface roughness, surface energy, and surface functional group formation. Cellular adhesion was studied by culturing murine calvarial MC3T3-E1 osteoblast cells on sample surfaces for 24 hours, and at the end of experiment the cells were fixed and imaged via SEM at various magnifications. For cell proliferation studies, cells were cultured and incubated for 1, 4, and 7 days, then the MTS Cell Proliferation Assay Kit was used to evaluate the cellular proliferation.

1.3 Research Outlines

This thesis represents the research work in total of five chapters. Following is the list of chapters with brief content to guide the readers on the authors approach to whole research.

Chapter 1 provides a brief introduction to the current study and provides the basic research motivation and the expected research objectives.

Chapter 2 explores background information on the craniofacial implant materials and reviews the existing literature on Titanium and PEEK as a conventional craniofacial implant material. Also, it provides important concise information regarding the silicon nitride as a novel biomaterial for spinal fusion procedure.

Chapter 3 gives an overview of the experimental approach and techniques used in this research as well as the rationale behind the use of each technique.

Chapter 4 addresses the first manuscript that presented the enhancement of osteoprogenitor cell growth via the increased surface energy and formation of amide, calcium and phosphate functional groups on the silicon nitride surface versus titanium or peek craniofacial implant materials.

Chapter 5 discusses further characterization for the biological samples and focuses on the matrix deposition analysis after 30 and 60 days of cell culture. This chapter also provides the general guidelines and the salient features of the future work.

CHAPTER 2

BACKGROUND AND LITERATURE REVIEW

Fractured or missing bones and the various endeavors to fix or replace them have presented a remediation challenge that has attracted researcher's attention throughout human history. The recent era witnessed a dramatically increase in bone grafts and substitution procedures due to the massive increase in the number of road accidents, wars, trauma cases, the rate of congenital facial deformities, and technological advancements. Then, orthopedic implants were manufactured to replace or support the missing or damaged bone or joint and restore the normal skeletal function of the body. According to Allied Market Research (AMR) reports, the global orthopedic implants market achieved $47.2 billion in 2016 and is expected to reach $75 billion by 2023 [27]. Deep view within this market indicated that bone grafts and substitution procedures reported $2.4 billion in 2015, and this value is expected to jump to $3.4 billion by 2022 [1], which confirms the rapid increase in bone grafts and substitution procedures. Within the bone grafts and substitutes market, craniomaxillofacial implants have become an important branch that is controlled by several factors [2]. In this chapter, we will discuss the meaning of craniomaxillofacial and review the conventional materials that are currently used in the craniofacial implant procedures. Also, we will present the unique properties of the novel bioactive silicon nitride that make it a promising material for the craniofacial implants.

2.1 Craniomaxillofacial

Craniomaxillofacial is a term that is related to the whole area of the mouth, jaws, face, skull, and associated structures. While maxillofacial refers only to the jaws and face, craniofacial relates to, or involves both the cranium and the face. Craniomaxillofacial bone

defects, resulting from trauma, cancer, resection, or congenital defects can affect either the bony contour, or the bony continuity, or both [28][29]. These facial skeleton deformities used to be reconstructed using autografts, xenografts, or allografts [30][31]. Autologous bone grafts are considered the gold standard due to the consideration of full integration and regeneration in the host body [32]. Although autografts are the gold standard for craniofacial skeletal reconstructions, they have serious limitations and drawbacks. Availability of a suitable donor, large defect sites, tissue harvesting problems, resorption of the graft, donor site morbidity, chances of infection at both the recipient and donor sites, increased surgical time, patient discomfort, ethical issues, risk of infection, and religious affiliations are the common limitations and disadvantages of autografts [33][34][32]. On the other hand, allografts and xenografts have potential infectious and immunological risks, and some ethical issues and religious affiliations [1][34]. To avoid these disadvantages and limitations, various alloplastic materials have been developed and are in clinical use for bone replacement procedures [31]. Alloplastics are biological materials either produced by extensive physical/chemical processing of xenogeneic or completely synthetic materials. Alloplastic materials could be a material of animal origin, plant origin, or synthetic biomaterials. These biomaterials could be metal (titanium), ceramics (calcium phosphate cements and HA), and different types of polymers such as acrylic bone cement, polymethylmethacrylate (PMMA), polyethylene (PE), and polyetheretherketones (PEEK) [34]. The main roles of these biomaterials are to support function or replace a part of a living system. So, there are necessary properties that must be found in a material to be an ideal scaffold or implant and get approved for medical applications. The first property is **biocompatibility,** which is defined as the ability of a material to support normal cellular activity, including molecular signaling systems, without any local and systemic toxic effects to the host tissue. It is the most important challenge that distinguishes a biomaterial from any other material and tests

its ability to be an ideal implant or scaffold [35][36]. Second, properties of **osteoinduction, osteoconduction,** and **osseointegration** are of great importance for any biomaterial to lead to an ideal osteogenesis (development and formation of bone). The process by which osteogenesis is induced is known as **osteoinduction** and it means the ability to induce new bone formation or the stimulation of primitive, undifferentiated, and pluripotent cells to develop into the bone-forming cell lineage [36][37]. **Osteoconduction** means that bone grows on a surface, so the osteoconductive material is one that permits bone cells to adhere, grow, proliferate, and form an extracellular matrix on its surface or down into channels, pores or pipes [37]. Ideal osteoconductive materials could improve the fixation of solid implants to the surrounding bone tissues by the formation of strong bonding between the implant and the bone. Direct contact between implants and living bones that end up in the formation of bony tissue around the implant without any growth of fibrous tissue at the bone/implant interface is known as **Osseointegration** [37]. Last**, Mechanical strength** of the biomaterial also plays an important role in the implant stability [36]. The implant must have a sufficient mechanical stability to withstand the implantation procedure and resist the collapse during a patient's normal activities. So, selecting a biocompatible material that serves as matrices for tissue formation, promotes cell adhesion, proliferation, and differentiation, as well as supports mechanical stability, is a crucial matter for any medical implant [36].

Over the years, an enormous amount of research has been done on titanium, titanium alloys, and polymers, especially PEEK, as materials of interest for craniofacial bone defect procedures. The next section will explore the recent studies related to Ti and PEEK materials and highlight the advantages as well as the limitations of using these implants.

2.2 Titanium as Craniofacial Implants Material

As early as 1965, pure titanium plates and screws were introduced for orthopedic applications [38], and for many decades, metallic materials like titanium (Ti) and its alloys have been used as biomaterials for medical applications, such as orthopedic and dental fields [11]. The main reasons for using titanium as biomedical implants are due to its excellent biocompatibility [39], high corrosion resistance [40], and specific mechanical properties [11][38][41][42]. Over the years, numerous studies have investigated the properties of Ti and its alloys in an effort to find a superior material for long-time implantations. In his 2000 study, Pohler argued that commercially pure titanium is an excellent implant due to its outstanding biocompatibility that is expressed by two important observations: the favorable response of tissues to Ti surfaces and the absence of allergic reaction [38]. Furthermore, he mentioned that using Ti alloys, such as Titanium-6Aluminium-7Niobium (Ti6Al7Nb) or Titanium-6Aluminium-4Vanadium (Ti6Al4V), resulting in β- and β+α alloys that have higher strength and mechanical properties [38]. β-alloys offer the unique characteristic of low elastic modulus and superior corrosion resistance [43].

Although Ti has a low elastic modulus compared to other metals (110 GPa), it is still 3-11 times greater than the human bone modulus (10-30 GPa). This mismatching of Young's modulus between the bone and Ti implants leads to major problems such as the stress-shielding effect [41]. This shielding effect makes the bone insufficiently loaded that results in bone remodeling and healing retardation as well as loss of density and increase in porosity [41][44]. One approach to mitigate this problem is to reduce the elastic modulus by introducing pores [45]. These pores minimize the damages to tissues adjacent to the implant, increase bone/implant bonding by forming interconnections between the bone and porous implants, and allow extensive body fluid transportation [41][11]. So, the porous Ti scaffolds/implants have been extensively studied. For example, I.-H. Oh et al. reported that

Young's modulus and three-point bending strength of porous Ti compacts having the porosity around 30 vol.% are close to those of human cortical bone [41]. Also, Dabrowski et al concluded that porous Ti scaffolds with 75% porosity can assure ingrowth of bone tissue that results in good bonding between metallic implants and bone. Furthermore, highly porous Ti scaffolds with ~1 GPa modulus may be effective in reducing the stress shielding effect in load-bearing applications [11]. Another study reported that porous Ti with 40% porosity and bioactive Ti (chemically and thermally treated) produced enhanced bone ingrowth and apposition [42]. In a word, from these different studies that investigated the relation between porous implant surface and bone ingrowth, we can conclude that the porous implant surface introduces interconnections between the implant and the bone that result in alleviating the stress shielding effect.

Although alloying of pure Ti with different elements (Al, V, and Nb) results in higher strength and enhanced mechanical properties alloys, all these alloying elements have been reported as highly cytotoxic elements inside the human body. Vanadium is classified in the sterile toxic group, aluminum included in the scar tissue group, and Niobium in the loose connective vascularized group regarding tissue reaction [39]. So, from the biological point of view, these Ti alloys (the most common implant) are not the ideal alloys for long term implantation in the human body due to their high content of cytotoxic elements [39]. Furthermore, meshes made of Ti showed an infection rate average of 7.71%, and the Ti-plates reported 8.31% according to a 2017 study by Kwarcinski et al.[32].

Aseptic loosening of titanium-alloy components is the most common complication of these implant materials [46][47][13]. The failure of the bond between the implant and the bone in the absence of infection is known as aseptic loosening. Metallic debris from Ti alloys induces aseptic loosening that result in severe osteolysis [47]. Within this area of

investigation, several studies have reported on Ti implants failure due to this impaired implant fixation, which accounts for 75 % of the failure occurrences [13][14][46]. Furthermore, another study recommended to avoid the use of implants made of titanium alloys in which ions have not been implanted [47].

Oxidative stress and absence of antioxidant effects of Ti implants are also common issues that these materials present. R. Tsaryk et al. reported that Ti6Al4V alloy-induced permanent oxidative stress during the in vitro study of endothelial cells on the surface of Ti6Al4V alloy [15][48]. So, from the previous studies we can conclude that stress shielding effect [41][44], cytotoxicity of alloying elements [39], aseptic loosening [12][13][14][46][47], poor long-term stability, absence of antioxidant effects [15][48], and prolonged healing time remain critical issues for Ti implants. Therefore, using Ti implants for craniofacial reconstruction and orthopedic applications is still less than optimal for bone healing and long-term applications.

2.3 PEEK as a Craniofacial Implant Material

Polyaryletherketones (PAEKs) are a relatively new series of high temperature thermoplastic polymers that have been introduced since 1980. This family includes two very important polymers: poly(aryl-ether-ether-ketone) (PEEK) and poly(aryl-ether-ketone-ether-ketone-ketone (PEKEKK). PAEKs consist of an aromatic molecular chain that is interconnected by ether and ketone functional groups [5]. The polyaromatic ketones structure offers some important properties that allowed these polymers to be used as biomaterials for orthopedic, trauma, and spinal implants [5][49][50]. Among these properties are its stability at elevated temperature (300°C); un-reactivity and inherent resistance to chemical, thermal, and post-irradiation degradation; biocompatibility; and its relatively low elastic modulus (3-4 GPa) that closely match cortical bone (12-20 GPa) [5].

Although PEEK has very attractive properties that make it a critical component in the field of biomaterials, it still has some limitations and drawbacks. The main concerns that have been raised against PEEK are its bio-inertness and hydrophobic surface properties that result in limited fixation with bone and poor osseointegration [5][49][50]. As a result of its bio-inertness, PEEK surfaces do not integrate with the surrounding bone and can form a fibrous connective interface that allows micromotion and eventually leads to implant failure [6][5][32].

Recent studies have explored the impact of PEEK implant materials on the osteoblast and in vitro bone forming capacity. Olivares-Navarrete et al. compared the osteoblast differentiation on Ti and PEEK surfaces and reported that osteoblasts differentiate to a lesser degree on PEEK versus Ti surfaces, which means that the PEEK surface has a lower level of support for osteogenic tissues [6]. Furthermore, M. H. Pelletier et al. reported that Ti implants had a significant higher bone contact percentage compared to PEEK surfaces [7]. This lower bone contact can be attributed to the hydrophobic nature and bioinertness of PEEK materials that do not allow protein absorption as well as cell adhesion on the surface [7]. Also, it has a high average infection rate of 7.89%, as well as a zero interactive surface form and tissue attachment bioactivity [32].

Although coating of PEEK surface with osteoconductive materials like hydroxyapatite (HA) has introduced as an alternative approach to improve its osseointegration [50], PEEK implants are still less than optimal for craniofacial reconstruction and orthopedic applications. Lack of bioactivity, smoothness, poor wettability, and low surface energy are still the main issues that limit osteoblast differentiation and bone regeneration on PEEK surfaces [6][7][8][9].

2.4 Bioactive Silicon Nitride as an implant material

Silicon nitride (Si_3N_4) is a relatively new synthetic material that has been synthesized by Deville and WÖhler in 1859, and it was first used as refractory material in the 1960s [21][51]. In the 1980s, non-oxide Si_3N_4 ceramic was introduced as a potential high-temperature structural engine material [51]. Since then, it has been used in a wide range for internal components of combustion engines. Over the years, several strands of Si_3N_4 have been developed, such as porous Si_3N_4, dense Si_3N_4, amorphous thin films, and powder production. Furthermore, it has been used in various industries and applications such as refractory materials, engine materials, atomic-energy jets and rockets, reinforcement of metals, and recently bioactive materials for orthopedic applications [21][51]. The main reason behind this considerable attention paid for Si_3N_4 is its unique combination of excellent properties. Silicon nitride': excellent properties include: mechanical strength; high fracture toughness; oxidation, corrosion and thermal shock resistance; inherent phase stability; low wear; scratch resistance; hydrophilicity; improved radiographic imaging; biocompatibility; and bacteriostasis effect [51][21][16][17][20][26].

Over the last 50 years, Si_3N_4 has been produced by one of these three following strategies: reaction bonding, sintering, and pressure-assisted sintering, respectively. In the reaction bonding method, silicon nitride ceramic material is produced by nitridation of a porous-shaped silicon (Si) powder. This porous-shaped material is heated in N_2 at temperature range of 1200-1400 ºC that allows Si to react with N_2 and form bonded particles of Si_3N_4. The formed Si_3N_4 has high porosity, and relatively low density and strength (200-300 MPa) [16]. The second approach is preparing Si_3N_4 by sintering, in which additives (typically Y_2O_3 and Al_2O_3) mixed with Si_3N_4 powders are compacted in an N_2 atmosphere of 10–20 MPa pressure and heated at temperature of ~1700 ºC. These additives aid in the densification process by forming a liquid phase from the reaction of the native SiO_2 layer

on the Si_3N_4 powder. By cooling, this liquid phase solidifies to form a glassy (amorphous) or partially crystallized glassy phase at the Si_3N_4 grains boundaries [16]. The last technique is known as pressure-assisted sintering which uses pressure to address inadequate densification of sintered Si_3N_4. This technique can be done by hot pressing or hot isostatic pressing (HIP). In the hot-pressing method, a powder of Si_3N_4 with additives is placed in a graphite die and then subjected to high applied pressure (~50 MPa) at 1700 ºC. On the other hand, in HIP, Si_3N_4 powder with additives is encapsulated in a metal can and pressurized at 150–200 MPa in 1700 ºC [16][21]. Although this method has a higher manufacturing cost, the prepared Si_3N_4 gains improvements in strength and toughness [16][52].

In recent years, researchers have become increasingly interested in silicon nitride as a new bioactive material for biomedical implants, and an enormous amount of research has been done in this field. Recent studies proved that non-oxide Si_3N_4 ceramics have a similar, favorable biocompatibility profile compared to ZrO_2 and Al_2O_3 oxide ceramics that used in orthopedic applications. Furthermore, biocompatibility of Si_3N_4 has validated by the complete spectrum of ISO-10993 biocompatibility testing. Also, Si_3N_4 has been successfully implanted in spinal surgery without any adverse effects for over 3 years [16]. Neumann et al. studied the biocompatibility of Si_3N_4 in vitro and confirmed a favorable biocompatibility of silicon nitride ceramic [53]. Also, the L929-mice fibroblast cell culture showed that Cell growth, viability and morphology on the Si_3N_4 surface were comparable to Ti surfaces [53]. Further investigation by Kue et al. confirmed the non-toxicity and the biocompatibility of the ceramic Si_3N_4 surface using human osteoblast-like MG-63 cell line in vitro testing [54].

Mazzocchi et al. successfully prepared three different silicon nitride-based materials, using the hot-pressing technique, and studied the microstructure, cytotoxicity, and me-

chanical properties of these compositions. Their findings proved outstanding characteristics of the three-different silicon nitride-based ceramics. Also, the cytotoxicity studies confirmed inertness and biocompatibility for all of these materials [20].

In 2004, Neumann et al. investigated the cytotoxicity of different qualities of Si_3N_4 ceramics using in vitro L929-cell line culture. Different biomedically approved materials such as Ti, Al_2O_3, and polyvinylchloride (PVC) used as control materials. They reported that there was no observation of cytotoxicity effect of the Si_3N_4; furthermore, the cell morphology remained the same as on Ti and alumina samples, and the polished surfaces showed an advanced biocompatibility and higher numbers of cells [55].

In his 2006 study, Neumann et al. implanted a mini-fixation system prototype made of Si3N4 in 3 minipigs to study the osteosynthesis in an artificial frontal bone defects [56]. By the end of the study, they reported that Si3N4 miniplates and screws showed satisfying intraoperative workability, no implant loss, displacement, or fracture. Also, the bone healing was complete in all animals and new bone formation was observed in direct contact to the implant. This study concluded that Si3N4 ceramic has a good biocompatibility in both in vitro and in vivo, and may serve as a biomaterial for midface osteosynthesis including reconstruction of the floor of the orbit and the skull base [56].

In 2012, Webster et al. investigated the anti-infection and osteointegration properties of silicon nitride compared to PEEK and Ti implant materials by implantation of these materials into matching rat calvarial defects. The animals' bacterial infection was induced by injection of 1 $x10^4$ Staphylococcus epidermidis. The results emphasize that the new bone formation around Si3N4 was ~69% compared to 24% and 36% for PEEK and Ti, respectively, in absence of bacterial injection. In the presence of bacteria new bone formation for Si3N4, Ti, and PEEK was 41%, 26%, and 21%, respectively. Moreover, no live bacteria were present adjacent to Si3N4, compared to 88% on PEEK and 21% on Ti. This

study concluded that bioceramic Si_3N_4 implants demonstrated superior new bone formation and resistance to bacterial infection compared with Ti and PEEK [10].

In 2017, Pezzotti et al. reported that different heat-treatments of the bioactive Si_3N_4 result in peculiar crystallographic characteristics of the N-apatite ($Y_{10}(SiO_4)_6N_2$) and Y-disilicate (β-$Y_2Si_2O_7$) surface phases [17]. These phases promote protein adhesion and differentiation of progenitor cells into mature osteoblasts. Furthermore, the number of cells per unit area on Si_3N_4 surfaces was four-fold and two-fold higher than the Ti alloy and Al_2O_3, respectively. The study concluded that Si_3N_4 surfaces enhance progenitor cells adhesion, osteoblast differentiation, and bone formation more efficiently than conventional substrates (Ti alloy and Al_2O_3) [17].

Later in 2017, Pezzotti et al. provided the evidence for the unique behavior of the bioactive Si_3N_4 in bone tissue engineering [24]. By comparing two short-term intervertebral spinal spacers made of Si_3N_4 (cervical implant) and PEEK (lumbar device) with comparable in vivo service, they confirmed that the amount of bone growth within Si_3N_4 implant was significantly greater than in PEEK implant. Furthermore, the release of Si, and N elements from the Si_3N_4 ceramic surface upregulates the metabolic activity of osteoblasts, and results in rapid and efficient bone growth [24].

From the previous studies, we could conclude that Si_3N_4 enhances biomineralization and osteogenic differentiation when compared to Ti and PEEK implants, but the correlation between osteoprogenitor cells adhesion/growth and Si_3N_4 surface activity is still poorly understood. So, our study seeks to correlate the osteoprogenitor cells adhesion and growth to surface roughness, surface energy, and surface functional group formation to identify differences in the osteogenic potential of Si_3N_4, Ti, and PEEK implant materials.

CHAPTER 3

EXPERIMENTAL APPROACH AND TECHNIQUES

3.1 Sample Preparation

Silicon nitride (Si_3N_4) samples were provided by Amedica Corporation (Salt Lake City, UT, USA). Details of their processing and basic properties are provided elsewhere [21][19]. This bioceramic has a nominal composition of 90 weight % (wt.%) Si_3N_4, 6 wt.% yttrium oxide (yttria, Y_2O_3), and 4 wt.% aluminum oxide (alumina, Al_2O_3). The Y_2O_3 and Al_2O_3 serve as densification additives. From this composition, a quantity of disc samples (Ø12.7 x 2.5mm) was prepared for characterization and biological testing. They were separated into two groups – as-fired and polished. The as-fired samples had no post-densification treatments whereas the polished samples were abrasively lapped to a near-mirror finish. Dimensionally identical samples were also prepared from PEEK (ASTM D6262, Ketron® PEEK 1000, Quadrant EPP USA, Inc., Reading PA, USA; distributed by McMaster-Carr, Santa Fe Springs, CA, USA) and a titanium alloy (ASTM F136, Ti6Al4V-ELI, distributed by Vincent Metals, Minneapolis, MN, USA). The Ti and PEEK samples were also produced in two groups – as-machined and polished – using 600 grit and 2000 grit abrasive lapping, respectively. All samples were prepared at two different levels of roughness in an effort to examine each material's surface morphology with respect to in vitro osteoblast cell adhesion and growth.

Prior to all experiments, samples were immersed in 100% ethanol and ultrasonicated for 5 minutes to remove any possible surface debris. Prior to the in vitro studies, samples were gas sterilized using ethylene oxide for 12 hours and then vacuum desiccated for 24 hours to remove residual absorbed ethylene oxide gas. Surface cleaning and sterilization were conducted at standard temperature and pressure (i.e., 25^{o}C and 1 bar).

3.2 Samples Characterization

The current study was performed in three different steps. First, study and characterization of the bare samples' surfaces in a way to understand the chemistry of each material before any in vitro studies. Second, free cells in vitro studies were conducted on all samples (Si_3N_4, PEEK, and Ti) to investigate the effect of each material on the biominerals formation. Last, in vitro cell study using Murine calvarial MC3T3-E1 osteoblast cells was accomplished to investigate the cell adhesion and proliferation on each surface. The experimental studies were conducted in the Department of Material Science and Engineering at the University of Texas at Arlington and the Department of Biomedical Sciences at Texas A & M University's College of Dentistry. All characterizations were carried out at the Center for Characterization of Materials and Biology at the University of Texas at Arlington (CCMB, UTA).

3.2.1 X-ray Absorbance Near Edge Structure (XANES) Analysis:

X-ray Absorbance Near Edge Structure(XANES), also known as Near Edge X-ray Absorption Fine Structure (NEXAFS), spectroscopy is a powerful, highly selective, non-destructive technique. XANES enables the study of the chemical bonding nature in a material as well as the element-by-element analysis of the local atomic environment (i.e. valance, coordination, and distortions in geometry due to nearest neighbor atoms) [57]. This technique uses the synchrotron facility that generates an intense electromagnetic beam by accelerating charged particles at speeds close to that of light. This electromagnetic radiation (i.e. X-ray) has sufficient energy to excite a core electron of an atom to an empty hole below the ionization threshold "excitonic state" or above the ionization threshold "continuum state." When a core electron absorbs an X-ray photon with energy matched to its distinct binding energy, it will be ejected from its core leaving a core hole. These extremely

energetic core holes have an average life span of 1 femtosecond due to their unstable nature, so it is rapidly decaying through auger electron ejection or X-ray emission.

Fig. 3-1 shows a schematic illustration of an X-ray absorption edge, the structure found within 50 eV of the absorption edge refers to XANES. However, the structure beyond XANES, that can be extended to 1000 eV or more above the absorption edges, refers to the Extended X-ray Absorption Fine Structure (EXAFS) caused by the interference between the outgoing and the back-scattered photoelectron waves [57][58]. The typical XANES spectra consists of three different zones: a pre-edge, an absorption edge, and a post edge. The 'edge' means that each spectrum is taken around an element-specific core-electron excitation energy. The absorption edge is a phenomenon that corresponds to absorption of the X-ray photon by a specific type of core electron and appears as an abrupt increase in the absorption as shown in Fig. 3-1. The absorption edge is mainly used to determine the oxidation state and it can be shifted up to 5 eV per one-unit change. The pre-edge structures appear as a weak transition below the absorption edge and it can be used to investigate the local geometry around an absorption atom [58]. The absorption can be measured through the current or total electron yield (TEY) or the fluorescence signal (FLY) of the materials during the absorption. The detectors are beamline dependent, so a beamline can be thought of as an end station equipped to detect a certain energy range of signals [58]. For the current study, Si-L edge and Y-M edge are the edges of interest for Si_3N_4 samples to determine the presence of Si-O, Si-N, and Si-Si bonds and how the presence of Y affects these coordination structures. Later for the in-vitro studies, Ca-L edge, O-K edge, N-K edge, and P-K edge might also be of interest. Due to the large difference in energy between the edges, multiple beamlines must be used to collect the spectra. All XANES spectra were collected at the Canadian Light Source Synchrotron Facility (Saskatoon, Canada) using the High Resolution Spherical Grating Monochromator (SGM, 11ID-

1) and the Variable Line Spacing Plane Grating Monochromator (VLS PGM 11ID-2) beamlines. The beamline parameters including available detectors, energy range, edge collected, resolution, and beam spot size are summarized in Table 3-1.

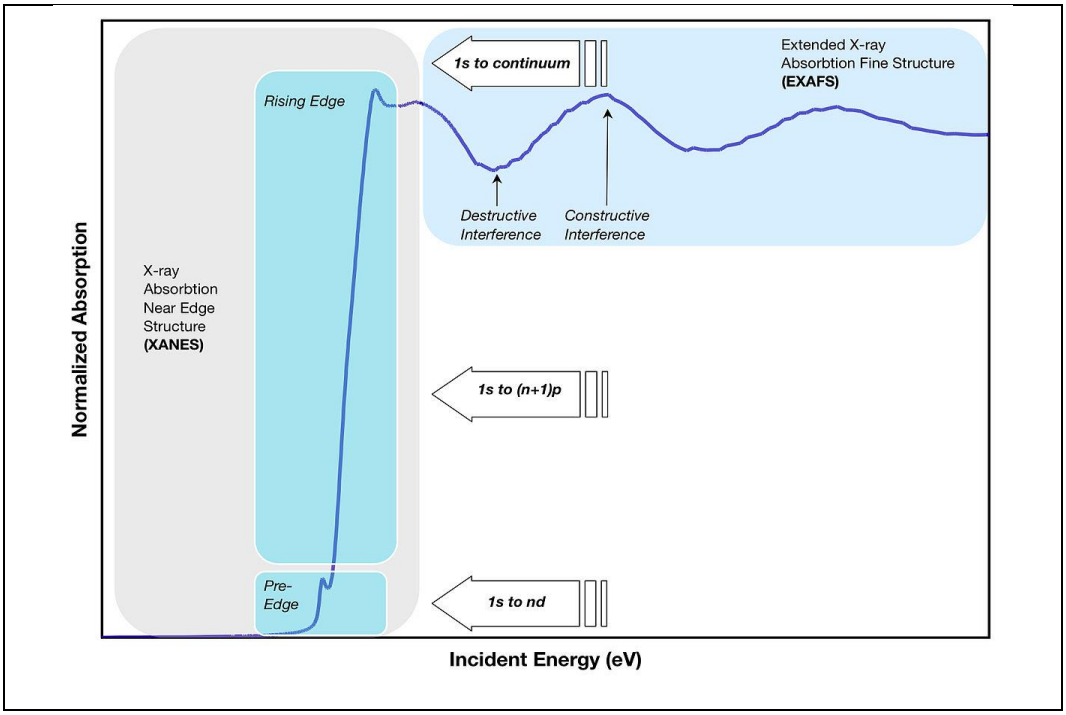

Figure 3- 1: Schematic illustration of X-ray absorption edge. Figure courtesy of Wikipedia.

Table 3- 1: Canadian Light Source Beamline Parameters.

Beamline	SGM	VLS PGM
Energy Range (eV)	250 - 2000	5.5 - 250
Edges	N-K, O-K, Ca-L	P-L, Si-L
Spot Size (μm)	1000 x 100	500 x 500
Source	45 mm planer undulator	185 mm planar undulator
Resolution (eV)	0.2	0.1

3.2.2 Surface Roughness

It is generally accepted that the surface roughness and composition of the test material have a great effect on cell activity: cell adhesion and proliferation. Recent studies have shown that cell adhesion depended on titanium oxide thickness, roughness, and surface microporosity [59][60]. Ponsonnet et. al. demonstrated a strong correlation between surface roughness of Ni-Ti alloy and cell proliferation [61] and it also can disturb the relationship between the surface free energy and the cell proliferation [62]. For the current samples, to correlate the effect of surface roughness on the cell adhesion and proliferation, a comprehensive surface roughness study will be conducted using the following techniques:

3.2.2.1 Atomic Force Microscopy

Atomic Force Microscopy (AFM) is a very-high resolution type of scanning probe microscopy, with unprecedented resolution on the order of frictions of a nanometer, which makes it 1000 times better than optical diffraction limit. AFM is a powerful and multifunctional technique that allows for imaging, probing, and manipulating materials (Metals, Ceramics, and Polymers) as well as biological samples [63][64]. It can be used to form a three-dimensional shape image (topography) by imaging the reaction of the probe to the forces that the sample surface imposes on it. AFM can be also used to determine the mechanical properties of the sample by measuring the force between the probe and the sample as a function of their mutual separation. Furthermore, this force can be used to change the properties of the sample in a controlled way that enables AFM manipulation.

Since the AFM operates by allowing the probe to scan and build up a map of the height or topography of the sample surface, it is one of the most important tools to measure and map the surface roughness. According to the nature of the tip motion, AFM has three different imaging modes; contact, tapping, and non-contact modes. In the Contact mode,

the tip is directly dragged on the sample surface and the surface features are measured through the cantilever deflection or the feedback signals required to keep the cantilever at constant position. In the Tapping mode, the cantilever is driven to oscillate up and down at or near its resonance frequency and the AFM image is produced by imaging the force of the intermittent contacts of the tip and the sample surface. On the other hand, Non-Contact mode does not allow the cantilever tip to touch the sample surface, but instead the cantilever oscillates with an amplitude of a few nanometers (<10 nm) down to a few picometers. Vander Waals forces of sample surface decrease the resonance frequency of the cantilever that correlated to adjust the tip-to-sample distance. Measuring the tip-to-sample distance allows the scanning software to construct a topographic image of the surface. Then, using AFM will provide topography imaging as well as estimating the roughness parameters such as [65]:

- Roughness Average (Ra), or arithmetic average height, which is the average of the absolute deviation of the roughness irregularities from the mean line over the sampling length.
- RMS Roughness (Rq), which is the root mean square roughness and represents the standard deviation of the distribution of surface features heights. Then, Rq is an important parameter that describes the surface roughness by statistical methods.
- Maximum Profile Peak Height (Rp) represents the distance between the highest point of the profile and the mean line within the evaluation length.
- Maximum Profile Valley Depth (Rv) gives the distance between the deepest valley of the profile and the mean line within the evaluation length.
- Tin-point height or Average Maximum Height (Rz) estimates the difference in height between the average of the five highest peaks and the five lowest valleys over the evaluation length.

- Maximum Height of the Profile (Rt or Rmax) is the vertical distance between the highest and lowest points of the profile within the evaluation length.

The current study used the AFM (AFM, Park XE 70, Park Systems, Suwon, Kore) contact mode to assess the morphological features and surface roughness of the samples. R_a and R_q roughness parameters, as well as AFM three-dimensional images of the samples surface before and after in-vitro studies, will be presented.

3.2.2.2 Contact Stylus Surface Profiler

Stylus profilometers use a probe that physically moves along the surface to acquire the height of surface features. A feedback system monitors the force from the sample pushing up the probe as it moves along the surface, and the changes in Z position of the arm holder can be used to reconstruct the surface. In the present study, the contact stylus surface profiler (Alpha Step IQ, KLA Tencor Corporation, Milpitas, CA) at UTA Nanofab, was used to scan and reconstruct the samples surface and roughness parameters. Although the stylus profiler analyzes thin-step heights, measures surface micro-roughness, and combines high measurement precision and versatility, its stylus tip size and shape can influence the measurements and limit the lateral resolution.

3.2.2.3 Optical Profilometer

Recently, a non-contact optical profiler (NOP), based on the principle of two-beam optical interferometry, became a widely used device for surface characterization in research and industry [66]. Optical profilers are interference microscopes that use the wave properties of light to compare the optical path difference between the reference surface and the test material surface. So, NOP can measure the surface height variations - such as surface roughness – and enables three-dimensional mapping of the surface with great precision. Since the optical profilometer can perform analysis on a relatively large surface

area and allows for a non-contact mapping, it is a suitable device to capture the surface topography images and estimate the different surface roughness parameters.

In the current study, NPFLEX Optical profilometer (NPFLEX, Bruker, Billerica, MA) was used to map the surfaces of the samples and estimate the roughness parameters. It is the first optical metrology system built to handle nano - to macro - features on samples of widely varying shapes and sizes. NPFLEX also provides data-rich, three-dimensional images, superior resolution, and repeatability beyond what is possible with contact instrumentation. By using the optical profilometer, we can scan and analyze a large surface area in an effort to create a good representation of the whole sample and avoid the scan area limitation of the AFM. Also, using a non-contact mapping device allows to capture the tiny features on the surface that cannot be achieved by using the alpha KLA contact profiler with its stylus tip diameter limitation.

3.2.3 Wettability and Surface Energy

Surface hydrophilicity, or wettability, of a biomaterial is a key factor that has a strong effect on cell response and biocompatibility of the surface itself [67]. Studies of the bone/implant interface have shown that increased hydrophilicity increases the rate and extent of new bone formation around the implant due to faster cell adhesion and spreading through the adsorbed protein layer [68]. So, the hydrophilicity study of the samples surface in the current work will reflect a clear image of the cells response on each surface. The relative wettability of each sample was investigated through contact angle measurements. Sessile's drop technique was used to determine the contact angle of deionized water on the surface of each sample. Each material was tested in triplicate (3 samples), and 9 drops of the water were used for each sample. The images were captured using a high-speed camera (WATEC, high resolution, NAVITAR lens) synced to FTA32 software (First Ten Angstroms Inc, Portsmouth, VA).

It is well known that Young's equation (Equation 3.1) gives the relationship between the interfacial tensions of solid-vapor, liquid-vapor, solid-liquid interfaces, and the contact angle. Also, surface energy can be broken down into dispersive and polar components according to equation 3.2. Then, the polar and dispersive components of a solid's surface energy could be calculated by applying the Owens-Wendt-Kaeble equation (Equation 3.3), that treats the total surface energy as the geometric mean of the dispersive and polar components [69][70]. To achieve this, dispersive and polar components of the surface tension of at least two probing liquids must be known as shown in equation 3.4. So, the contact angles, of the well-known dispersive and polar components, of deionized water and diiodomethane (> 99% purity, Sigma-Aldrich, St. Louis, MO, USA) on the sample's surfaces were determined, and the surface energy was calculated using the polar and the dispersive components values of the testing fluids as taken from literature (table 3-2).

$$\gamma^{LV}\cos\theta = \gamma^{SV} - \gamma^{SL} \tag{3.1}$$

$$\gamma = \gamma^{d} - \gamma^{p} \tag{3.2}$$

$$\gamma^{SL} = \gamma^{S} - \gamma^{L} - 2\left(\gamma_L^d \gamma_S^d\right)^{1/2} - 2\left(\gamma_L^p \gamma_S^p\right)^{1/2} \tag{3.3}$$

$$0.5\,\gamma^{LV}(1+\cos\theta) = \left(\gamma_L^d \gamma_S^d\right)^{1/2} + \left(\gamma_L^p \gamma_S^p\right)^{1/2} \tag{3.4}$$

Table 3- 2: Surface energy (γ^{LV}) and its corresponding dispersive (γd) and polar (γp) component values for probing liquids [71][72].

Probing liquid	$\boldsymbol{\gamma^{LV}}$ (mJ/m2)	γ^d (mJ/m2)	γ^p (mJ/m2)
Water	72.8	21.8	51.0
Diiodomethane	50.8	50.4	0.4

3.2.4 Scanning Electron Microscopy and EDS

Scanning Electron Microscopy (SEM) allows for creating high-resolution images with a relatively large depth of focus, so it can provide surface topography and morphology images. In the current study, an Ultra HR-SEM (Hitachi S-4800 II FE SEM, Hitachi, Tokyo, Japan) and Hitachi S-3000N Variable Pressure SEM were used to capture the surface features, as well as the interface between the sample surface and the HA layer that formed after in vitro studies. Due to the nonconductive nature of PEEK and Si_3N_4 samples, these samples were sputter-coated with a conductive silver layer using the CrC-100 sputter (Plasma Sciences Inc., Lorton, VA) prior to imaging. Compositional analysis and mapping of the surface after the free-cells in vitro studies as well as the matrix deposition were obtained using the Energy Dispersive Spectroscopy (EDS). EDS spectra and surface mapping were collected using the EDS detector connected with a Hitachi S-3000N Variable Pressure SEM.

3.2.5 Fourier Transform Infrared Spectroscopy (FT-IR)

Fourier Transform Infrared Spectroscopy (FT-IR) is a technique used to collect infrared spectra of absorption or emission of the test materials; it can collect high-spectral-resolution data over a wide range of spectra. In the current study, Thermo Nicolet 6700 FT-IR Spectrometer (Thermo Electron Corporation, Madison, WI USA) equipped with a smart attenuated total reflectance (ATR) accessory, was used to investigate the surface functional groups and biominerals formation after the in vitro studies. ATR is one accessory of FT-IR spectrophotometer that allows to measure the surface properties (1-2 µm penetration depth) of solid or thin film samples rather than their bulk properties. All FT-IR absorbance spectra were collected for 128 scans over the range of 4000-500 cm^{-1}, with an aperture of 150, and a resolution of 4 cm^{-1}.

3.2.6 Raman spectroscopy

Raman spectroscopy is a vibrational spectroscopic technique that can be used to optically investigate surface functional groups, bonding types, and molecular conformations. This technique basically depends on the inelastic or raman scattering, which means the scattered photon has less or higher energy than the incident one due to the inelastic collision of the photons with the material molecules. This vibrational spectroscopic technique is relatively simple, reproducible, and nondestructive to the tissue. In addition, only small amounts of material are required, so it became an important tool for biomedical applications and clinical evaluations. In the present study, raman spectroscopy (DXR, Thermo Scientific Waltham, MA, USA) with a 780 nm excitation laser at 100 mW, 10x objective, and a 50 µm slit was used to collect the spectra for all samples except PEEK, which needed a different setup (1 mW, 10x objective, and a 25µm pinhole). The samples were photo-bleached for 4 minutes prior to spectra collection and a 10 s exposure time was used. Thirty-two spectra per location were recorded within the range of 400 - 2000 cm^{-1}.

3.2.7 X-ray Diffraction (XRD)

X- ray diffraction (XRD) is considered as one of the most important diffraction methods among all available characterization techniques. Atomic arrangement patterns in crystalline solids can be determined using x-rays radiation [73]. By studying the diffraction of x-ray resulting from the geometry of a crystal lattice, the crystal structure and phase composition of unknown material can be determined [74]. It is well known that X-ray powder diffraction not only using for identifying the structural of unknown sample, but also it can be used for finding the grain size, presence of texture and other key microstructural factors for a well-known material. Debye-Scherrer equation (eq. 3.5) relates the crystallite size to the full width at half maximum (FWHM) of peaks [74][75][76].

$$r = 0.9\lambda/B\cos\theta \qquad (3.5)$$

where r represents the mean grain size, and B represent the FWHM of the peak in radians unit. In the current study, X-ray diffraction was used to investigate the HA formation on sample surfaces after 7 days of immersion in α-MEM. A Siemens D500-XRD system was used to collect scans using Cu Kα radiation (λ = 1.5418 Å) at room temperature. Data were recorded over the 2θ range of 20−80° with a 0.04° step size and a dwell time of 1.5 seconds. Then, the Debye-Scherrer equation was used to estimate the grain size of the formed HA.

3.3 In vitro Experiments

3.3.1 In vitro cells-free Study

In vitro cell-free study, using only the Alpha Minimum Essential Medium (α-MEM) (Sigma-Aldrich Co., Spruce St. Louis, MO, USA) was conducted to investigate the sample's surface activity and the α-MEM effect on the HA and biomineral formations on the surfaces. According to manufacturer specifications as shown in table 3-3, α-MEM contains and provides the inorganic salts (Ca^{2+}, HPO_4^{2-} , Cl^-, Na^+, K^+, Mg^{2+}, HCO_3^-, SO_4^{2-}), amino acids, vitamins, and sugars necessary for cell viability [77]. These components make it a comparable medium to the human blood plasma and the simulated body fluid (SBF) [78][79] as indicated in table 3-4. So, αMEM is considered as an important source of passive ion exchange with the bioactive material surface. Then a primary approximation of biomaterial response to cell culture media environment can be achieved by studying the response of the biomaterial to αMEM.

In the present study, all samples were immersed in α-MEM and incubated at 37˚C in a humidified 5% carbon dioxide (CO_2) atmosphere for 1, 4, and 7 days. The media was exchanged every other day, and the samples surfaces were washed with Phosphate-buffered saline (PBS) at the end of the study. Then, samples kept in the desiccator overnight before any characterizations.

Table 3- 3: Components of α-Modified Minimum Essential Media [77].

Component	M. Formula	M.Wt.	Conc.(mg/L)	Conc. mM
Calcium Chloride (anhydrous)	$CaCl_2$	111	200	1.8
Magnesium Sulfate (anhydrous)	$MgSO_4$	120	97.67	0.814
Potassium Chloride	KCl	75	400	5.33
Sodium Bicarbonate	$NaHCO_3$	84	2200	26.19
Sodium Chloride	NaCl	58	6800	117.24
Sodium Phosphate monobasic	NaH_2PO_4	138	122	0.88

Table 3- 4: Concentrations of inorganic salts found in human blood plasma, SBF, and αMEM [78][79].

Ion	Plasma (mM)	SBF (mM)	α- MEM (mM)
Na^+	142	142	144.3
K^+	5	5	5.3
Mg^{2+}	1.5	1.5	0.81
Ca^{2+}	2.5	2.5	1.8
Cl^-	103.0	148.8	124.37
$\mathbf{HCO_3^-}$	27.0	4.2	26.2
$\mathbf{HPO_4^{2-}}$	1.0	1	0.88
$\mathbf{SO_4^{2-}}$	0.5	0	0.8

3.3.2 In vitro Cells Study

Murine calvarial MC3T3-E1 osteoblast cells (American Type Cell Culture Inc., Manassus, VA) were cultured in 75 sq. cm flasks (Corning Life Sciences Inc., Tewksbury, MA) using α-MEM supplemented with 10% fetal bovine serum (FBS) and 1% penicillin/ streptomycin (pen-strep) until 75-90% confluence. These cells were used below passage 29 incubated at 37ºC, 100% relative humidity, and 5% CO_2 (according to the manufacturer's specifications). Ethylene oxide sterilized samples of each test material (n=3) were washed twice with PBS, placed in 24 well plates, and seeded with 10^5 MC3T3 cells. All well plates used in this study were standard tissue culture plastic that was vacuum gas treated (Corning Life Sciences Inc., Tewksbury, MA).

Cellular adhesion was studied by culturing cells on sample surfaces for 24 hours. At the end of the experiment, the samples were washed in PBS twice to remove non-

adherent cells. All samples were then removed from culture plates and transferred to fresh well plates. The samples were fixed using 2% glutaraldehyde (Sigma Inc., St. Louis, MO) for 1 hour. The samples were then sequentially alcohol dehydrated using an ethanol-water mixture using sequential concentrations of alcohol (i.e., 25%, 50%, 75%, and 100%) to preserve the intact cellular structure on the sample surfaces. Cells were then imaged via SEM at various magnifications.

For cell proliferation studies, cells were cultured in a similar manner as adhesion study except for incubation periods of 1, 4, and 7 days. Samples were washed in PBS to remove non-adherent cells. Samples were removed from the incubation plates and transferred to fresh well plates with MTS reagent diluted with α-MEM (20% MTS reagent of total volume of MEM).

Samples were evaluated for cellular proliferation by an MTS Cell Proliferation Assay Kit (MTS Aqueous One Assay, Promega Inc., Madison, WI). The MTS assay is a colorimetric method for determining the number of viable cells on sample surfaces. It determines the amount of formazan produced from the mitochondria of viable cells given the MTS reagent (tetrazolium reagent) [80]. The formazan dye transforms the color of the culture media from a yellow (low cell density) to purple color (high cell density). The color of the solution was measured using a spectrophotometer (Spectromax Plus, Spectromax Inc., San Jose, CA) at 540 nm. The measured optical density of the solution was converted to cell density using a calibration curve of cell density versus optical density.

3.3.3 Extra Cellular Matrix study

It is well known that collagen type I is the most abundant protein in the extracellular matrix (ECM) and the human body as well [81]. Collagens represent 90% of bone matrix protein content [82]. Furthermore, collagen gives the structural support to the bone cells and it is present in the EMC as fiber-liked proteins [81,83]. In the current study, various

analysis such as Ft-IR, SEM, and SEM/EDS have been used to investigate the matrix deposition after 30, and 60 days of osteoblast in vitro cell culture.

Murine calvarial MC3T3-E1 osteoblast cells were seeded and treated for 30 and 60 days with an ascorbic acid medium to induce cell differentiation and ECM. After each time point, the samples were collected from culture plate, washed in DPBS twice, and transferred to a fresh well plate. Then, the samples were fixed using 2% glutaraldehyde for 1 hour. After then, the samples were sequentially alcohol dehydrated using an ethanol-water mixture with sequential concentrations of alcohol (i.e., 25%, 50%, 75%, and 100%) to preserve the intact cellular structure on the sample surfaces. Samples were dry overnight then used for FTIR analysis. After that, all samples sputtered with silver and examined by Hitachi S- 3000N Variable Pressure SEM. EDS spectra and surface mapping were collected using the EDS detector connected with the SEM.

CHAPTER 4

PAPER 1

SILICON NITRIDE ENHANCES OSTEOPROGENITOR CELL GROWTH VIA INCREASED SURFACE ENERGY AND FORMATION OF AMIDE AND NANOCRYSTALLINE HYDROXYAPATITE FUNCTIONAL GROUPS VERSUS TITANIUM OR PEEK CRANIOFACIAL IMPLANT MATERIALS

Kamal R. Awad[1, 3, +], Neelam Ahuja[2, +], Ami Shah[1],

Likith V. Reddy[4], Pranesh B Aswath[1],

Venu Varanasi[1, 2, *]

[1]Department of Material Science and Engineering, University of Texas at Arlington;
[2]Department of Biomedical Sciences, Texas A & M University, College of Dentistry;
[3]Department of Refractories and Ceramics, National Research Centre, Giza, Egypt.
[4]Department of Oral and Maxillofacial Surgery, Texas A & M Uni., College of Dentistry.
+Co-first author: Neelam Ahuja and Kamal R. Awad

*Corresponding author.

Abstract

As a relatively new and novel biomaterial, silicon nitride (Si_3N_4) has been FDA cleared for use as spinal intervertebral arthrodesis devices. Because its surface properties promote bone on-growth and ingrowth, it also has the potential to benefit craniofacial reconstruction. Thus, the aim of this work was to determine if the surface properties of Si_3N_4 could enhance the growth of calvarial osteoblasts and nucleation of hydroxyapatite (HA) crystals when compared to conventional implant materials such as titanium (Ti) and polyetheretherketone (PEEK). The investigated surface properties were contact angle (*i.e.*, surface energy), surface roughness, and surface functional group formation. X-ray absorbance near edge structure analysis (XANES) indicated the presence of Si-Si, Si-O, and Si-N bonding, which suggested random mixing of these bonding structures. Surface roughness evaluations showed that as-milled PEEK exhibited the roughest surface when compared to as-fired Si_3N_4 and as-milled titanium. Wetting behavior from sessile drop methods indicated that Si_3N_4 exhibited the lowest contact angle and highest surface energy. Cell culture studies showed that osteoblast growth was markedly enhanced on Si_3N_4 after 1 day and up to 7 days. The Si_3N_4 surface (as-fired and polished) induced the highest surface coverage and thickness of nanocrystalline hydroxyapatite in cell-free *in vitro* studies after 7 days of culture. Electron dispersive spectroscopy analysis revealed that the HA layer had a Ca/P ratio of 1.34 (as-fired Si_3N_4) and 1.58 (polished Si_3N_4). X-ray diffraction analysis revealed the formation of (211) and (203) HA nano-crystalline grains. Raman spectroscopy analysis showed the presence of surface functional groups consisting of phosphate and carbonate species. Interestingly, the surface also indicated the presence of amide and hydroxyproline groups, which are precursors to collagen. HA coverage was less dense on Ti and sparse on PEEK surfaces, and no formation of amides or hydroxyproline was observed. In conclusion, Si_3N_4 outperformed conventional craniofacial implant materials due

to its ability to induce rapid osteoblast growth, higher surface energy, and formation of collagenous precursor surface functional groups followed by dense nanocrystalline HA.

Keywords: Silicon nitride; craniofacial implants; hydroxyapatite nucleation; hydroxyproline; amide surface formation.

Introduction

Nearly 600,000 bone grafting procedures are performed in the US and 4 million globally every year at a cost of approximately $2.3 billion annually; and this healthcare burden is projected to reach $3.4 billion in 2023 [1]. Of greater concern is that the number of these procedures is estimated to rise 400% by 2050 as a result of increases in both population and life expectancy [84–86]. Craniofacial reconstructive procedures are often required for facial trauma, tumor resection, for congenital and birth defects. These reconstructive procedures require the use of implants made of autologous and heterologous bone grafts, or abiotic biomaterials. Autograft, allograft, and some biomaterials provide good biomimetic properties whereas others, like titanium, have higher primary tear resistance [87]. The use of autologous bone grafts for the repair and regeneration of critical sized defects (CSD) is not feasible or difficult due to the 3-dimensional complexity of structures, limited secondary site volumes along with donor site comorbidities. Bioceramics such as hydroxyapatite (HA) are used clinically for bone repair and reconstruction, and their ability to promote bone integration by rapid cellular proliferation makes them suitable for limited reconstruction [18,88–91]. However, HA's fragile nature, lack of osteosynthesis capacity [92], risk of secondary infections [93–97] (especially in frontal sinus, orbital and paranasal regions), and lack of long-term stability make it unfavorable for long-term craniofacial implants [92,98,99]. Multiple studies have documented poor healing of CSD traumatic fractures for patients receiving standard-of-care medical treatments. Large gaps of missing bone in CSDs require fixative implants to provide structure and strength for load-bearing applications [100]. Consequently, various implant materials such as PEEK and Ti are widely employed for craniofacial reconstruction.

PEEK is used in a number of orthopedic applications including trauma, arthroplasty, and spinal fusion because of its biocompatibility, inert nature, and low elastic modulus [5]. PEEK's modulus is designed to mimic bone and therefore it minimizes stress shielding when compared to Ti [50,101]. Yet, PEEK's fundamental flaw is its lack of bioactivity which precludes any adequate biological or mechanical integration with bone. Its low surface energy, smoothness, and poor wettability limit osteoblastic differentiation and bone regeneration when compared to Ti [6–9]. Surface modifications and coatings (*e.g.*, HA, tricalcium phosphate (β-TCP), as well as plasma treatments, help facilitate cell adhesion, differentiation and overall integration with bone [5,10,102,103]. These coatings increase surface bioactivity but at the expense of reduced strength, particularly in the case of HA, [104–106] and reduced cellular growth for β-TCP [104]. These types of coatings show low bonding to PEEK, leading to poor interfacial interaction and delamination [106,107]. Although they are still under development, coated PEEK is less than ideal as a fixative implant material.

Titanium and its alloys are biocompatible and have an inherent ability to osteointegrate. They have been widely used in orthopedic, dental, skeletal, and craniofacial reconstruction for many decades [10,11]. Calcium phosphate coatings on Ti surfaces help increase its bioactivity and osteointegration [108–110]. However, complications, such as post implant fractures due to stress shielding, aseptic loosening [12–14], poor long-term stability, absence of antioxidant effects [15], and prolonged healing remain as critical issues. To improve outcomes of fracture repairs using Ti implants, HA coatings have been attempted [111–114]. However, these coatings proved to be unsatisfactory due to the thermal expansion mismatch at the Ti-HA interface [115–121], the poor quality of HA formed by plasma spraying [122–126], and poor long-term stability. Bioglass®, an alternative to HA, is also a mechanically weak biomaterial [115,127–129]. It similarly exhibits cracking at

the Ti-glass interface due to its brittleness and thermal expansion mismatch [130]. Additionally, composite coatings, based on HA and Bioglass®, demonstrated immature bone healing and fibrous tissue attachment after 12 weeks *in vivo* [131]. Although MgO or N_2-annealing reduced their thermal expansion mismatch and interfacial adhesion [132–134], these glasses and composites had reduced bioactivity due to the release of Mg^{2+} ions that down-regulated osteogenic markers [135]. Antibiotics [136] and coatings such as silver [137,138], zinc [139,140], copper [136], and fluoride [141] have been used to incorporate antibacterial effects on Ti surfaces to overcome secondary infections [108]. Yet, antibacterial coatings do not induce a more rapid osteoblast and bone growth response, which is needed for long-term osteointegration. Overall, the use of monolithic or coated PEEK and Ti implants for craniofacial reconstruction and orthopedic applications is still less than optimal for bone healing. Therefore, using an implant material with a surface that induces rapid osteoprogenitor growth is desirable.

Silicon nitride (Si_3N_4) is a novel biomaterial that has shown improved cyto-compatibility and biomineralization versus traditional hydroxyapatite [18,19]. It was cleared by the FDA for use in spinal fusion procedures in 2008 and serves as intervertebral spacers for stabilization of cervical and thoracolumbar spine. Studies have also been conducted on the development of Si_3N_4 for reconstructive applications [21] Si_3N_4 ceramics have high strength and fracture toughness, inherent phase stability, high wear resistance, low coefficients of friction, hydrophilicity, and biocompatibility [17]. These traits make it a material of interest for craniofacial and dental applications [16,20] Studies have also shown that Si_3N_4 is anti-infective and enhances osteogenic differentiation of mesenchymal and osteoblast cells when compared to Ti and PEEK [10,16,18,22–25,142]. Chemical modifications to the surface of Si_3N_4 enhanced its biomineralization relative to HA and other competitive bio-

materials [143]. This was attributed to many factors, including its surface chemistry, hydrophilicity, and its strong electronegative surface sites, which promoted cell attachment and migration when compared to HA, Ti, or PEEK [17,18,26]. Based on prior work with amorphous silicon nitride [144], the presence of surface nitrogen induces the formation of N-H moieties that act as precursors to the amide groups present in collagenous extra-cellular-matrix (ECM). This study will seek to determine if such functional group formation occurs on monolithic ceramic surfaces.

Thus, it is hypothesized that Si_3N_4 enhances osteoprogenitor cell adhesion and growth via higher surface energy and the presence of amide surface functional groups. The aim of this study was to correlate osteoprogenitor adhesion and growth to surface roughness, surface energy, and surface functional group formation in order to identify differences in the osteogenic potential of each implant material.

Materials and Methods

Study Design

The surface properties (roughness, energy, and functional groups) of each material before and after cell-free *in vitro* immersion were analyzed at the Center for Characterization of Materials and Biology at the University of Texas at Arlington (CCMB, UTA). Methods used to determine surface roughness included atomic force microscopy (AFM), contact, and non-contact surface profilometry. Contact angles of two different liquids were measured using sessile drop methods; the collected data were used for the surface energy calculations. *In-vitro* cell-free study using the alpha minimum essential medium (α-MEM) was conducted to study the biomineral formation on the surface. All samples were immersed in α-MEM and incubated at 37˚C in a humidified 5% carbon dioxide (CO_2) atmosphere for 1, 4, and 7 days. Surface functional group formation and biomineral characteri-

zation were investigated using Raman Spectroscopy, Fourier Transform Infrared Spectroscopy (FT-IR) analysis, high-resolution scanning electron microscopy (HR-SEM), and electron dispersive spectroscopy (EDX/EDS). *In-vitro* cell culture testing was conducted using murine calvaria osteoblast cells (MC3T3-E1) seeded onto each material's surface. Imaging of adherent cells and cell growth measurements were conducted using SEM and cell proliferation assays, respectively. Statistical evaluation of the surface property data and *in-vitro* results was used to determine significant differences between groups. These statistical analyses were conducted via analysis of variance (ANOVA) using the general linearized model in SPSS (SPSS software, IBM Corporation, Fishkill, NY). A post-hoc Tukey's analysis was used to determine statistical significance between each group. Statistical significance was signified by the following convention: *, $p < 0.05$, **, $p < 0.01$, and ***, $p < 0.001$.

Sample Preparation

Silicon nitride (Si_3N_4) samples were provided by Amedica Corporation (Salt Lake City, UT, USA). Details of their processing and basic properties are provided elsewhere [19,21]. This bioceramic has a nominal composition of 90 weight % (wt.%) Si_3N_4, 6 wt.% yttrium oxide (yttria, Y_2O_3), and 4 wt.% aluminum oxide (alumina, Al_2O_3). The Y_2O_3 and Al_2O_3 serve as densification additives. From this composition, a quantity of disc samples (Ø12.7 x 2.5mm) was prepared for characterization and biological testing. They were separated into two groups – as-fired and polished. The as-fired samples had no post-densification treatments whereas the polished samples were abrasively lapped to a near-mirror finish. Dimensionally identical samples were also prepared from PEEK (ASTM D6262, Ketron®PEEK 1000, Quadrant EPP USA, Inc., Reading PA, USA; distributed by McMaster-Carr, Santa Fe Springs, CA, USA) and a titanium alloy (ASTM F136, Ti6Al4V-ELI, distributed by Vincent Metals, Minneapolis, MN, USA). The Ti and PEEK samples were also produced in two groups – as-machined and polished – using 600 grit and 2000 grit abrasive

lapping, respectively. All samples were prepared at two different levels of roughness in an effort to examine each material's surface morphology with respect to *in vitro* osteoblast cell adhesion and growth.

Prior to all experiments, samples were immersed in 100% ethanol and ultrasonicated for 5 minutes to remove any possible surface debris. Prior to the *in vitro* studies, samples were gas sterilized using ethylene oxide for 12 hours and then vacuum desiccated for 24 hours to remove residual absorbed ethylene oxide gas. Surface cleaning and sterilization were conducted at standard temperature and pressure (*i.e.*, 25^{o}C and 1 bar).

Sample Characterization

A XANES study was used to determine the type of bonding that exists within the constituent surface elements of silicon nitride. The theory on XANES methodology can be found in Koningsberger and Roelof (1988) [57,145]. In this study, evaluations of the Si L-edge, and Y M-edge were conducted at the National Synchrotron Light Source facility (Canadian Light Source, CLS, University of Saskatchewan, Saskatoon, Saskatchewan, Canada). Details of the beam energy for each studied element are given in previous publications [144,146,147] and in the Results section below. XANES analysis was used to determine the presence of Si-O, Si-N, and Si-Si bonds and how the presence of Yttrium affects these coordination structures.

Three instruments were utilized in assessing the morphological surface features of the samples including atomic force microscopy (AFM, Park XE 70, Park Systems, Suwon, Korea), a contact stylus surface profiler (Alpha Step IQ, KLA Tencor Corporation, Milpitas, CA), and an optical profilometer (NPFLEX, Bruker, Billerica, MA). The stylus-based surface profiler analyzed thin-step heights, surface micro-roughness, and overall form error while providing sufficient vertical range for large topographical variations. The

optical profilometer performed analyses over a larger surface area via non-contact mapping in three dimensions. It captured surface topography images and provided estimates of the different surface roughness parameters that were representative of the entire sample. The optical profilometer overcame some of the limitations imposed by small area analyses using AFM, and features that are smaller than the stylus tip diameter of the contact profiler.

The contact angles of deionized water and diiodomethane (> 99% purity, Sigma-Aldrich, St. Louis, MO, USA) on the sample's surfaces were determined using sessile drop techniques. The images were captured using a high-speed camera (WATEC, high resolution, NAVITAR lens) synced to FTA32 software (First Ten Angstroms Inc, Portsmouth, VA). For each material, three samples were tested with 9 repetitive drops of DI water and diiodomethane at 25˚C. Surface tensions, (γ^{LV}), including polar (γ^{d}) and dispersive (γ^{p}) components, for water and diiodomethane were 72.8, 21.8, and 51.0 mJ/m^2 and 50.8, 50.4, and 0.4 mJ/m^2, respectively [71,72,147]. The surface energy of each sample was calculated using the Owens-Wendt-Kaeble equation as described in prior work [147].

Each material was imaged for their respective surface morphology using an Ultra HR-SEM (Hitachi S-4800 II FE SEM, Hitachi, Tokyo, Japan). Prior to imaging, the PEEK and Si_3N_4 samples were sputter-coated with conductive silver (CrC-100 sputter, Plasma Sciences Inc., Lorton, VA). Images were acquired at a working distance 10 mm under 20 kV and at different magnifications. EDS mapping of sample surfaces after 7 days of immersion in α-MEM was observed with an energy-dispersive x-ray spectroscope (EDS) detector connected with a Hitachi S-3000N Variable Pressure SEM.

FT-IR and Raman spectroscopy were used to characterize mineral formation on the surface of all samples. These samples were immersed in α-MEM for 7 days. Thermo Nicolet 6700 FT-IR Spectrometer (Thermo Electron Corporation, Madison, WI USA)

equipped with a smart attenuated total reflectance (ATR) accessory was used to collect the FT-IR absorbance spectra over the range of 4000-500 cm^{-1}, with an aperture 150, 128 scans, and resolution of 4 cm^{-1}. Raman spectroscopy (DXR, Thermo Scientific Waltham, MA, USA) with a 780 nm excitation laser at 100 mW, 10x objective, and a 50 µm slit was used for all samples except for PEEK, which needed a different setup (1 mW, 10x objective, and a 25µm pinhole). The samples were photo-bleached for 4 minutes prior to spectra collection and a 10 s exposure time was used. Thirty-two spectra per location were recorded within the range of 400 - 2000 cm^{-1}.

X-ray diffraction was used to investigate HA formation on sample surfaces after 7 days of immersion in α-MEM. A Siemens D500 XRD system was used to collect scans using Cu Kα radiation (λ = 1.5418 Å) at room temperature. Data were recorded over the 2θ range of 20−80° with a 0.04° step size and a dwell time of 1.5 seconds.

Free cells in vitro studies and Murine calvarial MC3T3-E1 osteoblast cells studies previously mentioned in detail in section 3.3.

Results

Fig. 4-1 represents the XANES measurements of silicon nitride's surface chemical coordination. The fluorescence signal (FY) data for Si L2, 3 edge (Fig. 4-1a) represents the absorption energy of the p core shell electrons for Si. Peaks a and b at 105.7 and 106.3 represent 2p spin orbital splitting, which was described previously [144,147]. These were observed in a shifted state in the as-fired and polished samples possibly indicating a change in the near-surface bonding of the Si atom. Transition of 2p to 3s/3d orbitals was observed at peak c near 108.1eV. Resonance peaks were observed in the post edge data for Si_3N_4 samples but not seen in Si_3N_4 model compound data. This could indicate a shape change in the orbital [58,148]. Finally, the pre-edge peak at 104.5 **+/-** 0.2 eV is the distinguishing peak between Si_3N_4 type bonding and SiO_2 type bonding. The pre-edge shoulder

at this energy signifies the presence of Si-O and Si-N bonding. These results therefore confirm the formation of a silicon oxynitride surface with a random mixing of Si-O and Si-N bonding.

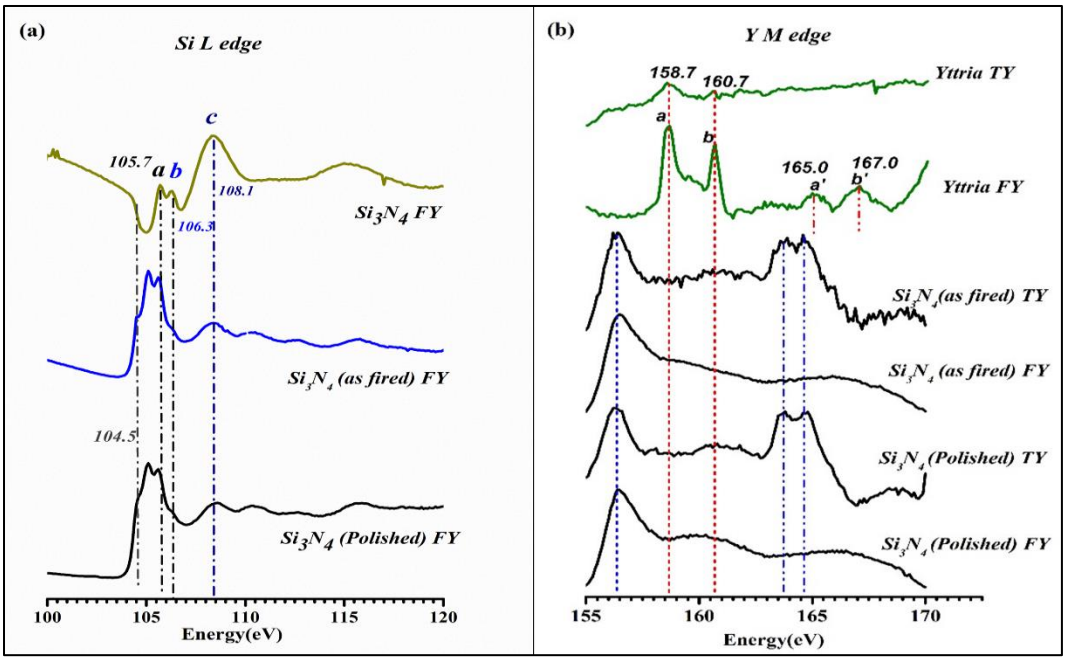

Figure 4- 1: XANES analysis of the as-fired and polished Si_3N_4 showing (a) Si-L2, 3 edge, and (b) Yttrium M-edge, (Total Electron Yield (TY) and Fluorescence signal (FY)).

Given in Fig. 4-1b is the total electron yield (TY) and fluorescence signal (FY) data for yttrium M edge which represents the absorption of d electrons. Peaks a and b represent $3d_{3/2}$ and $3d_{1/2}$ orbital activity. They are 2eV apart and are expected to occur at 155.7 and 157.7eV, respectively [94]. Their resonance feature was observed at a' and b'. The silicon nitride samples showed peaks a and b shifted to higher energies at 163.7 and 164.7 eV with just 1eV difference between them. The peak at 156.5 is likely due to N 1s peak resonance in the Y spectrum energy range. These shifts may have occurred due to a change in bonding or electrical coordination of elemental yttrium from its pure state as yttrium oxide

to its combination with Si_3N_4. These results therefore indicate the shift in binding energy for electrons on the surface, which contributes to the overall surface energy.

Surface roughness parameters collected from the three different measurement techniques are shown in Table 4-1. It is important to note that these different measurement methods confirmed that the polished silicon nitride samples had the lowest roughness parameters compared to the other samples. Results from both AFM (Fig. 4-2) and optical profilometer showed that the PEEK 600 grit samples had the highest Ra and Rq values. While the stylus profilometer was effective in measuring general surface parameters, the AFM and optical profilometer provided detailed three-dimensional characterization of each sample's morphological features as shown in Fig. 4-2. Thus, the average roughness according to the AFM and optical profilometer from highest to lowest was PEEK, 600 grit > Si_3N_4 as-fired > PEEK, 2000 grit > Ti6Al4V 600 grit > Ti6Al4V 2000 grit > Si_3N_4 polished. Both analyses confirmed the large difference in the surface topography between the as-fired and polished Si_3N_4, Ti6Al4V 600 grit and 2000 grit, and PEEK 600 and 2000 grit. As-fired Si_3N_4 showed a rougher and more granular surface whereas an even, non-granular surface was found for polished Si_3N_4.

Table 4- 1: Summary of the AFM, optical profilometer, and KLA Tencor roughness parameters; (Ra) roughness average and (Rq) the root-mean-square roughness of all samples.

Data samples	AFM		Optical Profilometer		Stylus Profilometer		AFM (After HA)	
	R_a	R_q	R_a	R_q	R_a	R_q	R_a	R_q
As-fired Si_3N_4	241	305	309	399	140	180	438	555
Polished Si_3N_4	31	36	9	13	4	6	561	702
PEEK 600 grit	295	357	496	619	122	155	405	508
PEEK 2000 grit	144	172	164	206	52	64	458	523
Ti6Al4V600 grit	135	166	140	183	38	53	226	300
Ti6Al4V2000 grit	64	83	89	120	17	24	429	563

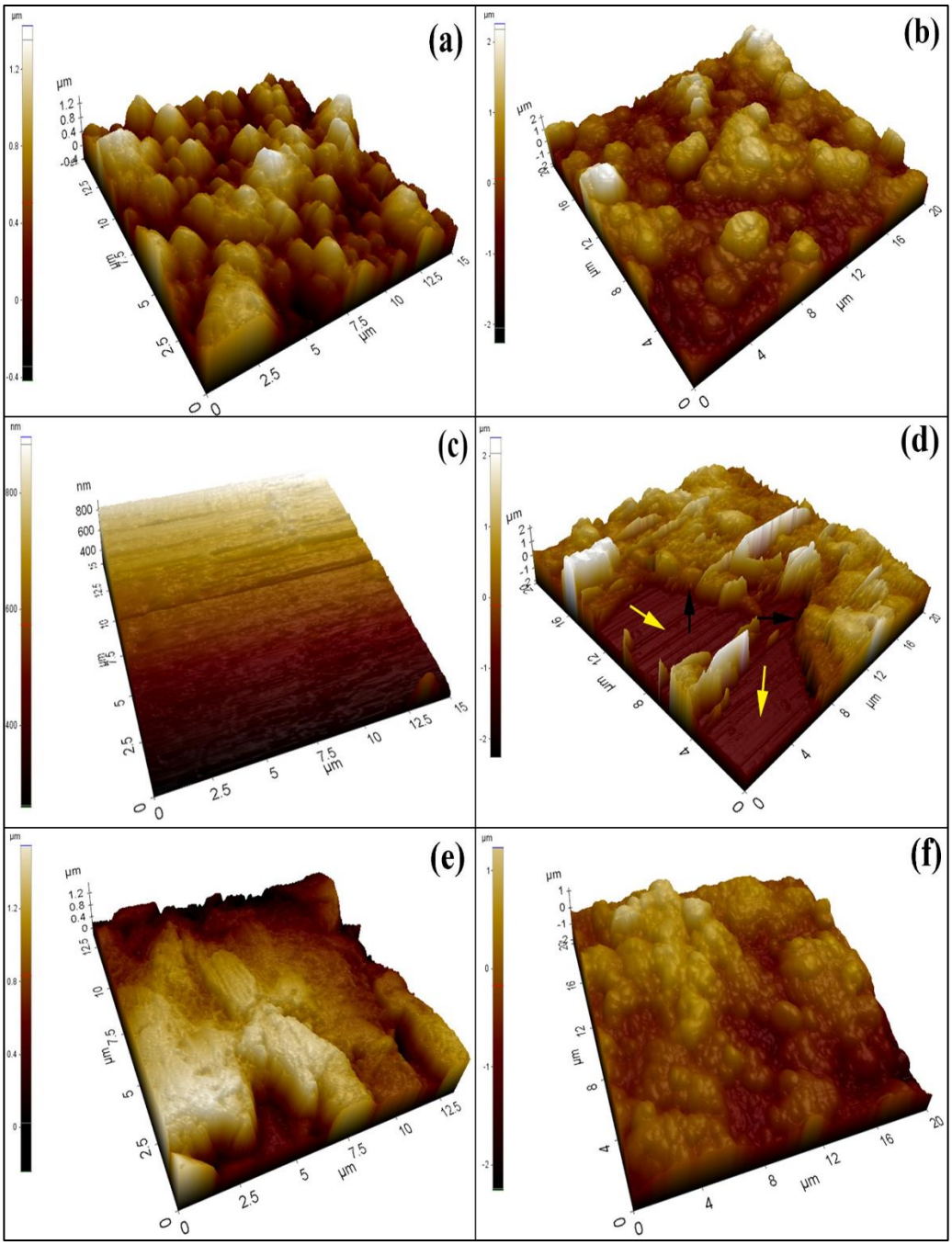

Figure 4-2: 3D-AFM images showing the surface topography before and after HA formation, respectively, (a, b) As-fired Si_3N_4, (c, d) Polished Si_3N_4, (e, f) PEEK, 600 grit, (g, h) PEEK, 2000 grit, (I, j) Ti6Al4V 600 grit, and (k, l) Ti6Al4V 2000 grit with color indicator bar.

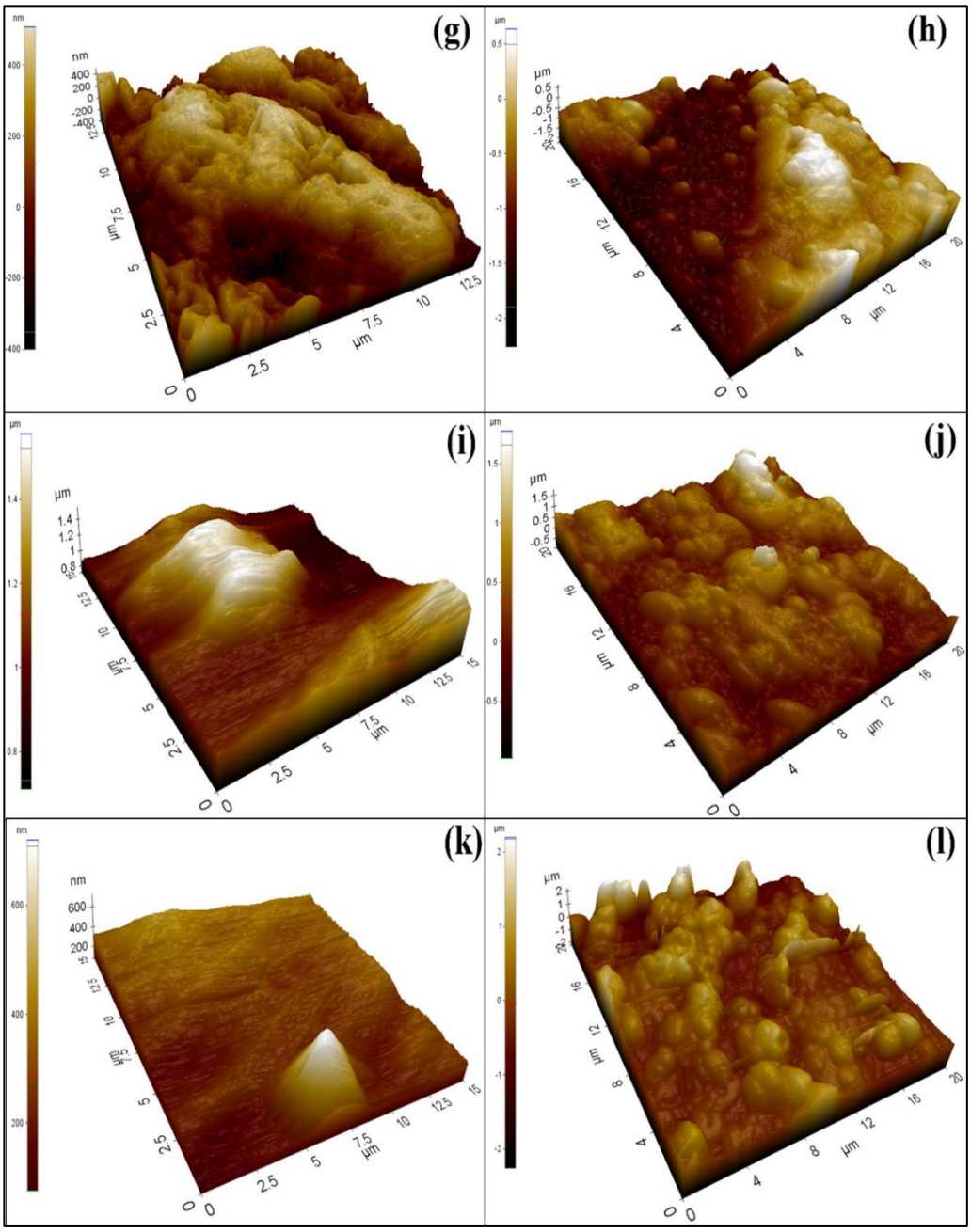

Figure 4-2: 3D-AFM images showing the surface topography before and after HA formation, respectively, (a, b) As-fired Si_3N_4, (c, d) Polished Si_3N_4, (e, f) PEEK, 600 grit, (g, h) PEEK, 2000 grit, (I, j) Ti6Al4V 600 grit, and (k, l) Ti6Al4V 2000 grit with color indicator bar (Cont.).

AFM 3D images of the surfaces of the tested samples after 7 days of incubation in α-MEM are shown in Fig. 4-2. After α-MEM immersion, each sample showed a "blister rough" surface compared to its bare surface (Fig. 4-2). This blister-shape is indicative of the formation of nanocrystalline HA. Furthermore, the roughness parameters for all samples increased, which further suggests the deposition of HA. In particular, Fig. 2(d) displays the topography of the polished Si_3N_4 sample after HA formation. This image clearly shows HA growth on the Si_3N_4 bare surface; the yellow arrows indicate the bare surface and the black arrows refer to HA crystals formation. Table 4-1 presents the average roughness of the HA layer and indicates that the HA crystals on the as-fired Si_3N_4 had the highest roughness of any surface, also confirming the highest HA density on this surface.

Fig. 4-3 provides the static water contact angles for each tested surface. Fig. 4-4a shows the variation of contact angles on the sample surfaces with water and diiodomethane. Fig. 4-4b presents the calculated surface energies (γ) broken into polar γp and dispersive γd components for each tested sample. It was observed that the magnitude of contact angle decreased as the surface roughness of the sample decreased. This was exemplified by comparing the contact angles for the as-fired silicon nitride (Θ=65.13°, Ra=309.27 nm) and polished silicon nitride (Θ=55.31°, Ra=9.32 nm). A similar result was observed for the Ti and PEEK samples. The effect of surface polishing reduced the prominence of peaks and valleys. This minimized entrapped air at the liquid-solid interface thereby reducing the contact angle [149]. Fig. 4-4c shows deionized water contact angles for all samples before and after immersion for 1, 4, and 7 days in α-MEM. The contact angles of all samples decreased within the first day. Remarkably, the contact angles for the as-fired and polished Si3N4 samples decreased from 65.13˚+/- 2.9˚and 58.50˚+/- 1.7˚ to 7.31˚+/- 4.1˚ and 7.05˚+/- 3.15˚, respectively, during the first day and then gradually decreased to 0˚ and 2.89˚ after 7 days.

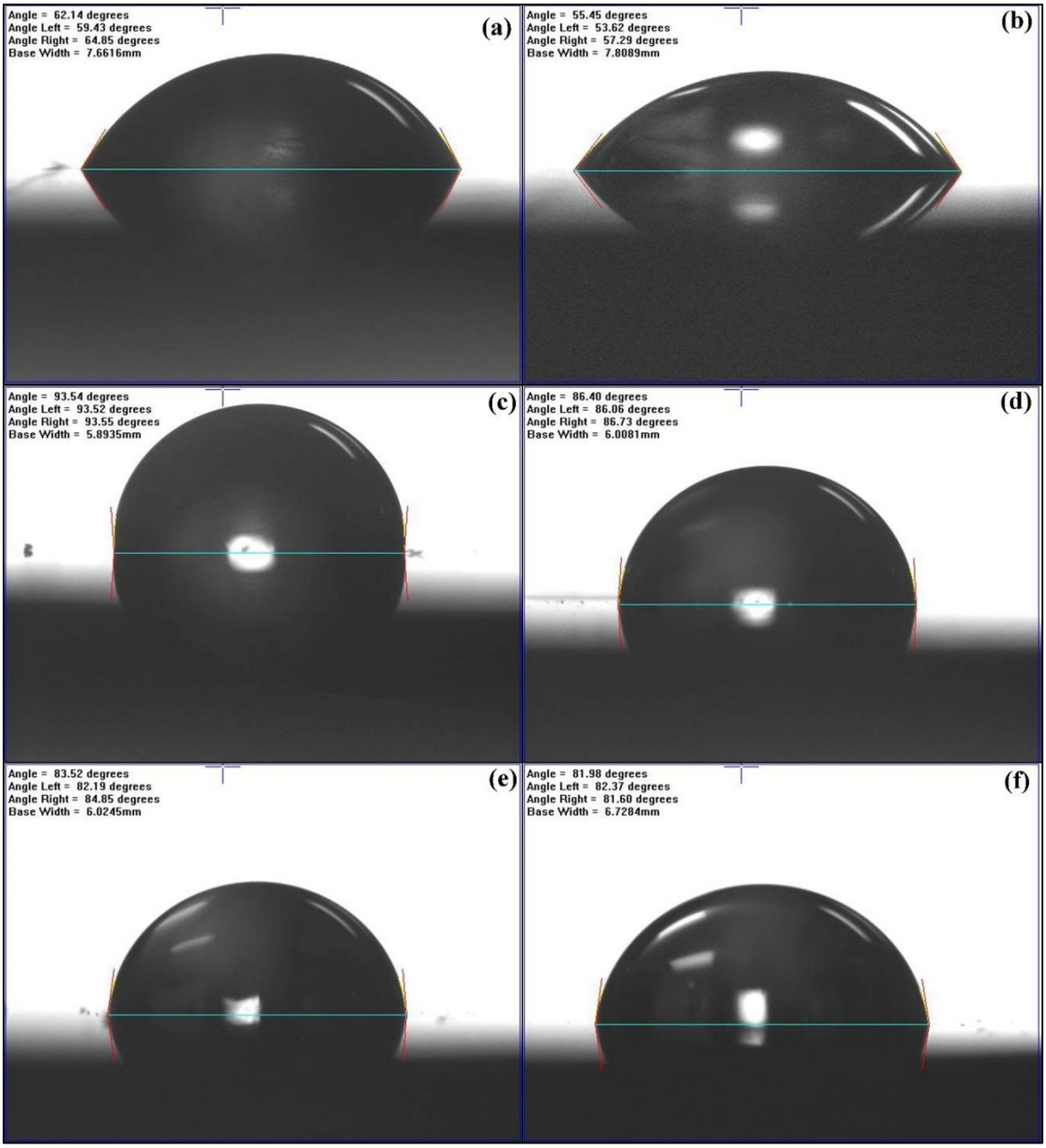

Figure 4-3: Static contact angle images of water on the surface of (a) As-fired Si_3N_4, (b) Polished Si3N4 (c) PEEK, 600 grit, (d) PEEK, 2000 grit, (e) Ti6Al4V 600 grit, and (f) Ti6Al4V 2000 grit. The Si_3N_4 samples show an acute angle suggestive of hydrophilic surfaces as compared to PEEK and Ti.

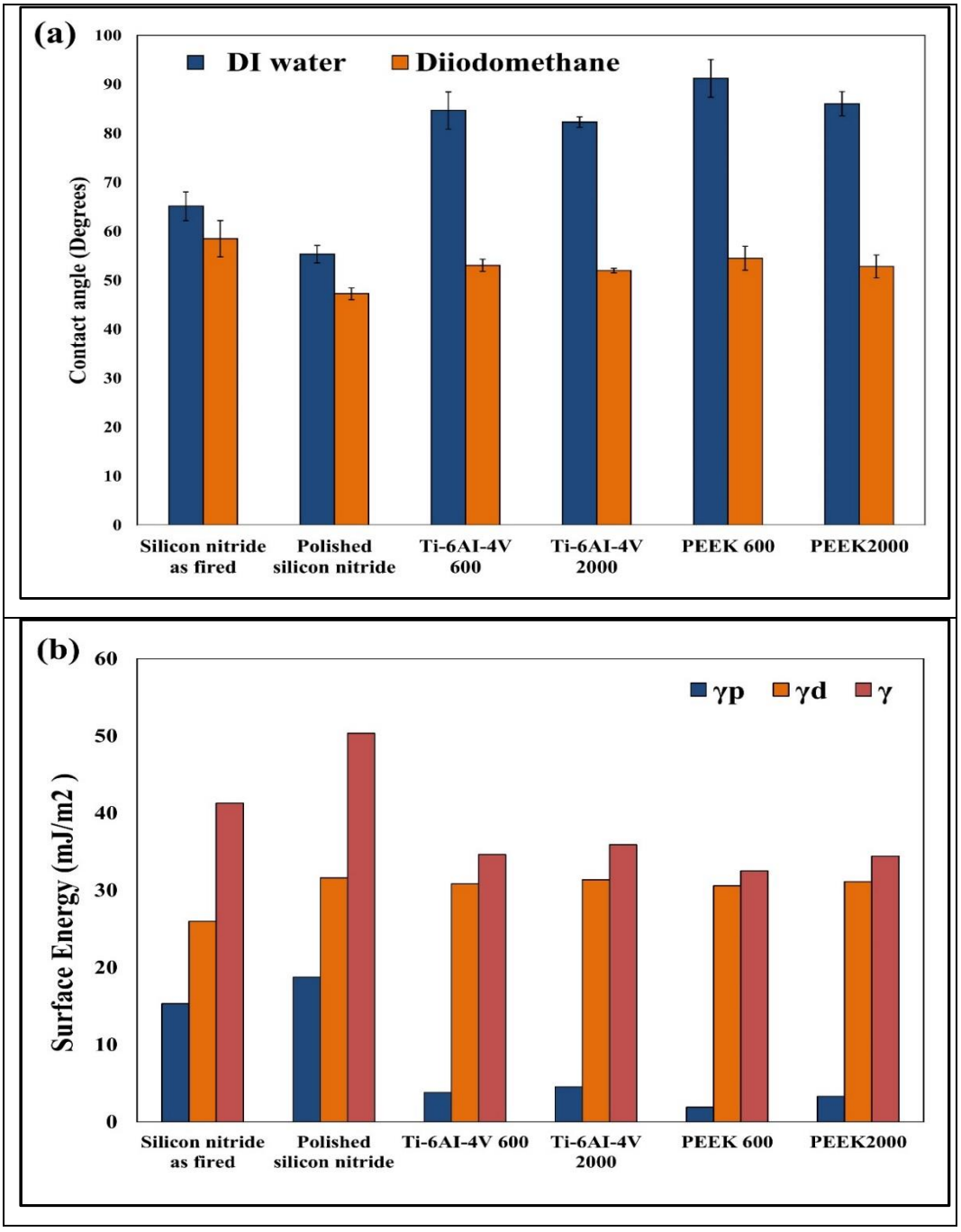

Figure 4-4: Contact angle and surface energy show (a) variation of contact angle on samples sur-face with water and DIM with error bars showing standard deviation, and (b) calculated surface energy (γ) for all samples, broken into polar γp and dispersive γd components, (c) variation of contact angle of DI water before and after immersion in α-MEM with error bars indicating the standard deviation.

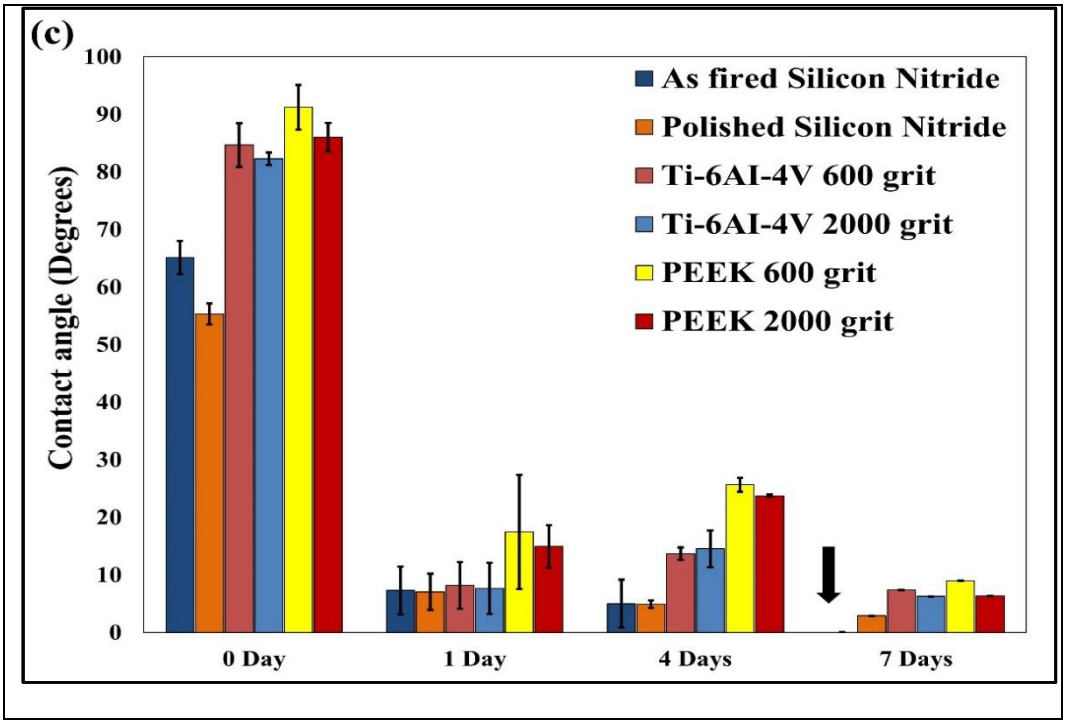

Figure 4-4: Contact angle and surface energy show (a) variation of contact angle on samples sur-face with water and DIM with error bars showing standard deviation, and (b) calculated surface energy (γ) for all samples, broken into polar γp and dispersive γd components, (c) variation of contact angle of DI water before and after immersion in α-MEM with error bars indicating the standard deviation (Cont.).

SEM images of the bare samples surfaces' and the nanocrystalline HA formed on these surfaces with their representative EDS spectra are presented in Fig. 4-5. Although, these images provide clear evidence for the formation of HA on the surfaces of all samples, it was noted that its highest density and largest coverage occurred on the as-fired and polished Si_3N_4 samples. This also was confirmed from the measured HA-layer thickness as shown in the cross-section SEM images presented in Fig. 4-6 (a, b, and c). These images clearly delineated the HA layer on each sample's surface and allowed an estimate of its thickness using imaging software. The measured HA thickness exhibited the highest value of 54.8 +/- 4.3 μm on the as-fired Si3N4 surface compared to 20.5 +/- 3.5 μm, and 15.9 +/- 2.3μm for Ti6Al4V 600 and PEEK 600 grit samples, respectively as presented in

Fig. (6-d). Fig. 4-6-e shows the Ca/P ratio calculated from the EDS elemental analysis. The Ca/P ratio for HA formation on the as-fired and polished Si_3N_4 was 1.32 +/- 0.03 and 1.42 +/- 0.16, respectively. PEEK samples showed Ca/P ratio relatively similar to Si_3N_4, while HA formation on Ti surface had a lower Ca/P ratio, which indicates Ca deficiency in the surface formed HA layer.

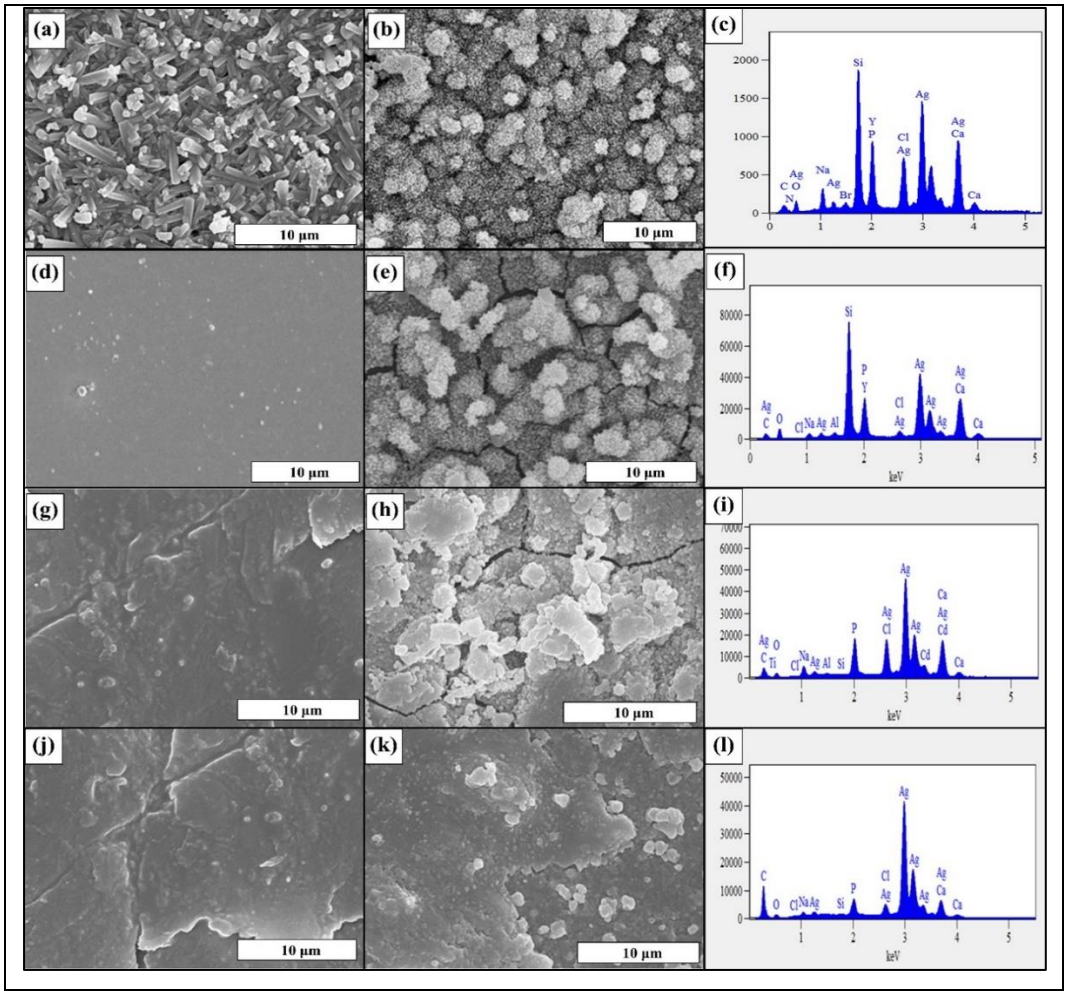

Figure 4-5: HR-SEM images before and after 7 days in α-MEM of (a, b) as-fired Si_3N_4, (d, e) Polished Si_3N_4, (g, h) PEEK, 600 grit, (j, k) PEEK, 2000 grit, (m, n) Ti6Al4V 600 grit, and (p, q) Ti6Al4V 2000 grit. EDX spectra of (c) as-fired Si_3N_4, (f) Polished Si_3N_4 (i) PEEK 600 grit, (l) PEEK 2000 grit, (o) Ti6Al4V 600 grit, and (r) Ti6Al4V 2000 grit after 7 days in α-MEM.

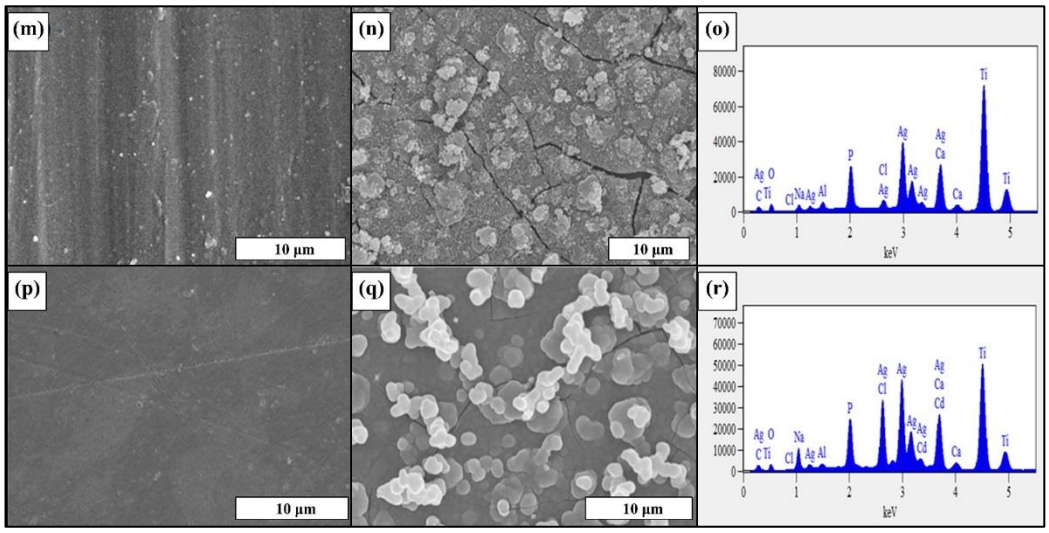

Figure 4-5: HR-SEM images before and after 7 days in α-MEM of (a, b) as-fired Si_3N_4, (d, e) Polished Si_3N_4, (g, h) PEEK, 600 grit, (j, k) PEEK, 2000 grit, (m, n) Ti6Al4V 600 grit, and (p, q) Ti6Al4V 2000 grit. EDX spectra of (c) as-fired Si_3N_4, (f) Polished Si_3N_4 (i) PEEK 600 grit, (l) PEEK 2000 grit, (o) Ti6Al4V 600 grit, and (r) Ti6Al4V 2000 grit after 7 days in α-MEM (Cont.).

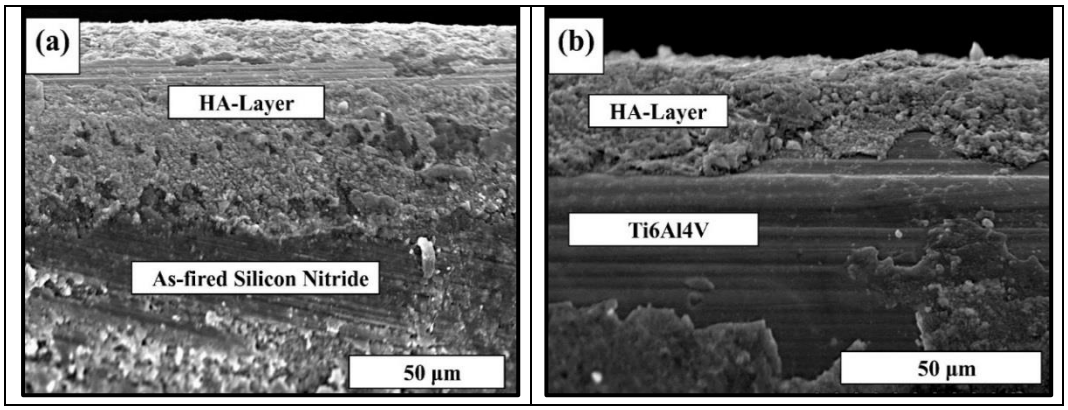

Figure 4-6: SEM images show the interface between the formed HA layer and the (a) As-Fired Si_3N_4, (b) Ti6Al4V 600 grit, and (c) PEEK 600 grit samples surfaces, (e) HA-Layer thick-ness (µm), and Ca/P ratio with standard deviation bar, calculated from the EDS data.

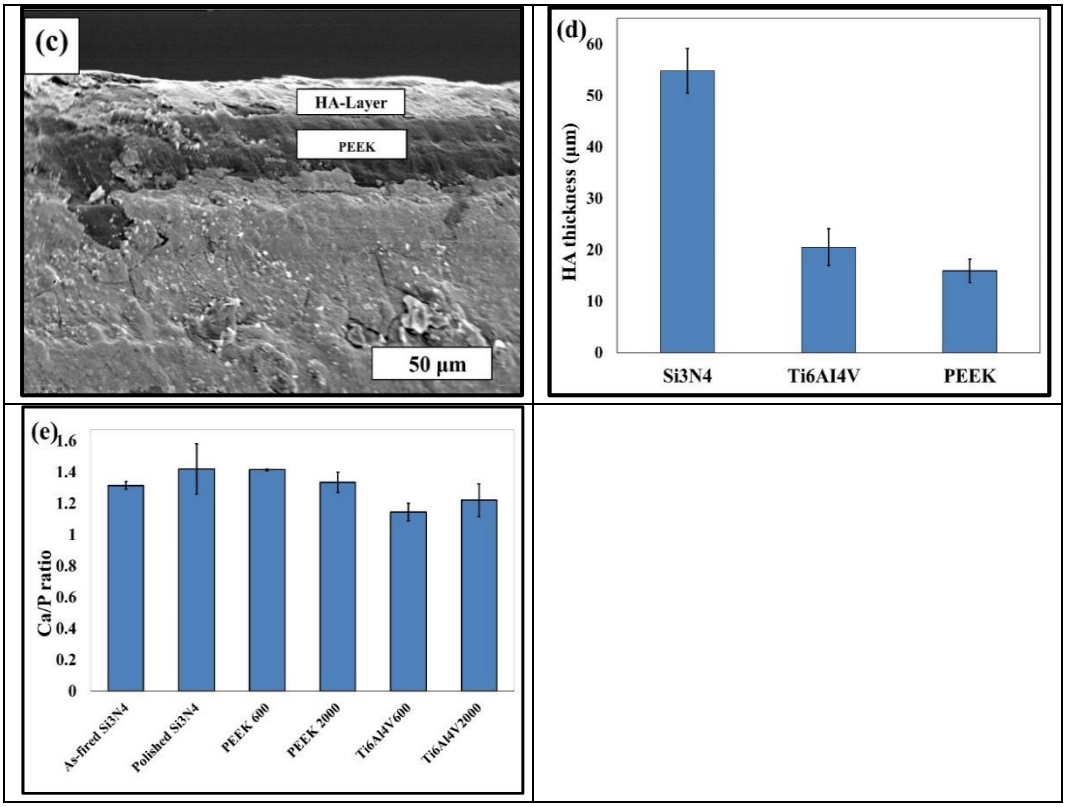

Figure 4-6: SEM images show the interface between the formed HA layer and the (a) As-Fired Si_3N_4, (b) Ti6Al4V 600 grit, and (c) PEEK 600 grit samples surfaces, (e) HA-Layer thick-ness (µm), and Ca/P ratio with standard deviation bar, calculated from the EDS data (Cont.).

Fig. 4-7 shows the surface morphology, composition and element distribution on the surface of all samples after 7 days immersion in α-MEM. EDS mapping showing the regions of interest corresponding to Si, Ca, P, O, N, Na, and Al K edges were defined for all samples. EDS results confirmed the presence of Ca and P deposition on the surface of each sample that previously indicated by the SEM images. It is important to note that the arrows drawn on each image indicate the regions of high Ca and P deposition density compared to the main elements distribution of the sample. For example, in the as-fired Si_3N_4 sample, the arrows refer to the high Ca and P deposition density that slightly shield the Si_3N_4 surface and show less Si density at these regions.

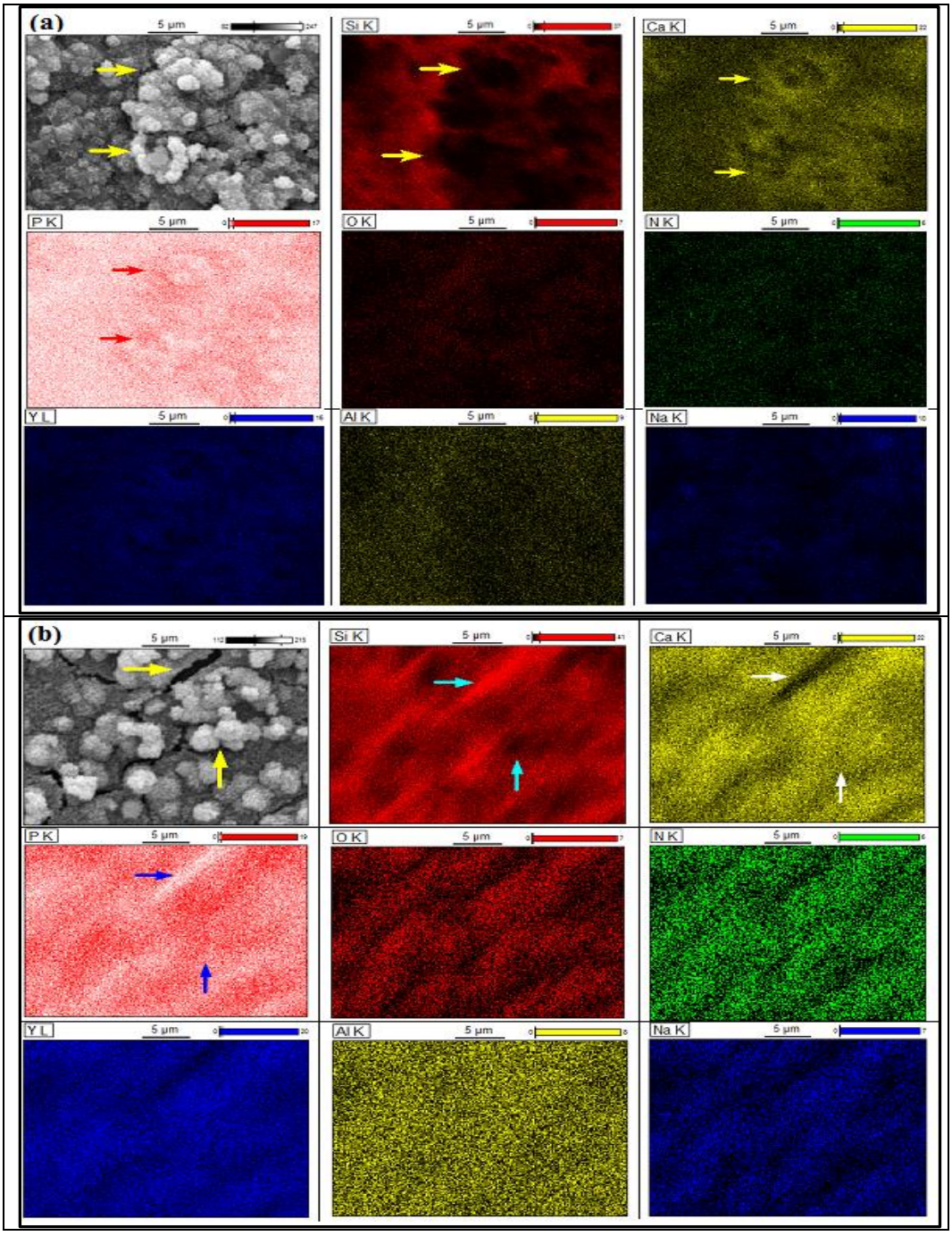

Figure 4-7: EDS surface mapping of (a) as-fired Si_3N_4, (b) Polished Si_3N_4, (c) PEEK, 600 grit, (d) PEEK, 2000 grit, (e) Ti6Al4V 600 grit, and (f) Ti6Al4V 2000 grit after 7 days immersion in α-MEM.

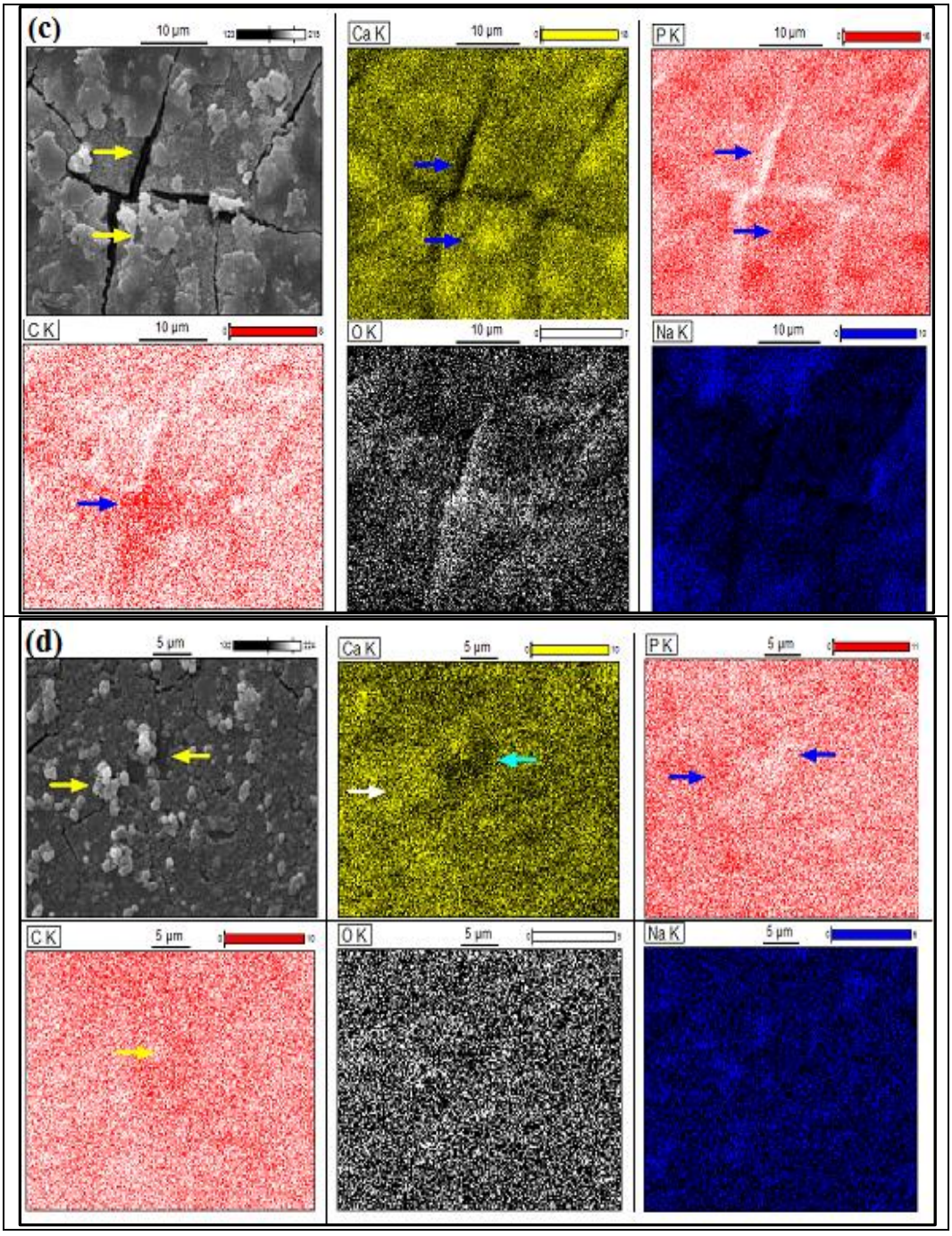

Figure 4-7: EDS surface mapping of (a) as-fired Si_3N_4, (b) Polished Si_3N_4, (c) PEEK, 600 grit, (d) PEEK, 2000 grit, (e) Ti6Al4V 600 grit, and (f) Ti6Al4V 2000 grit after 7 days immersion in α-MEM (Cont.).

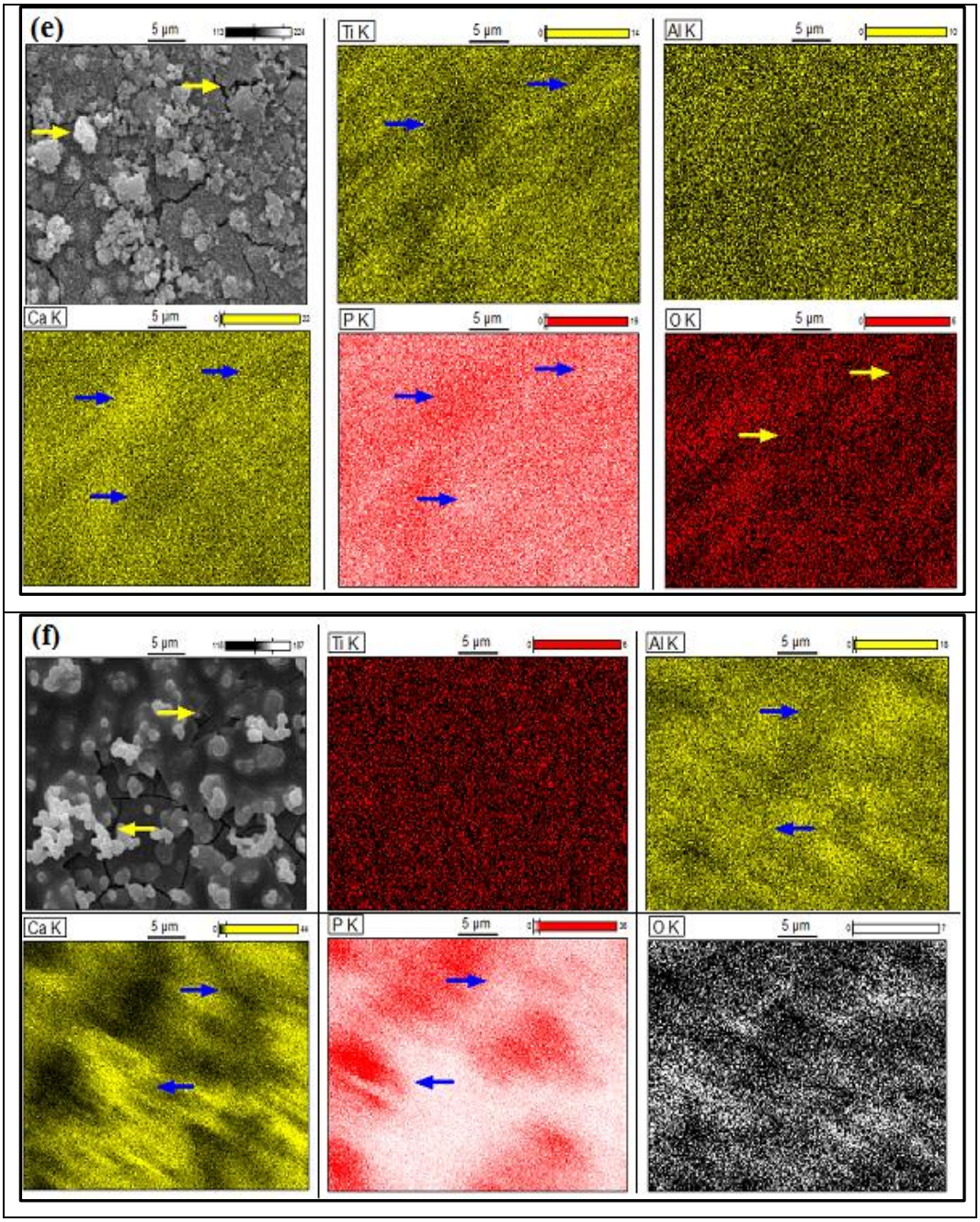

Figure 4-7: EDS surface mapping of (a) as-fired Si_3N_4, (b) Polished Si_3N_4, (c) PEEK, 600 grit, (d) PEEK, 2000 grit, (e) Ti6Al4V 600 grit, and (f) Ti6Al4V 2000 grit after 7 days immersion in α-MEM (Cont.).

Characterization of bare and in vitro immersed surfaces by Raman spectroscopy after 1, 4 and 7 days of incubation in α-MEM is given in Fig. 4-8. Silicon nitride and Ti surfaces showed the formation of carbonate and phosphate peaks from the first day of immersion, while PEEK samples exhibited very little to no phosphate or carbonate species formation after day 7. Only, silicon nitride surfaces indicated the presence of amide, and hydroxyproline peaks from day 4 of immersion. The amide and phosphate peaks on Si_3N_4 surfaces increased in height as a function of in vitro immersion time, indicating their stability to remain bound to this bioactive surface.

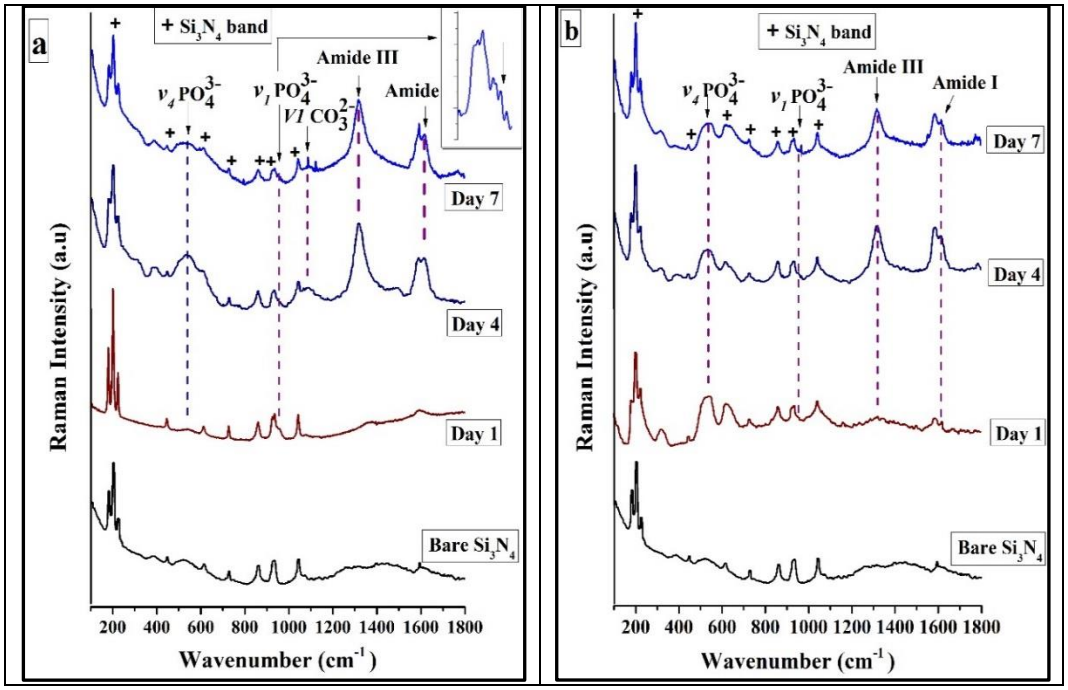

Figure 4-8: Raman Spectroscopic graphs for the bare and the immersed samples surfaces (1, 4, and 7 days) of (a) as-fired Si_3N_4, (b) Polished Si_3N_4, (c) PEEK, 600 grit, (d) PEEK, 2000 grit, (e) Ti6Al4V 600 grit, and (f) Ti6Al4V 2000 grit.

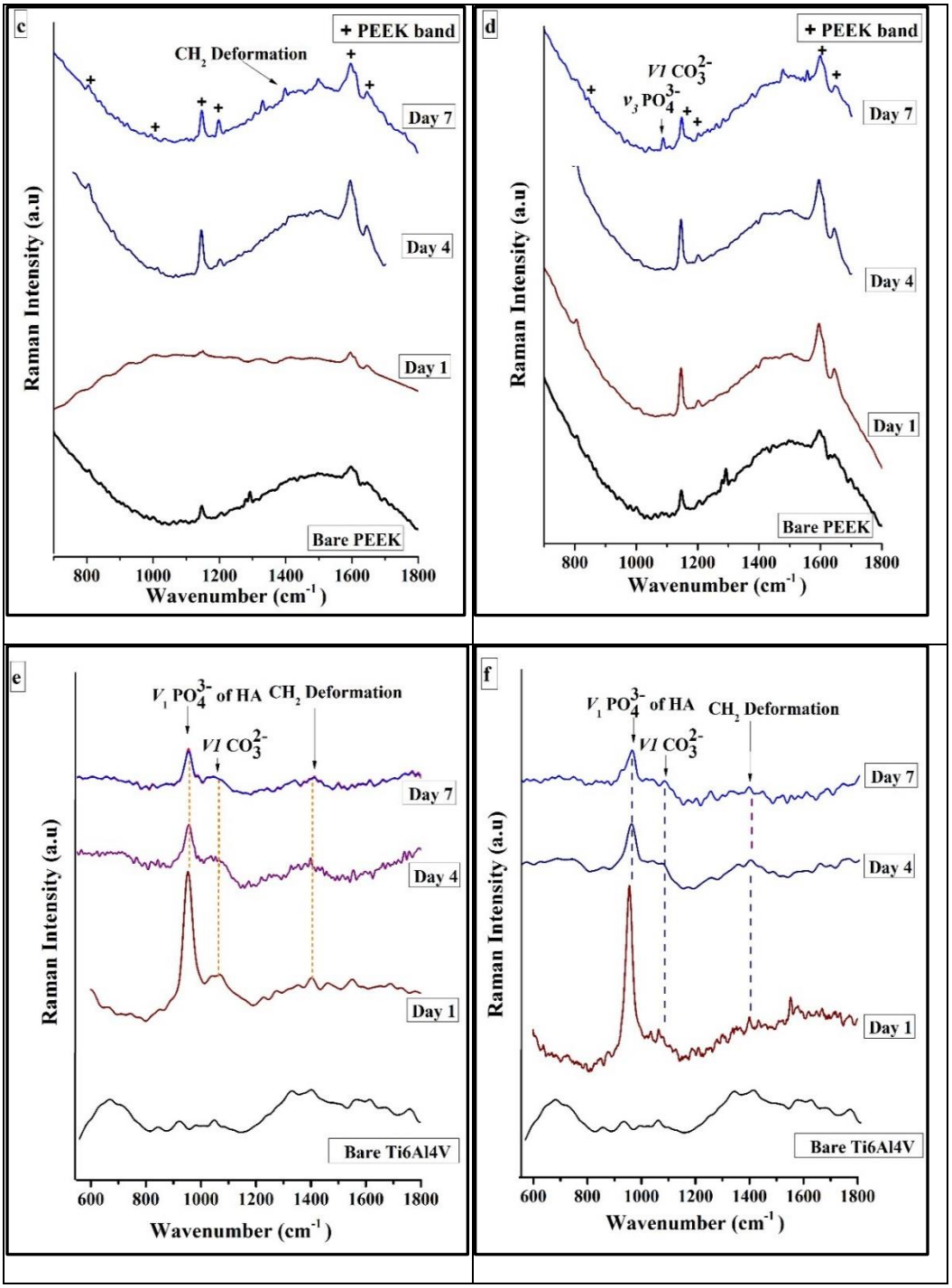

Figure 4-8: Raman Spectroscopic graphs for the bare and the immersed samples surfaces (1, 4, and 7 days) of (a) as-fired Si_3N_4, (b) Polished Si_3N_4, (c) PEEK, 600 grit, (d) PEEK, 2000 grit, (e) Ti6Al4V 600 grit, and (f) Ti6Al4V 2000 grit (Cont.).

FT-IR spectra of all samples after 7 days immersion in α-MEM confirmed the formation of HA as presented in Fig. 4-9. These spectra indicated the presence of characteristic absorption bands for the vibrational modes of PO_4^{3-} that appeared around 1019, 962, and 600 cm^{-1}. The broad band that appeared at 3350-3550 cm^{-1} corresponded to strongly adsorbed and/or bound H_2O, as well as the weak bands of OH^- group that appeared at 3572 and 595 cm^{-1}. Furthermore, the observed bands at 1420-1465 and 875 cm^{-1} were attributed to the CO_2^{3-} group that substituted for the phosphate group in the apatite structure. These spectra are in agreement with other published data of the HA [150–154]. Of all the samples, only Si_3N_4 showed a weak broad band at 1600-1650 cm^{-1} corresponding to the N-H of amide I, which can explain the presence of amide peaks found in the Raman spectra.

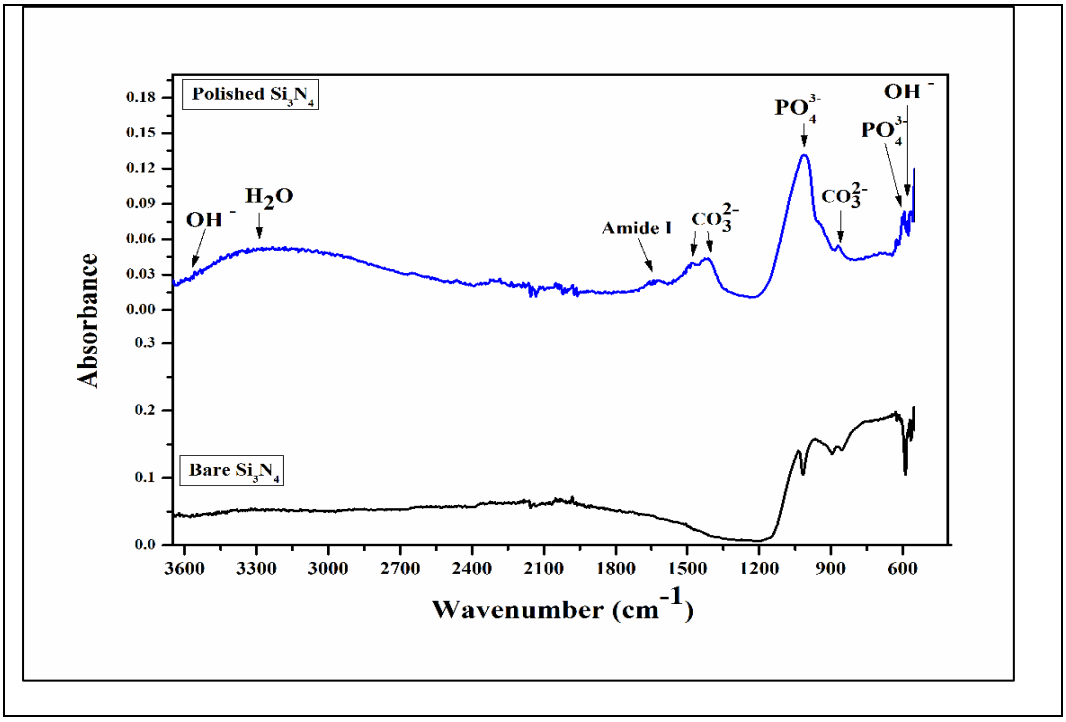

Figure 4-9: FT-IR spectrum of HA formation on the surface of Polished Si_3N_4, PEEK, 2000 grit, and Ti6Al4V 2000 grit.

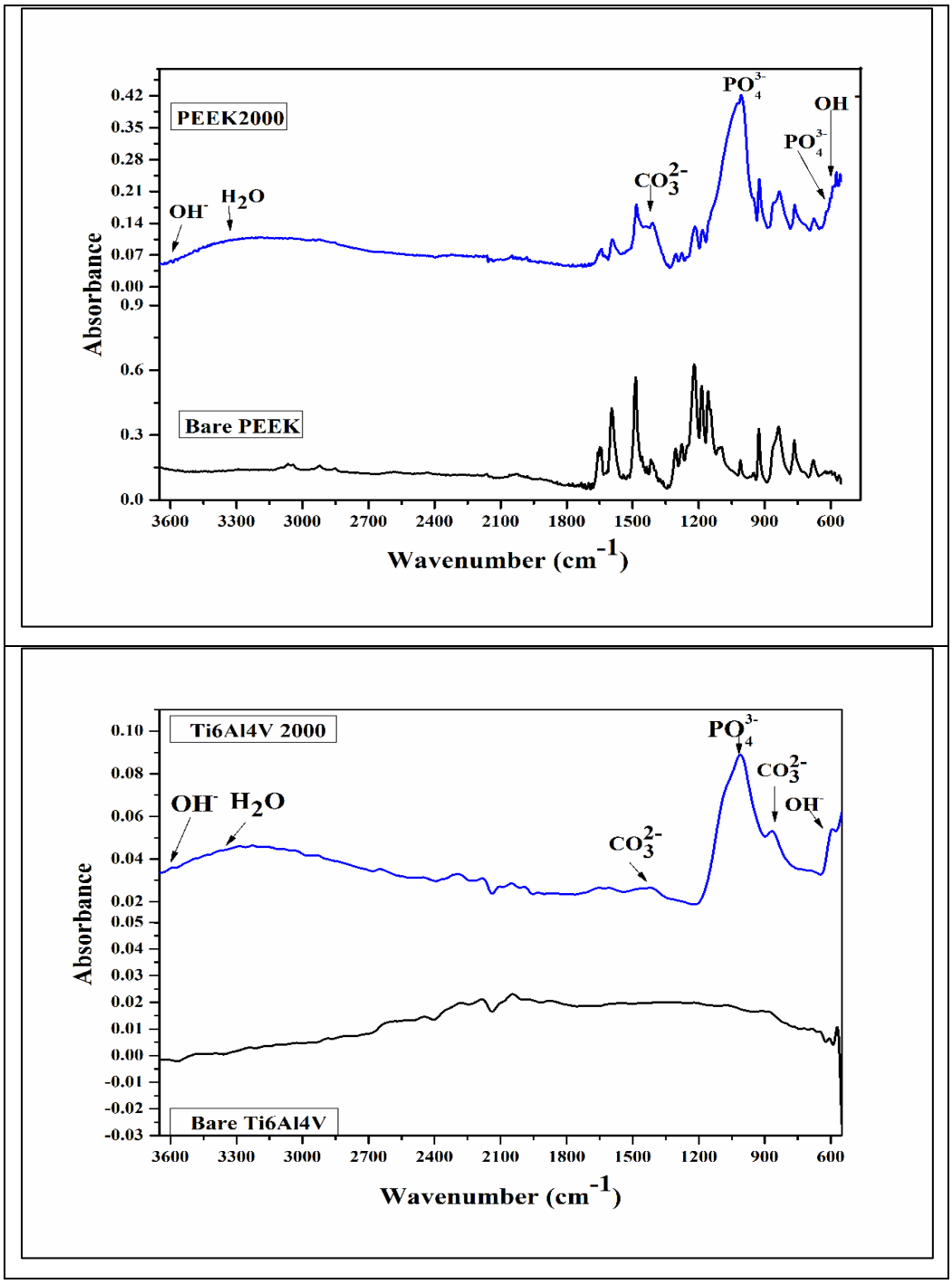

Figure 4-9: FT-IR spectrum of HA formation on the surface of Polished Si_3N_4, PEEK, 2000 grit, and Ti6Al4V 2000 grit (Cont.).

To confirm the presence of HA layer formation on the samples' surfaces, the structure of the formed layer compared to the bare samples surfaces was investigated by X-ray diffraction analysis. The patterns presented in Fig. 4-10. XRD analysis supported the SEM, Raman, and FT-IR results that indicated the formation of HA layer after *in vitro* testing. When the bare and the immersed surfaces of each sample were compared, two newly formed peaks appeared at 32° and 46° 2θ that related to (211) and (203) planes, respectively, of the nanocrystalline hydroxyapatite. The grain size of these HA crystals on each surface was estimated using the Debye-Sheerer relation [74,155,156]. The estimated values confirmed that the grain size increases from 30.4 nm for the polished Si_3N_4 to reach 48.20 nm for the PEEK 2000 grit sample; this increase can explain the highest intensity of the (211) peak for PEEK 2000 grit sample. The lack of the "needle-like" structure of HA and more of a "flower-like" porous structure as seen in SEM images concur with the oriented polycrystalline grains seen in Fig.4-5. The (203) peak shift was likely due to a slight change of lattice parameters associated with compression or tension within the HA lattice.

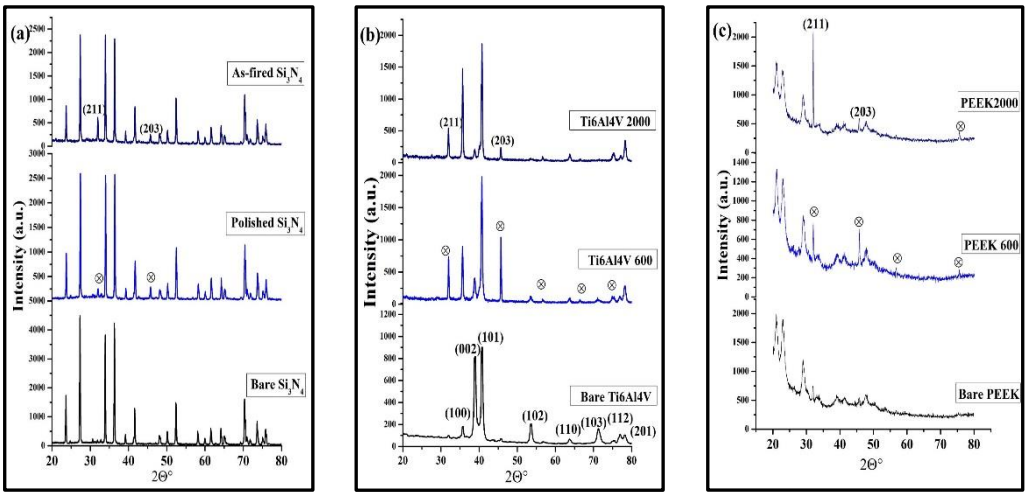

Figure 4-10: XRD results for: (a) Bare Si_3N_4, Polished Si_3N_4+HA, and As-fired Si_3N_4+HA; (b) Bare Ti6Al4V alloy, Ti6Al4V 600 grit +HA, and Ti6Al4V 2000 grit+HA; (c) Bare PEEK, PEEK 600 grit +HA, and PEEK 2000 grit +HA.

Fig. 4-11 shows the cellular adhesion on polished surfaces of silicon nitride, titanium and PEEK. Fig. 4-11a shows more cell spreading and a higher density of well-adherent cells on the surface of silicon nitride than PEEK (Fig. 4-11c); however, it had comparable density and cell spreading to titanium (Fig. 4-11b). The images indicate polished silicon nitride and titanium are suitable surfaces for proliferation of osteoblasts.

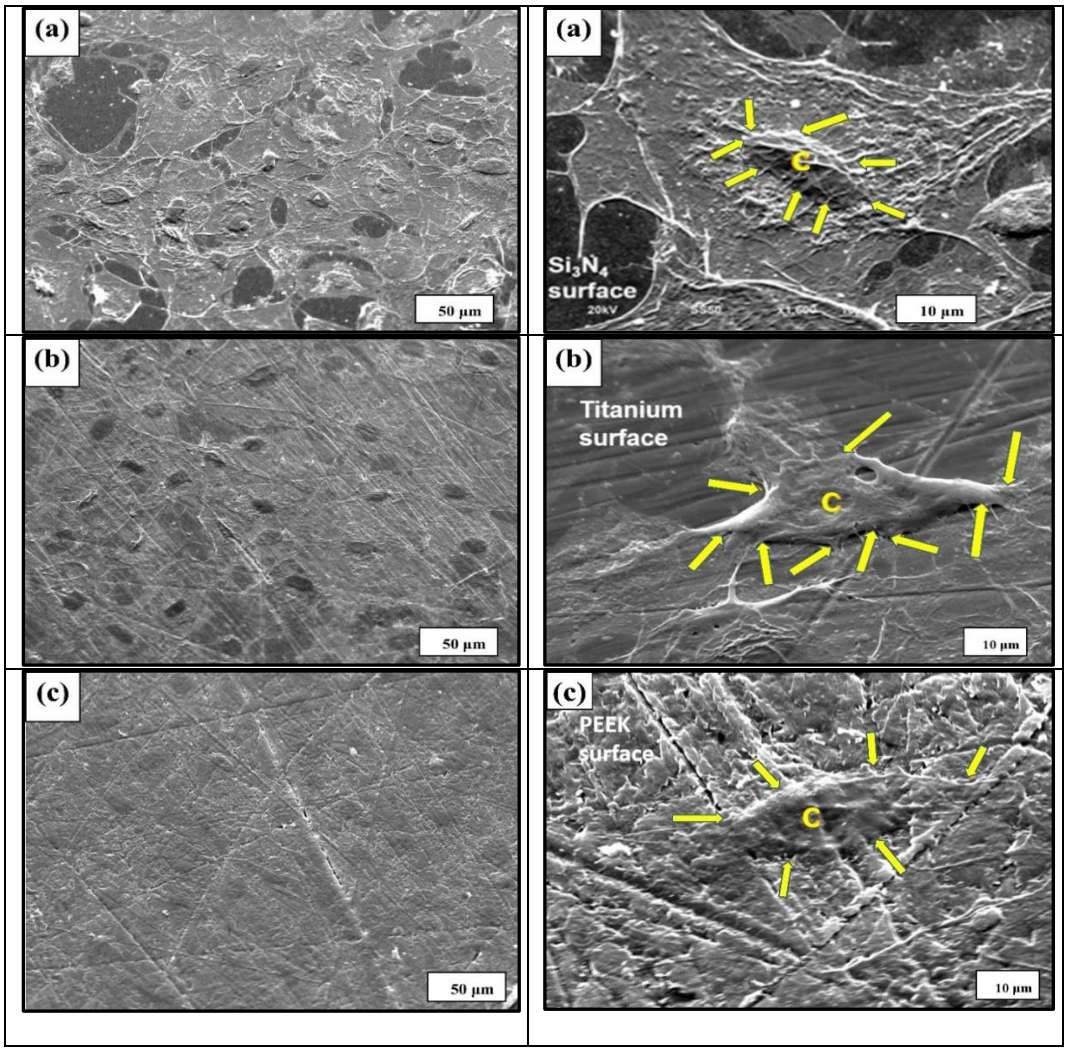

Figure 4-11: SEM images of cell adhesion on (a) Silicon Nitride (as-fired), (b) Ti6Al4V (as-machined), and (c) PEEK (as-machined), C represents the cell and yellow arrows shows the filopodia on these surfaces, (d) and (e) represent cell proliferation (MTS assay) with MC3T3-E1 cells, (d) shows as machined PEEK, Ti6Al4V, and as fired Si_3N_4, (e) shows polished samples of PEEK, Ti6Al4V, and Si_3N_4.

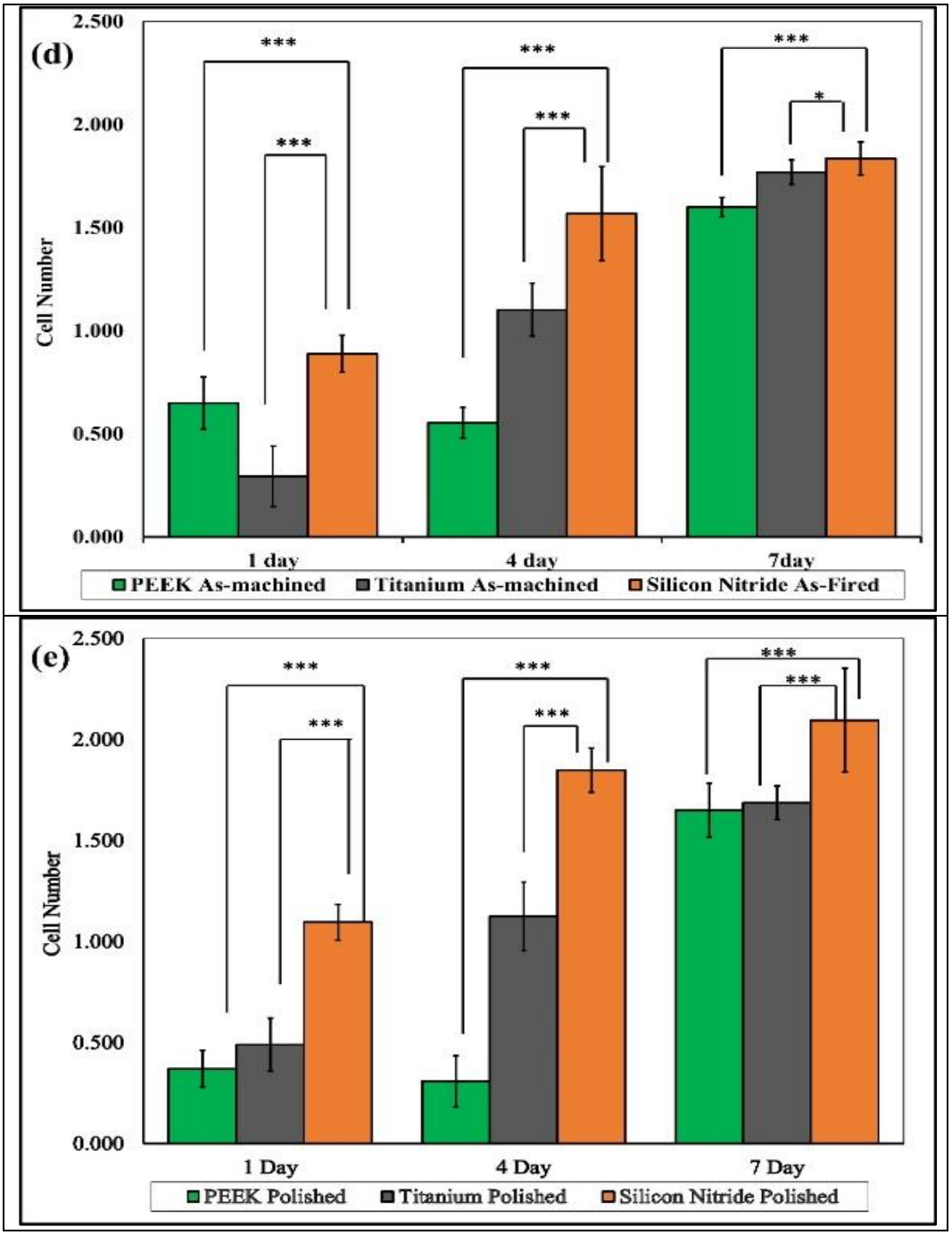

Figure 4-11: SEM images of cell adhesion on (a) Silicon Nitride (as-fired), (b) Ti6Al4V (as-machined), and (c) PEEK (as-machined), C represents the cell and yellow arrows shows the filopodia on these surfaces, (d) and (e) represent cell proliferation (MTS assay) with MC3T3-E1 cells, (d) shows as machined PEEK, Ti6Al4V, and as fired Si_3N_4, (e) shows polished samples of PEEK, Ti6Al4V, and Si_3N_4 (Cont.).

Fig. 4-11 (d, e) shows cell proliferation on the different surfaces. Fig. 4-10d compares as-fired silicon nitride, as-machined titanium and PEEK and Fig. 4-11e shows cellular proliferation on the polished surfaces for 1, 4 and 7 days. It was found that Si_3N_4 out-performs Ti and PEEK at a very early stage of seeding (1 day). Silicon nitride also facilitated significant proliferation of cells as compared to Ti and PEEK after 7 days of culture. This suggests that Si_3N_4 had a higher affinity for cell attachment at an early time-point and it more readily facilitated cellular proliferation.

Discussion

The aim of this study was to characterize the surface properties of three clinically relevant biomaterials – Si_3N_4, Ti, and PEEK – and subsequently assess their impact on the adhesion and proliferation of calvarial osteoprogenitor cells. Each material was tested at two different average surface roughnesses. In addition to roughness, surface energy and surface functional group formation were also examined (after *in vitro* immersion). In *in vitro* cell-free testing, silicon nitride surfaces formed the highest and most dense nanocrystalline HA layer. Silicon nitride (either as-fired or polished) out-performed titanium and PEEK in promoting osteoprogenitor cell growth. Cells were highly dense and well-adherent when in contact with the silicon nitride surfaces.

The increased cell growth on the Si_3N_4 samples was due in part to the difference in surface energy when compared with titanium and PEEK. Each material was evaluated for its surface energy by measuring the contact angle of polar and non-polar solvents. It is well-understood that the surface energy depends on the number of dangling or broken bonds [157–159]. By increasing the density of dangling bonds, the surface energy increases and the contact angle decreases. For the Si_3N_4 samples, the significant decrease in the contact angle can be attributed to the precipitation of calcium phosphates out of the α-MEM solution onto the sample surfaces that led to the formation of hydroxyapatite as

confirmed by XRD and from the SEM images. The HA significantly enhanced the hydrophilic character of the surface which ultimately promoted cell differentiation and proliferation. For both PEEK and Ti6Al4V samples, their contact angles decreased significantly after the first day, but slightly increased again after 4 days. This later increase could be attributed to unstable precipitates on their surfaces. Conversely, the Si_3N_4 surfaces showed evidence of increased bonding density of other functional groups (amide I, amide II, hydroxyproline, and CH_2) that were absent on the Ti and PEEK surfaces. The presence of these functional groups may explain why the Si_3N_4 samples' surface energies remained relatively low after 4 and 7 days as compared to Ti and PEEK.

The presence of surface functional groups on silicon nitride can also help explain the differences in cell adhesion and growth when compared to titanium and PEEK. On the one hand, titanium and PEEK surfaces also showed formation of HA crystals. On the other hand, the Si_3N_4 surfaces appeared to form other functional groups that are present in collagenous extracellular matrix. The analysis by SEM of these surfaces showed a higher density of nanocrystalline HA as compared to titanium and PEEK (Fig. 7). The nanocrystalline HA appeared to exhibit a porous, "flower-like" structure. Indeed, this structure was confirmed by XRD to be consistent with nanocrystalline HA. [150,160,161]. Elemental analysis by EDS showed that the Ca/P ratio of the HA on the as-fired Si_3N_4 surface was 1.32. This ratio has been associated with octa-calcium phosphate (~1.3 – 1.33) which is a precursor to hydroxyapatite [162]. Interestingly, the polished Si_3N_4 surfaces induced nanocrystalline HA with a Ca/P ratio of 1.42, which is close to that of native HA ($Ca_{10}(PO_4)_6(OH)_2$: Ca/P = 1.66). For Ti or PEEK, nanocrystalline HA was confirmed with similar Ca/P ratio as that of as-fired Si_3N_4. Furthermore, the formation of HA structures on the Si_3N_4 surfaces was similar to that found in prior studies on amorphous silicon nitride [147]. Combining the results from the SEM, EDS, XRD, and Raman spectroscopy analyses, it is reasonable to

attribute the enhanced osteoblast growth on the Si_3N_4 surfaces to the presence of these surface functional groups, relatively dense nanocrystalline HA formation, and relatively high surface energy (*i.e.*, low wetting angles). This contrasts with the Ti and PEEK samples which showed lower osteogenic effects.

In a prior study using amorphous silicon oxide, silicon oxynitride, and silicon nitride [144], the addition of nitrogen caused the surface silicon dioxide to become a mixture of both tetrahedral and trigonal coordination. The added N caused an increase in the carbonate/phosphate ratio and N-H bond density prior to testing in cell culture. It was also observed that a large density of collagenous ECM formed on this silicon nitride surface, and it was speculated that the increased N-H bonding could be integrated into the structure of the collagen via amine group bonding to the material's surface [147]. In other investigations, it was found that N increased the expression of enzymes associated with collagen cross-linking such as superoxide dismutase and lysil oxidase [146]. The results from XANES analysis confirmed the presence of Si-O and Si-N bonding on the Si_3N_4 surface. Thus, it is reasonable to suggest that the surface of Si_3N_4 may have the presence of a silicon oxynitride layer. Future investigations will attempt to uncover this effect and provide evidence of the important role of nitrogen in bone regeneration and the impact of the Si-O-N elemental system on collagen formation.

It is known that nanometer size HA is the nuclei on which osteoblast cells build apatite crystals. However, these HA crystals are believed to form in the intracellular space [163]. Pezzotti and colleagues have observed similar findings in high-resolution transmission electron microscopy [17] . Nevertheless, the spontaneous formation of Ca-P or HA on Si_3N_4 in absence of cells has never been reported on the Si_3N_4 surfaces. However, our group has reported on this formation in previous work on silicon oxide, silicon oxynitride

coatings [144,146,147]. Kokubo et al. has extensively reported on the spontaneous formation of CaP on titanium and other implantable polymers [164]. Thus, it was not surprising that precipitation of CaP crystals occurs when simulated body fluid (or cell culture medium) is used as an immersion environment. The formation of the amide peaks was also not surprising given prior results indicating that its formation occurs as a result of hydrogen bonding to the silicon-nitrogen-oxygen (Si-O-N) surface [147]. Therefore, the formation of carbonate, phosphate, calcium, amide, and hydroxyproline on these surfaces appears to be a characteristic solely observed on Si-N, Si-O, and Si-O-N elemental constituent surfaces.

It is not well-understood why there are delays in osteoprogenitor growth on Ti and PEEK surfaces as compared to Si_3N_4. For titanium, this could be due to the self-passivating nature of its surface with the formation of a TiO_2 layer. Although this layer promotes osteoblast attachment, it does not resorb [165]. For PEEK surfaces, osteoprogenitor cells have demonstrated poor proficiency to differentiate into an osteoblast lineage and remain fibrogenic [6–9]. In this work, the key differences between these surfaces are their relatively low surface energies, a lack of surface functional groups that act as precursors for collagenous ECM formation, and relatively sparse deposition HA crystals. Conversely, the surfaces of Si_3N_4 have been shown to exhibit Si-O and Si-N bonding as well as the formation of functional groups that promote collagenous biomineral deposition. This surface has been shown in a prior study to enhance osteogenic growth, collagen formation, and osteogenic marker expression [147]. It may be possible that the absence of amide and hydroxyproline causes delays in healing due to the relatively slow-growth of osteoblasts on Ti and PEEK surfaces. Future work will further analyze the effect of surface functionalization of silicon nitride on osteogenesis and possibly angiogenesis.

The ability of a material to induce rapid cell growth is an indicator of its potential to hasten healing and improve the potential for osteointegration by facilitating cellular attachment and growth. In the application of these materials in bone fixation, each has shown varying effects on promoting bone growth. Based on the results of this study, the various surfaces of silicon nitride exhibited high surface energy (*i.e.*, low wetting angles) which facilitated the rapid growth of cells. These are promising signs that silicon nitride could be a viable alternative relative to titanium and PEEK for use in craniofacial bone defect reconstruction and where osseous integration is desired This is coupled with the fact that prior work also showed the positive impact of silicon nitride on osteogenesis and bone regeneration. Further investigation in potentially integrating silicon nitride on bone regeneration and reconstruction in complex craniofacial defects, fractures and as implants is underway. It is clear from the current work coupled with prior studies that silicon nitride plays a significant scientific role in collagen formation, biomineral deposition, and enhanced osteoblast proliferation.

Conclusions

In this study, a comparative analysis of the effect of surface properties of various fixative bone implant materials was conducted. Silicon nitride, titanium, and polyetheretherketone were compared. It was found that cells were well-adherent, relatively high in density, and grew at a relatively faster rate on silicon nitride surfaces as compared to titanium and PEEK. Silicon nitride's surface energy and surface functional group formation were determined to contribute to this result. Silicon nitride surfaces exhibited lower contact angles (*i.e.*, higher surface energy) and were deemed more hydrophilic as compared to titanium or PEEK. Their improved wettability facilitated increased potential for cell migration and growth. This favorable wetting was coupled with the rapid formation of nanocrystalline HA along with amide functional group precursors important for collagen formation. Titanium

and PEEK did not exhibit this coupled effect; therefore, it is concluded that the higher surface energy, formation of collagen precursor functional groups, and biomineral on the surface of silicon nitride enabled well-adherent and rapid growing cells as compared to titanium and PEEK.

Acknowledgements

The authors thank Dr. G. Pezzotti at the Ceramic Physics Laboratory, Kyoto Institute of Technology and Dr. Likith V. Reddy at Department of Oral and Maxillofacial Surgery, Texas A&M, College of Dentistry for helpful discussions. The authors also thank Drs. Bryan J. McEntire, Ryan M. Bock, and B. Sonny Bal of Amedica Corporation for their assistance in providing samples and their sponsorship of this study under grant # M1701379 (Varanasi, PI)

CHAPTER 5

MATRIX DEPOSITION STUDY

Introduction

It is well known that any tissue is composed of cells surrounded by extracellular matrix (ECM). This ECM consists of a unique three dimensional structure of specific molecules that secreted by the resident cells [166]. ECM is composed of proteins including collagens and proteoglycans. Collagens include collagen, laminin, fibronectin, hyaluronan and proteoglycans such as beta glycan, decorin, and perlecan. ECM of various bone tissue compartments plays an important role in directing the remodeling of the bone [167]. Furthermore, ECM formed by the osteoblast makes up most of the dry weight of bone [81]. Mechanical properties of the skeleton are controlled by the bone ECM. Mineralized portion of the bone tissue provides hardness and rigidity, while flexibility is provided by the organic component of the ECM. Calcium-phosphate is the main component of the mineralized portion of ECM and present in the form of hydroxyapatite, plus an extensive type I collagen-rich organic ECM [81]. This organic part, mainly type I collagen, serve as a scaffold upon which minerals is deposited [81,167]. So, ECM produced by the osteoblast plays an important role in the minerals deposition as well as supports a complete biomaterial osseointegration [168].

This chapter will provide a comprehensive investigation of the ECM deposition after 30 and 60 days of seeding MC3T3-E1 osteoblast cells. FT-IR analysis will compare the bare sample surface to its relevant after the matrix deposition. SEM imaging will represent clear view of the surface after collagen fibers and minerals formations. Also, EDS spectra and mapping will be provided to allow an extra evidence of the minerals and collagen formation on the top of each sample after the matrix deposition.

Results and Discussion

5.1 Fourier Transform Infrared Spectroscopy Analysis:

To identify the organic and inorganic components of the ECM environment on the surface of each sample, FT-IR analysis within 600-2000 cm^{-1} spectral range have performed. Figure 5-1(a, b, c) show the FT-IR spectra of the samples after the matrix deposition study for 30 days. It is noted

that both Si_3N_4 (Polished and as fired) and Ti (600 and 2000 grits) samples support collagen fibers and minerals formation. On Si_3N_4 and Ti surfaces, the spectra showed several vibrational bands related to the ECM component, such as ECM proteins (collagen) and P-O bonds of PO_4^{3-} ions.

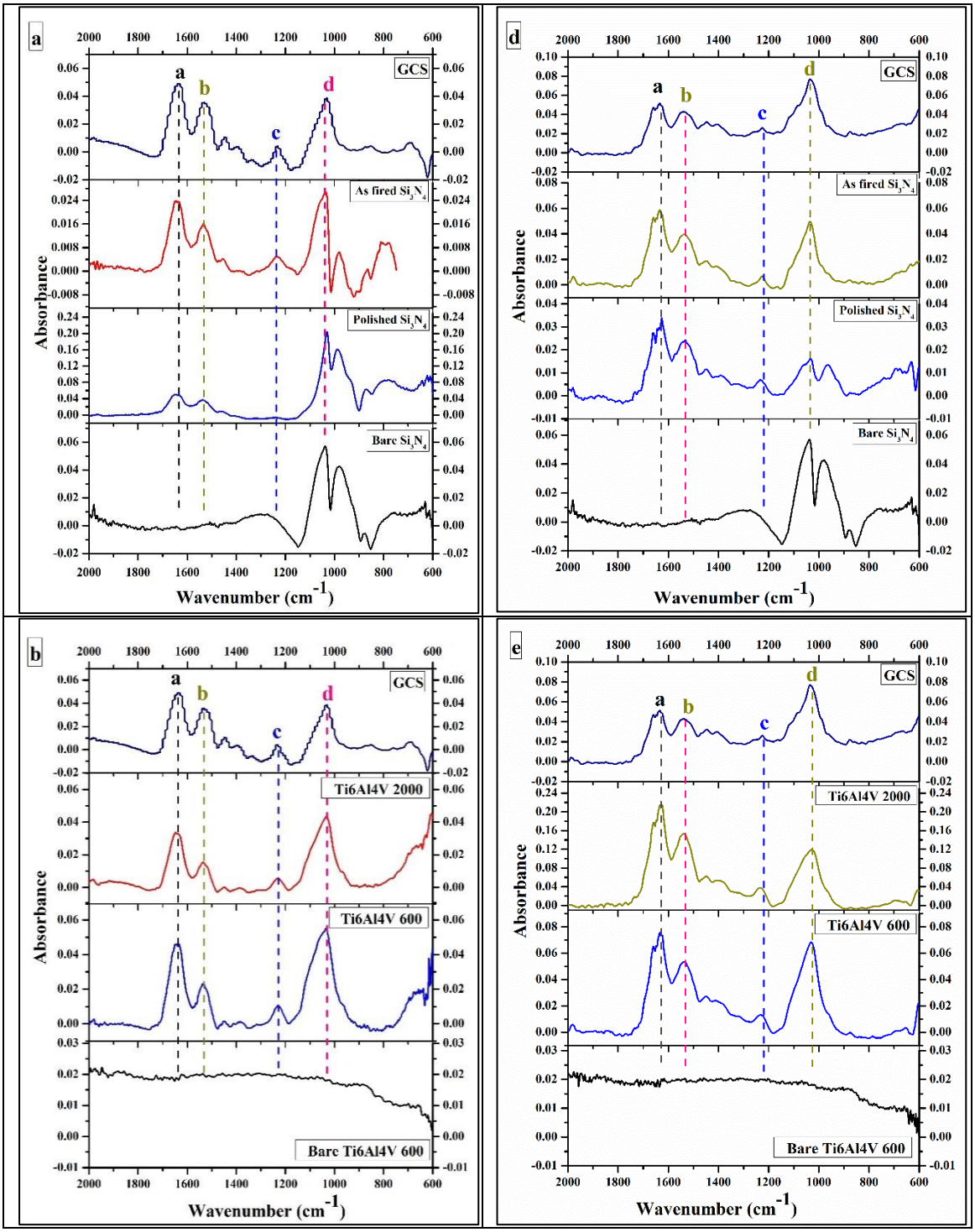

Figure 5-1: FT-IR spectrum of Si_3N_4, Ti6Al4V, and PEEK samples showing the matrix deposition after 30 days (a, b, and c), and 60 days (d, e, and f) of in vitro study.

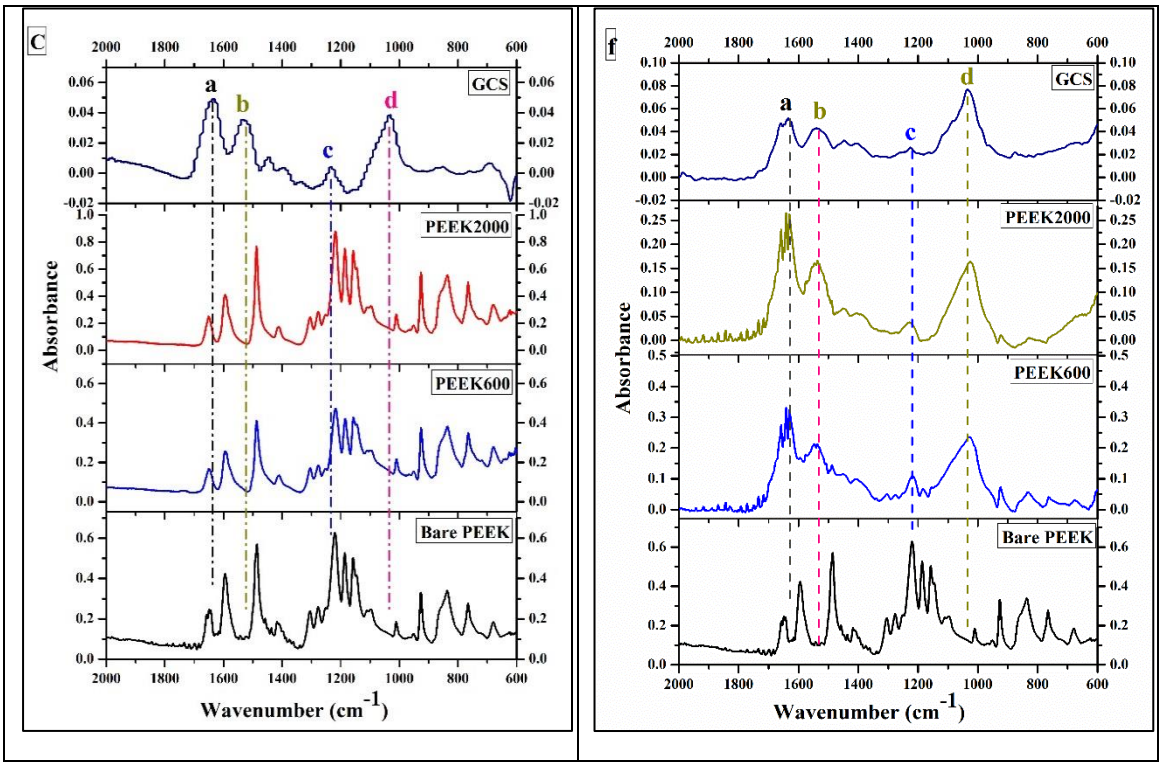

Figure 5-2: FT-IR spectrum of Si_3N_4, Ti6Al4V, and PEEK samples showing the matrix deposition after 30 days (a, b, and c), and 60 days (d, e, and f) of in vitro study (Cont.).

The vibrational bands of amide I (peak a at 1637 cm^{-1}), amide II (peak b at 1532 cm^{-1}), and amide III (peak c at 1228 cm^{-1}) indicative of ECM proteins were detected in both Si_3N_4 and Ti samples. Presence of the stretching P-O bond of PO_4^{3-} at 1030 cm^{-1} confirms the minerals formation" inorganic components of the ECM" on Si_3N_4 and Ti surfaces. The vibrational bands of ECM proteins and P-O stretching agree with various ECM FT-IR analysis in literature [169][170]. Furthermore, the presence of single broad peak spanning by 900– 1200 cm^{-1} refers to the formation of amorphous calcium phosphate (ACP) that usually characterized in FTIR spectra by a broad single peak at this range [169]. On the other hand, PEEK samples didn't show any peaks related to ECM environment as indicated in fig. 5-1(c). The absence of collagen and/or minerals formation on the PEEK surfaces could be attributed to the low surface energy, hydrophobic nature, and surface smoothness, that lead to low protein adsorption, less cell attachment, and result in less to no collagen or minerals formations.

After 60 days of the in vitro cell culture, the FT-IR spectra revealed the presence of ECM deposition on the surface of each samples (Si_3N_4, Ti, and PEEK), as indicated in fig. 5-1(d, e, f). FT-IR spectra of PEEK samples confirmed the presence of organic and inorganic components of the ECM environment. It should be noted that amides and PO_4^{3-} peaks intensity increased after 60 days compared to 30 days on Si_3N_4 and Ti surfaces. Also, two closed peaks were observed for amide I at 1659 and 1628 cm^{-1}, this shift in amide I peak position could be attributed to the presence of collagen/Ca^{2+} structure [171].

5.2 ECM analysis by Scanning Electron Microscopy

As mentioned before, collagen is the main component of the ECM and the most abundant protein in our bodies. It is a strong fibrous protein that forms stretch-resistant fibers. In the ECM, collagen bundles consist from single collagen fibrils (20 nm in diameter) that be composed of small fine fabrics. Scanning electron microscopy can provide insight into the ECM environment and the collagen fibers by examination the tissue morphology.

In the current study, we used the HR-SEM to capture the samples surfaces and investigate the formation of collagen fibers. Fig. 5-2 indicates the surface morphology of the samples after 30 days of the in vitro study. From fig. 5-2 (a), it should be noted that Si_3N_4 surface is completely covered with the collagen fibrils that turned into collagen bundles as indicated by the arrows. Furthermore, minerals formations of amorphous calcium phosphate ACP deposition are found on the surface as indicated by the high magnification image. SEM images also confirmed the presence of collagen fibers and minerals deposition on the surface of Ti samples (Fig. 5-2b). Although the high magnification images indicated that collagen fibers started to form collagen bundles on Ti surface, the Ti surface in not completely covered by the collagen fibers. Also, sparse deposition of ACP was detected on the surface of Ti samples. On the other hand, SEM imaged of the PEEK samples revealed the presence of collagen fibrils, but no collagen bundles were detected. Moreover, the PEEK surface was not completely covered by the collagen fibers. The poor ECM formations on the PEEK surfaces could be attributed to the low number of attached cells that result in low differentiation and poor ECM deposition. By comparing the three different surfaces of Si_3N_4, Ti, and PEEK after 30 days of the in vitro study, it is noted that the ECM deposition was formed in highest density

on the bioactive silicon nitride samples. Also, Si_3N_4 was completely covered with collagen bundles and ACP particles, but Ti and PEEK surfaces showed low surface coverage area of ECM, sparse deposition of ACP, and the bare surfaces can be easily seen.

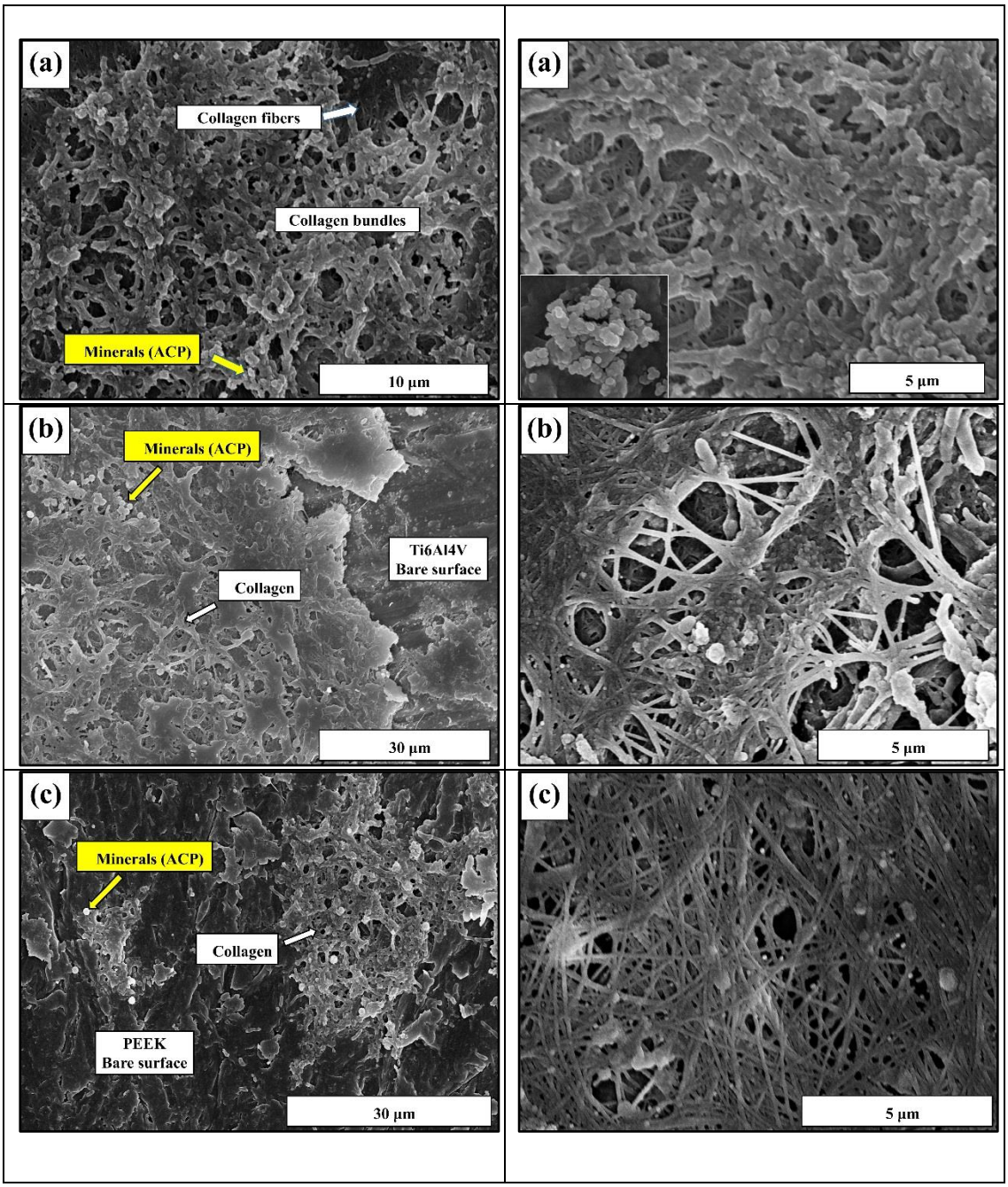

Figure 5-2: SEM images of different magnification for (a) Si_3N_4, (b) Ti6Al4V, and (c) PEEK samples showing the matrix deposition after 30 days of in vitro study.

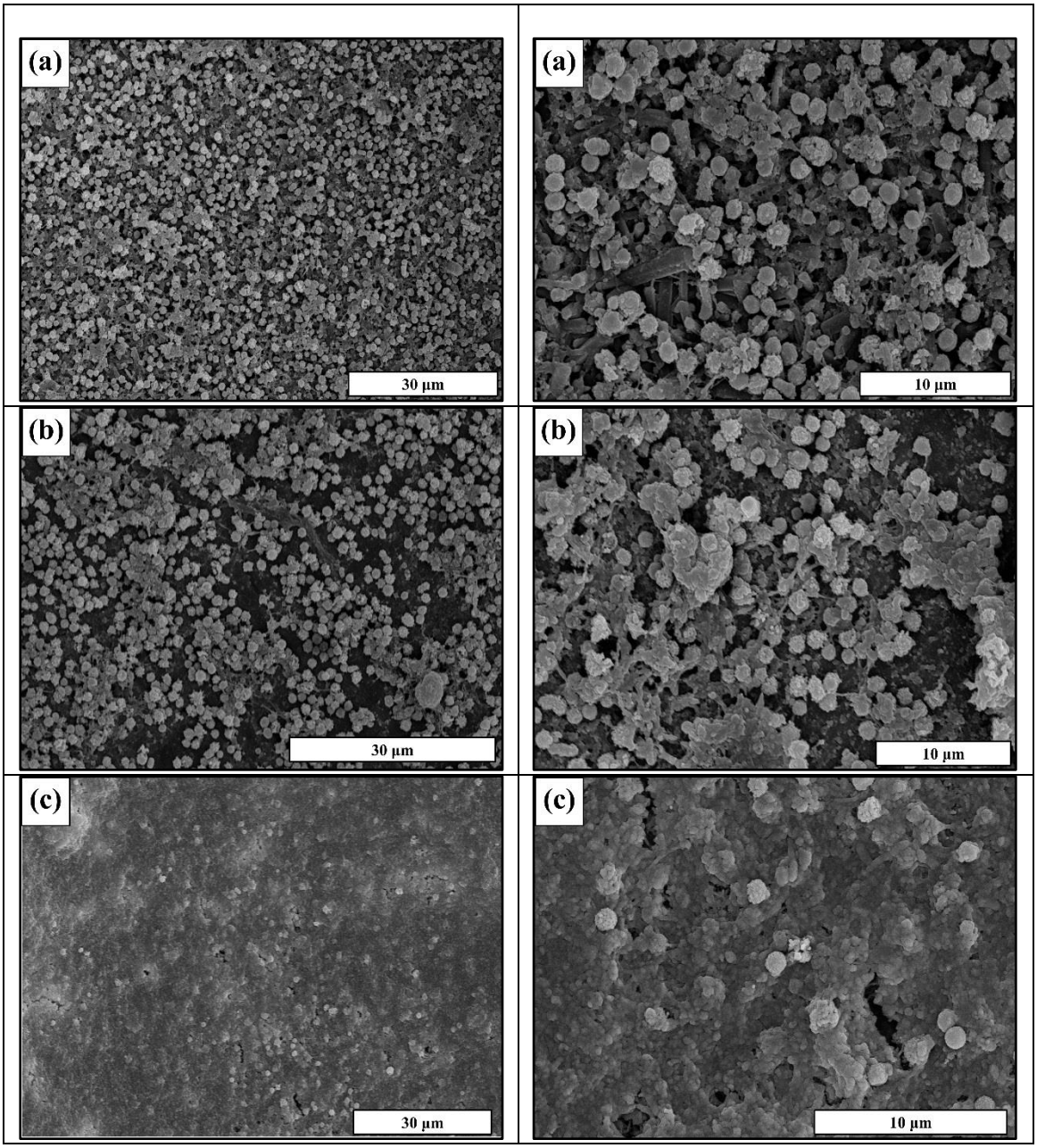

Figure 5-3: SEM images of different magnification for (a) Si_3N_4, (b) Ti6Al4V, and (c) PEEK samples showing the matrix deposition after 60 days of in vitro study.

Fig. 5-3 presents the SEM images at different magnification of (a) Si_3N_4, (b) Ti6Al4V, and (c) PEEK samples investigating the matrix deposition after 60 days of in vitro study. After 60, surfaces of Si_3N_4 and Ti samples become completely covered with “flower-like” porous structure of ACP deposition. Although the Ti surfaces showed a comparable area coverage of deposited minerals to the Si_3N_4, the later still has the highest coverage area as indicated in fig. 5-3a. For PEEK

samples after 60 days, the surface became covered with collagen bundles and sparse of ACP deposition.

Our SEM findings support our previous conclusions from the surface properties, in vitro free cell studies, and the osteoprogenitor cell study. We mentioned before that there are delays in osteoprogenitor growth on Ti and PEEK surfaces as compared to Si_3N_4, and the SEM data confirmed this by indicating the high density and surface coverage of ECM on the Si_3N_4 surfaces. Low surface energy, a lack of surface functional groups that act as precursors for collagenous ECM formation are the main reasons for poor ECM deposition on Ti and PEEK. Contrariwise, hydrophilic nature, high surface energy, presence of Si-O and Si-N bonding on the surface of Si_3N_4 lead high number of cell attachment, cell growth and proliferation, and promote collagenous biomineral deposition.

5.3 Energy Dispersive X-Ray Analysis:

The energy dispersive X-ray (EDS) detector was used to determine the surface morphology, composition, and element distribution of the deposited matrix. Also, surface mapping by EDS for the ECM deposition will be presented. Regions of interest corresponding to ACP deposition were defined by mapping the surfaces and detect the Ca, and P K edges. After 30 days of the in vitro study, we could only identify that the Ca and P deposition on the surface of Si_3N_4 samples only as shown in fig. 5.4. This could be attributed to the high density of ACP deposition on the surface of Si_3N_4 compared to Ti and PEEK samples that did not show any Ca or P deposition by EDS analysis. Fig. 5-5 present the EDS mapping of the samples after 60 days. After 60 days, EDS mapping clearly identified the presence of ACP deposition on the surface of all samples, but high density of Ca and P deposition have indicated on Si_3N_4 surfaces (fig. 5-5a) as expected.

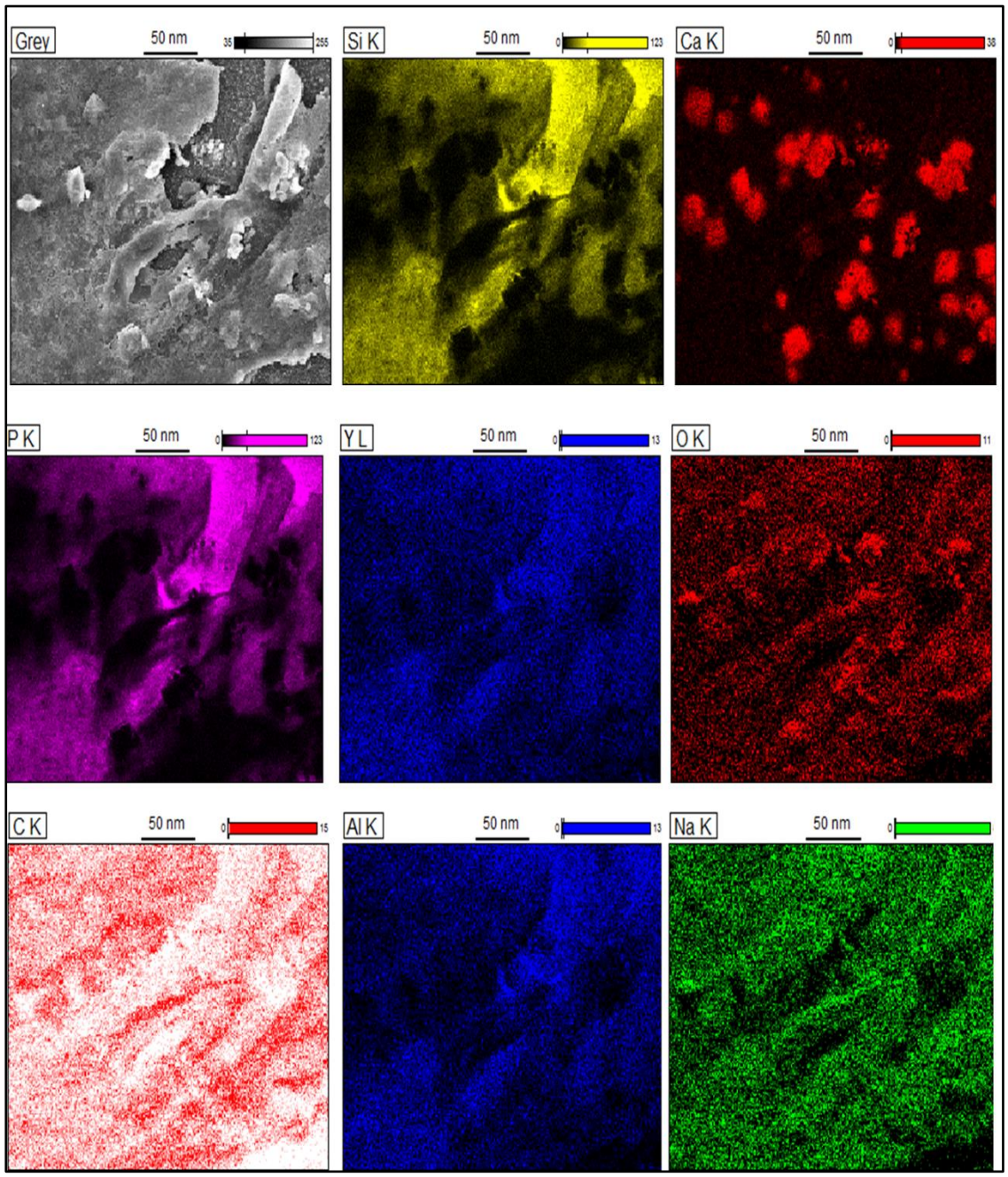

Figure 5-4: EDS mapping of Si_3N_4 sample showing the matrix deposition after 30 days of in vitro study.

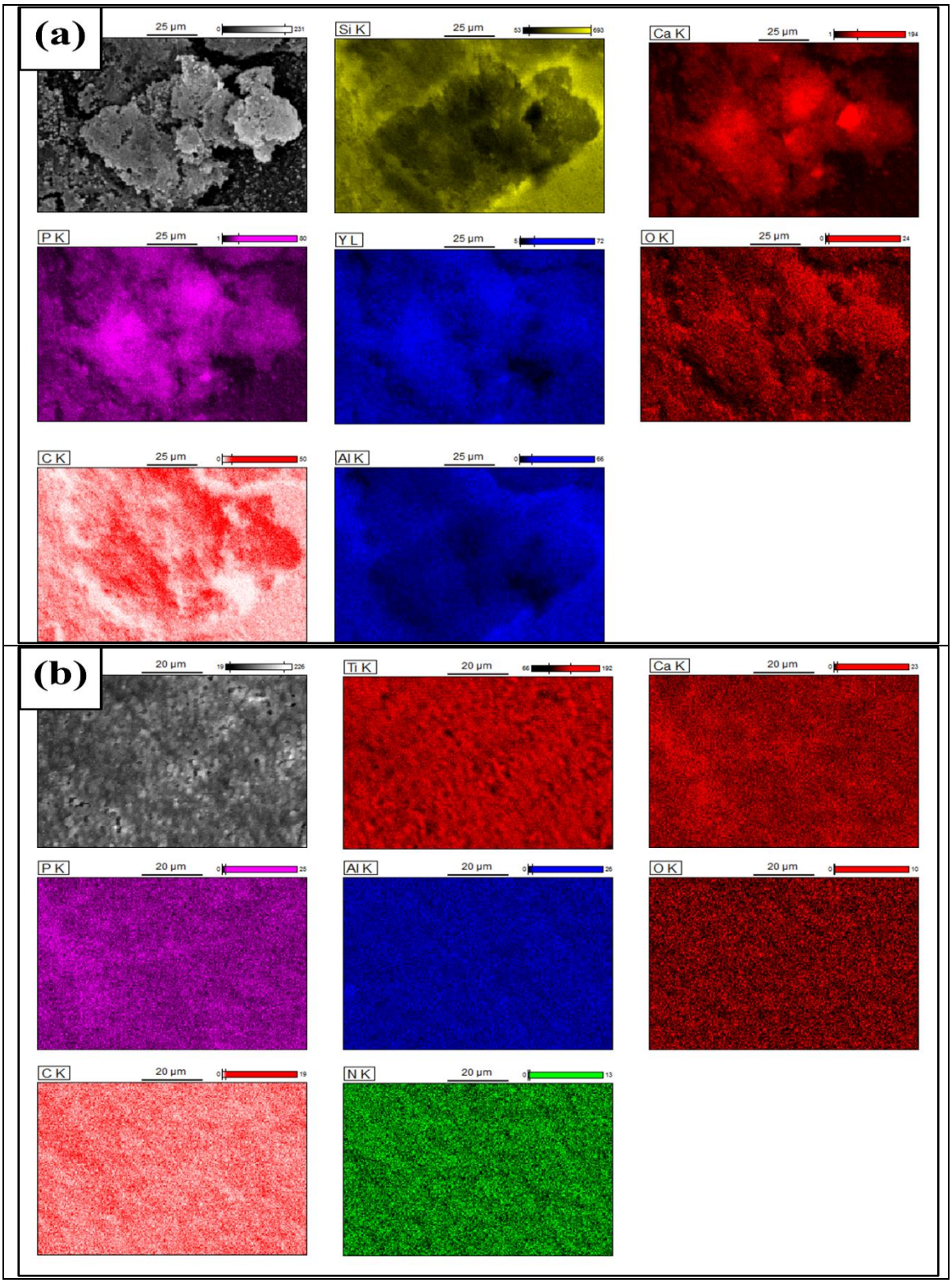

Figure 5-5: EDS mapping of (a) Si_3N_4, (b) Ti, and (c) PEEK sample showing the matrix deposition after 60 days of in vitro study.

/

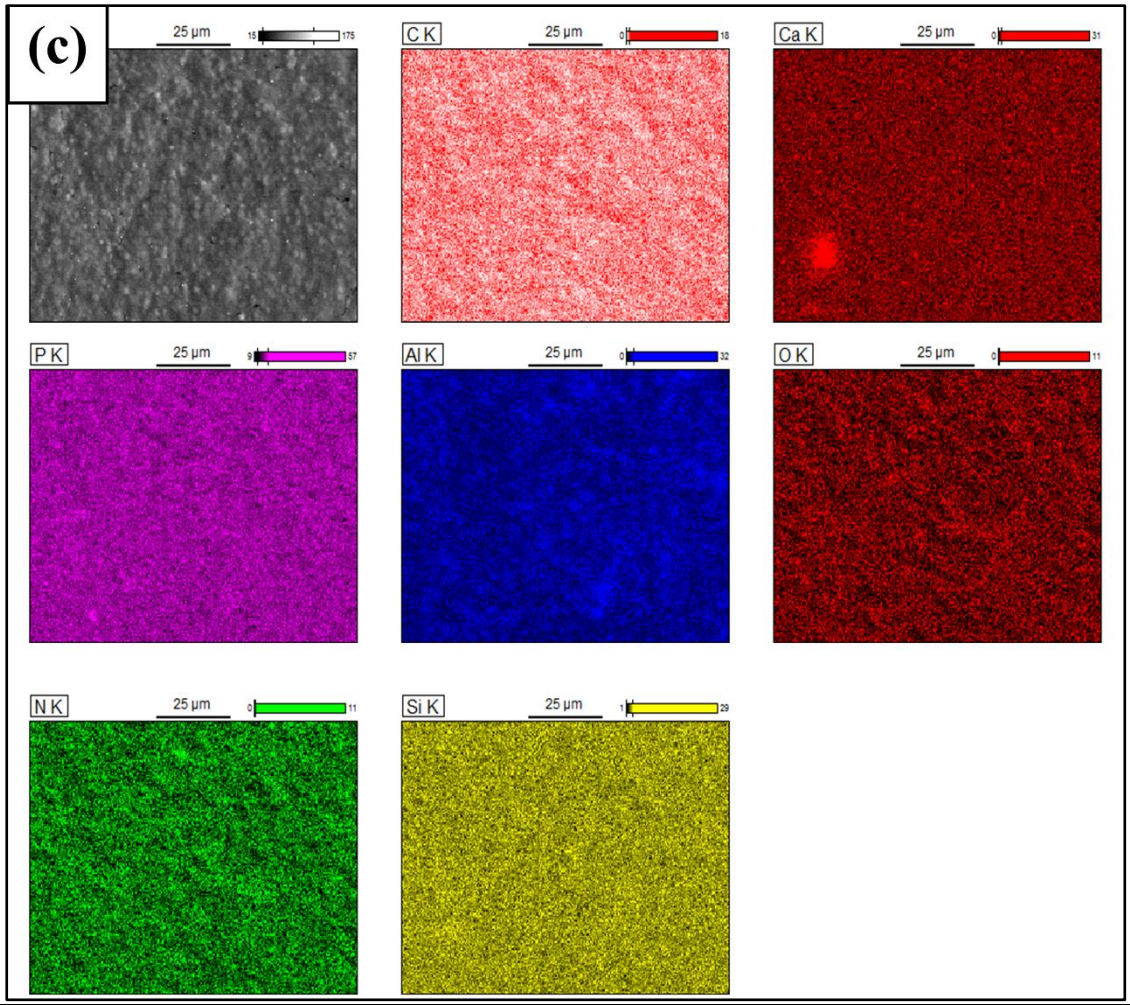

Figure 5-5: EDS mapping of (a) Si_3N_4, (b) Ti, and (c) PEEK sample showing the matrix deposition after 60 days of in vitro study (Cont.).

Conclusions

In this present study, surface properties of three different fixative bone implant materials were investigated. Silicon nitride, titanium, and polyetheretherketone were compared. Our aim was to correlate the osteoprogenitor cell adhesion and growth to surface roughness, surface energy, and surface functional group formation to identify differences in the osteogenic potential of Si_3N_4, Ti, and PEEK implant materials. We found that osteoprogenitor cells have a well-adherent profile, relatively high in density, and faster growth rate on the bioactive silicon nitride surfaces as compared to titanium and PEEK. Silicon nitride's surface energy and surface functional group formation are the main contributors to this result. Lower contact angles (*i.e.*, higher surface energy) and hydrophilic nature of silicon nitride's surface facilitated increased potential for cell migration and growth. High surface energy and improved wettability of Si_3N_4 result in rapid formation of nanocrystalline HA along with amide functional group precursors important for collagen formation. Furthermore, comprehensive ECM deposition study by FT-IR and SEM/EDS confirmed high density and complete surface coverage of ECM on the Si_3N_4 surfaces compared to Ti and PEEK samples. Concisely, hydrophilic nature, high surface energy, presence of Si-O and Si-N bonding, rapid formation of nanocrystalline HA along with amide functional group precursors on the surface of Si_3N_4 lead to high number of cell attachment, cell growth and proliferation, and promote high density of collagenous biomineral deposition.

References

[1] Allied Market Research, Bone Grafts and Substitutes Market by Product (Allografts, Bone Grafts Substitutes, and Cell-based Matrices), by Application (Spinal Fusion, Long Bone, Foot & Ankle, Craniomaxillofacial, Joint Reconstruction, and Dental Bone Grafting) - Global Opportunity, (2016) 130. https://www.alliedmarketresearch.com/bone-graft-substitutes-market.

[2] Allied Market Research, Craniomaxillofacial Implants Market by Product (Mid Face Implants, Cranial or Neuro Implants, Man-dibular Orthognathic Implants, Distraction Systems, Bone Graft Substitutes, Thoracic Fixation Systems, Total TMJ Replacement Systems, Dural Repair Product, (2018).

[3] R.F. Fernández, C. Bucchi, P. Navarro, V. Beltrán, E. Borie, Bone grafts utilized in dentistry: an analysis of patients' preferences, BMC Medical Ethics. 16 (2015) 1–6. doi:10.1186/s12910-015-0044-6.

[4] R.H. Khonsari, P. Berthier, T. Rouillon, J.P. Perrin, P. Corre, Severe infectious complications after PEEK-derived implant placement: Report of three cases, Journal of Oral and Maxillofacial Surgery, Medicine, and Pathology. 26 (2014) 477–482. doi:10.1016/j.ajoms.2013.04.006.

[5] S.M. Kurtz, J.N. Devine, PEEK biomaterials in trauma, orthopedic, and spinal implants, Biomaterials. 28 (2007) 4845–4869. doi:10.1016/j.biomaterials.2007.07.013.

[6] R. Olivares-Navarrete, R.A. Gittens, J.M. Schneider, S.L. Hyzy, D.A. Haithcock, P.F. Ullrich, Z. Schwartz, B.D. Boyan, Osteoblasts exhibit a more differentiated phenotype and increased bone morphogenetic protein production on titanium alloy substrates than on poly-ether-ether-ketone, Spine Journal. 12 (2012) 265–272. doi:10.1016/j.spinee.2012.02.002.

[7] M.H. Pelletier, N. Cordaro, V.M. Punjabi, M. Waites, A. Lau, W.R. Walsh, PEEK versus ti interbody fusion devices resultant fusion, bone apposition, initial and 26-week biomechanics, Clinical Spine Surgery. 29 (2016) E208–E214. doi:10.1097/BSD.0b013e31826851a4.

[8] K. Anselme, Osteoblast adhesion on biomaterials, Biomaterials. 21 (2000) 667–681. doi:10.1016/S0142-9612(99)00242-2.

[9] D.R. Lu, S.J. Lee, K. Park, Calculation of solvation interaction energies for protein adsorption on polymer surfaces, Journal of Biomaterials Science, Polymer Edition. 3 (1992) 127–147. doi:10.1163/156856291X00232.

[10] T.J. Webster, A.A. Patel, M.N. Rahaman, B. Sonny Bal, Anti-infective and osteointegration properties of silicon nitride, poly(ether ether ketone), and titanium implants, Acta Biomaterialia. 8 (2012) 4447–4454. doi:10.1016/j.actbio.2012.07.038.

[11] B. Dabrowski, W. Swieszkowski, D. Godlinski, K.J. Kurzydlowski, Highly porous titanium scaffolds for orthopaedic applications, Journal of Biomedical Materials Research - Part B Applied Biomaterials. 95 (2010) 53–61. doi:10.1002/jbm.b.31682.

[12] A. Jokstad, Common complications with implants and implant prostheses: What complications are associated with dental implants?, Evidence-Based Dentistry. 5 (2004) 70–71. doi:10.1038/sj.ebd.6400267.

[13] S. J., A. Gordon, J. Mark, Risk Factors for Aseptic Loosening Following Total Hip Arthroplasty, Recent Advances in Arthroplasty. (2012). doi:10.5772/26975.

[14] J.N. Katz, J. Wright, E.A. Wright, E. Losina, Failures of Total Hip Replacement: A Population-Based Perspective, Orthopaedic Journal of Harvard Medical School. 9 (2009) 101–106. http://www.orthojournalhms.org/volume9/manuscripts/ms11.pdf.

[15] M. Iwai-Yoshida, Y. Shibata, Wurihan, D. Suzuki, N. Fujisawa, Y. Tanimoto, R. Kamijo, K. Maki, T. Miyazaki, Antioxidant and osteogenic properties of anodically oxidized titanium, Journal of the Mechanical Behavior of Biomedical Materials. 13 (2012) 230–236. doi:10.1016/j.jmbbm.2012.01.016.

[16] B.S. Bal, M.N. Rahaman, Orthopedic applications of silicon nitride ceramics, Acta Biomaterialia. 8 (2012) 2889–2898. doi:10.1016/j.actbio.2012.04.031.

[17] G. Pezzotti, R.M. Bock, T. Adachi, A. Rondinella, F. Boschetto, W. Zhu, E. Marin, B. McEntire, B.S. Bal, O. Mazda, Silicon nitride surface chemistry: A potent regulator of mesenchymal progenitor cell activity in bone formation, Applied Materials Today. 9

(2017) 82–95. doi:10.1016/j.apmt.2017.05.005.

[18] G. Pezzotti, B.J. McEntire, R. Bock, W. Zhu, F. Boschetto, A. Rondinella, E. Marin, Y. Marunaka, T. Adachi, T. Yamamoto, N. Kanamura, B.S. Bal, In Situ Spectroscopic Screening of Osteosarcoma Living Cells on Stoichiometry-Modulated Silicon Nitride Bioceramic Surfaces, ACS Biomaterials Science and Engineering. 2 (2016) 1121–1134. doi:10.1021/acsbiomaterials.6b00126.

[19] G. Pezzotti, B.J. McEntire, R. Bock, M. Boffelli, W. Zhu, E. Vitale, L. Puppulin, T. Adachi, T. Yamamoto, N. Kanamura, B.S. Bal, Silicon Nitride: A Synthetic Mineral for Vertebrate Biology, Scientific Reports. 6 (2016) 2–8. doi:10.1038/srep31717.

[20] M. Mazzocchi, A. Bellosi, On the possibility of silicon nitride as a ceramic for structural orthopaedic implants. Part I: Processing, microstructure, mechanical properties, cytotoxicity, Journal of Materials Science: Materials in Medicine. 19 (2008) 2881–2887. doi:10.1007/s10856-008-3417-2.

[21] K.-P. Jen, R. Warzoha, J. Guo, M. Tang, S. Santhanam, Processing and Characterization of Silicon Nitride Bioceramics, Journal of Nanomaterials. 2013 (2013) 1–7. doi:10.1155/2013/875361.

[22] M. Ishikawa, K.L. de Mesy Bentley, B.J. McEntire, B.S. Bal, E.M. Schwarz, C. Xie, Surface topography of silicon nitride affects antimicrobial and osseointegrative properties of tibial implants in a murine model, Journal of Biomedical Materials Research - Part A. 105 (2017) 3413–3421. doi:10.1002/jbm.a.36189.

[23] R.M. Bock, E.N. Jones, D.A. Ray, B. Sonny Bal, G. Pezzotti, B.J. McEntire, Bacteriostatic behavior of surface modulated silicon nitride in comparison to polyetheretherketone and titanium, Journal of Biomedical Materials Research - Part A. 105 (2017) 1521–1534. doi:10.1002/jbm.a.35987.

[24] G. Pezzotti, N. Oba, W. Zhu, E. Marin, A. Rondinella, F. Boschetto, B. McEntire, K. Yamamoto, B.S. Bal, Human osteoblasts grow transitional Si/N apatite in quickly osteointegrated Si3N4cervical insert, Acta Biomaterialia. 64 (2017) 411–420. doi:10.1016/j.actbio.2017.09.038.

[25] G. Pezzotti, R.M. Bock, B.J. McEntire, E. Jones, M. Boffelli, W. Zhu, G. Baggio, F. Boschetto, L. Puppulin, T. Adachi, T. Yamamoto, N. Kanamura, Y. Marunaka, B.S. Bal, Silicon Nitride Bioceramics Induce Chemically Driven Lysis in Porphyromonas gingivalis, Langmuir. 32 (2016) 3024–3035. doi:10.1021/acs.langmuir.6b00393.

[26] R.M. Bock, B.J. McEntire, B.S. Bal, M.N. Rahaman, M. Boffelli, G. Pezzotti, Surface modulation of silicon nitride ceramics for orthopaedic applications, Acta Biomaterialia. 26 (2015) 318–330. doi:10.1016/j.actbio.2015.08.014.

[27] Allied Market Research, Orthopedic Implants Market by Product [Reconstructive Joint Replacements {Knee Replacement Implants, Hip Replacement Implants, and Extremities}, Spinal Implants {Spinal Fusion Devices, Non-Fusion Devices/Motion Preservation Devices, and Invasive Spinal Bo, (2017) 210. www.alliedmarketresearch.com/orthopedic-implants-market.

[28] Y. (JP Shohei Kuroda, Yokohama (JP); Takuya Yamamoto, Yokohama (JP); Yuko Saeki, Yokohama (JP); Masumi Kurasawa, UnIted States Patent, 2 (2013). doi:10.1126/science.Liquids.

[29] H. Eufinger, M. Wehmöller, E. Machtens, L. Heuser, A. Harders, D. Kruse, Reconstruction of craniofacial bone defects with individual alloplastic implants based on CAD/CAM-manipulated CT-data, Journal of Cranio-Maxillofacial Surgery. 23 (1995) 175–181. doi:10.1016/S1010-5182(05)80007-1.

[30] J.J. Kuttenberger, N. Hardt, Long-term results following reconstruction of craniofacial defects with titanium micro-mesh systems, Journal of Cranio-Maxillofacial Surgery. 29 (2001) 75–81. doi:10.1054/jcms.2001.0197.

[31] A. Menderes, C. Baytekin, A. Topcu, M. Yilmaz, A. Barutcu, Craniofacial reconstruction with high-density porous polyethylene implants., The Journal of Craniofacial Surgery. 15 (2004) 719–724. doi:10.1097/00001665-200409000-00004.

[32] J. Kwarcinski, P. Boughton, A. Ruys, A. Doolan, J. van Gelder, Cranioplasty and Craniofacial Reconstruction: A Review of Implant Material, Manufacturing Method and Infection Risk, Applied Sciences. 7 (2017) 276. doi:10.3390/app7030276.

[33] J. Parthasarathy, 3D modeling, custom implants and its future perspectives in craniofacial surgery, Annals of Maxillofacial Surgery. 4 (2014) 9. doi:10.4103/2231-0746.133065.

[34] U. Klammert, U. Gbureck, E. Vorndran, J. Rödiger, P. Meyer-Marcotty, A.C. Kübler, 3D powder printed calcium phosphate implants for reconstruction of cranial and maxillofacial defects, Journal of Cranio-Maxillofacial Surgery. 38 (2010) 565–570. doi:10.1016/j.jcms.2010.01.009.

[35] D.F. Williams, On the mechanisms of biocompatibility, Biomaterials. 29 (2008) 2941–2953. doi:10.1016/j.biomaterials.2008.04.023.

[36] G. Thrivikraman, A. Athirasala, C. Twohig, S.K. Boda, L.E. Bertassoni, Biomaterials for Craniofacial Bone Regeneration, Dental Clinics of North America. 61 (2017) 835–856. doi:10.1016/j.cden.2017.06.003.

[37] T. Albrektsson, C. Johansson, Osteoinduction, osteoconduction and osseointegration, European Spine Journal. 10 (2001) S96–S101. doi:10.1007/s005860100282.

[38] O.E.M. Pohler, Unalloyed titanium for implants in bone surgery, Injury. 31 (2000). doi:10.1016/S0020-1383(00)80016-9.

[39] M. Abdel-Hady Gepreel, M. Niinomi, Biocompatibility of Ti-alloys for long-term implantation, Journal of the Mechanical Behavior of Biomedical Materials. 20 (2013) 407–415. doi:10.1016/j.jmbbm.2012.11.014.

[40] H.H. Huang, Electrochemical impedance spectroscopy study of strained titanium in fluoride media, Electrochimica Acta. 47 (2002) 2311–2318. doi:10.1016/S0013-4686(02)00079-8.

[41] I.H. Oh, N. Nomura, N. Masahashi, S. Hanada, Mechanical properties of porous titanium compacts prepared by powder sintering, Scripta Materialia. 49 (2003) 1197–1202. doi:10.1016/j.scriptamat.2003.08.018.

[42] M. Takemoto, S. Fujibayashi, M. Neo, J. Suzuki, T. Kokubo, T. Nakamura, Mechanical properties and osteoconductivity of porous bioactive titanium, Biomaterials. 26 (2005) 6014–6023. doi:10.1016/j.biomaterials.2005.03.019.

[43] X. Liu, P.K. Chu, C. Ding, Surface modification of titanium, titanium alloys, and related materials for biomedical applications, Materials Science and Engineering R: Reports. 47 (2004) 49–121. doi:10.1016/j.mser.2004.11.001.

[44] H.W. Moyen BJ, Lahey PJ Jr, Weinberg EH, Effects on intact femora of dogs of the application and removal of metal plates. A metabolic and structural study comparing stiffer and more flexible plates., J Bone Joint Surg. 60A (1978) 940. https://www.ncbi.nlm.nih.gov/pubmed/100500.

[45] C.E. Wen, M. Mabuchi, Y. Yamada, K. Shimojima, Y. Chino, T. Asahina, Processing of biocompatible porous Ti and Mg, Scripta Materialia. 45 (2001) 1147–1153. doi:10.1016/S1359-6462(01)01132-0.

[46] D. Apostu, O. Lucaciu, C. Berce, D. Lucaciu, D. Cosma, Current methods of preventing aseptic loosening and improving osseointegration of titanium implants in cementless total hip arthroplasty: a review, Journal of International Medical Research. 0 (2017) 30006051773269. doi:10.1177/0300060517732697.

[47] D.P. Lombardi AV Jr 1 , Mallory TH , Vaughn BK, Aseptic loosening in total hip arthroplasty secondary to osteolysis induced by wear debris from titanium-alloy modular femoral heads, The Journal of Bone and Joint Surgery. 71 (1989) 1337–1342. https://insights.ovid.com/pubmed?pmid=2793886.

[48] R. Tsaryk, M. Kalbacova, U. Hempel, D. Scharnweber, R.E. Unger, P. Dieter, C.J. Kirkpatrick, K. Peters, Response of human endothelial cells to oxidative stress on Ti6Al4V alloy, Biomaterials. 28 (2007) 806–813. doi:10.1016/j.biomaterials.2006.09.033.

[49] H.K. Tsou, M.H. Chi, Y.W. Hung, C.J. Chung, J.L. He, In Vivo Osseointegration Performance of Titanium Dioxide Coating Modified Polyetheretherketone Using Arc Ion Plating for Spinal Implant Application, BioMed Research International. 2015 (2015). doi:10.1155/2015/328943.

[50] P.J. Rao, M.H. Pelletier, W.R. Walsh, R.J. Mobbs, Spine Interbody Implants: Material Selection and Modification, Functionalization and Bioactivation of Surfaces to Improve Osseointegration, Orthopaedic Surgery. 6 (2014) 81–89. doi:10.1111/os.12098.

[51] F.I. Riley, Silicon Nitride and Related Materials, Journal of American Ceramics Society. 83 (2000) 245–265. doi:10.1111/j.1151-2916.2000.tb01182.x.

[52] W. Wang, M. Hadfield, A.A. Wereszczak, Surface strength of silicon nitride in relation to rolling contact performance measured on ball-on-rod and modified four-ball tests, Tribology International. 43 (2010) 423–432. doi:10.1016/j.triboint.2009.07.005.

[53] A. Neumann, K. Jahnke, H.R. Maier, C. Ragoss, Biocompatibilty of silicon nitride ceramic in vitro. A comparative fluorescence-microscopic and scanning electron-microscopic study, Laryngo- Rhino- Otologie. 83 (2004) 845—851. doi:10.1055/s-2004-825739.

[54] R. Kue, A. Sohrabi, D. Nagle, C. Frondoza, D. Hungerford, Enhanced proliferation and osteocalcin production by human osteoblast-like MG63 cells on silicon nitride ceramic discs, Biomaterials. 20 (1999) 1195–1201. doi:10.1016/S0142-9612(99)00007-1.

[55] A. Neumann, T. Reske, M. Held, K. Jahnke, C. Ragoß, H.R. Maier, Comparative investigation of the biocompatibility of various silicon nitride ceramic qualities in vitro, Journal of Materials Science: Materials in Medicine. 15 (2004) 1135–1140. doi:10.1023/B:JMSM.0000046396.14073.92.

[56] A. Neumann, C. Unkel, C. Werry, C.U. Herborn, H.R. Maier, C. Ragoß, K. Jahnke, Prototype of a silicon nitride ceramic-based miniplate osteofixation system for the midface, Otolaryngology - Head and Neck Surgery. 134 (2006) 923–930. doi:10.1016/j.otohns.2006.01.022.

[57] J.E. Penner-Hahn, X-ray absorption spectroscopy, Comprehensive Coordination Chemistry II. (2004) 159–186. doi:10.1038/277089a0.

[58] S. Bare, XANES Measurements and Interpretation, EXAFS Data Collection and Analysis Course, APS. (2005) 1–51. http://cars9.uchicago.edu/xafs_school/Material/Lectures/XANES Bare.pdf.

[59] J. Lincks, B.D. Boyan, C.R. Blanchard, C.H. Lohmann, Y. Liu, D.L. Cochran, D.D. Dean, Z. Schwartz, Response of MG63 osteoblast-like cells to titanium and titanium alloy is dependent on surface roughness and composition, The Biomaterials: Silver Jubilee Compendium. 19 (2006) 147–160. doi:10.1016/B978-008045154-1.50019-8.

[60] A. Letic-Gavrilovic, R. Scandurra, A. Kimio, Review article The purpose of this review is to summarise recent advances in the design and composition of bioactive surface layers of implantabile and thus the genetic potential of osteoprogenitor cells to recognize and respond to these diverse implanted, Dental Materials Journal. 19 (2000) 99–132. doi:10.4012/dmj.19.99.

[61] L. Ponsonnet, V. Comte, A. Othmane, C. Lagneau, M. Charbonnier, M. Lissac, N. Jaffrezic, Effect of surface topography and chemistry on adhesion, orientation and growth of fibroblasts on nickel-titanium substrates, Materials Science and Engineering C. 21 (2002) 157–165. doi:10.1016/S0928-4931(02)00097-8.

[62] L. Ponsonnet, K. Reybier, N. Jaffrezic, V. Comte, C. Lagneau, M. Lissac, C. Martelet, Relationship between surface properties (roughness, wettability) of titanium and titanium alloys and cell behaviour, Materials Science and Engineering: C. 23 (2003) 551–560. doi:10.1016/S0928-4931(03)00033-X.

[63] J.V.; M. sendne. et All., Atomic Force Microscopy, Karls Universität Heidelberg Kirchhoff-Institut Für Physik. (2014). doi:10.1093/acprof:oso/9780199570454.001.0001.

[64] Y.F. Dufrêne, T. Ando, R. Garcia, D. Alsteens, D. Martinez-Martin, A. Engel, C. Gerber, D.J. Müller, Imaging modes of atomic force microscopy for application in molecular and cell biology, Nature Nanotechnology. 12 (2017) 295–307. doi:10.1038/nnano.2017.45.

[65] E.S. Gadelmawla, M.M. Koura, T.M.A. Maksoud, I.M. Elewa, H.H. Soliman, Roughness parameters, Journal of Materials Processing Technology. 123 (2002) 133–145. doi:10.1016/S0924-0136(02)00060-2.

[66] C.Y. Poon, B. Bhushan, Comparison of surface roughness measurements by stylus profiler, AFM and non-contact optical profiler, Wear. 190 (1995) 76–88. doi:10.1016/0043-1648(95)06697-7.

[67] S.A. Redey, S. Razzouk, C. Rey, D. Bernache-Assollant, G. Leroy, M. Nardin, G. Cournot, Osteoclast adhesion and activity on synthetic hydroxyapatite, carbonated hydroxyapatite, and natural calcium carbonate: Relationship to surface energies, Journal of Biomedical Materials Research. 45 (1999) 140–147. doi:10.1002/(SICI)1097-4636(199905)45:2<140::AID-JBM9>3.0.CO;2-I.

[68] K. Webb, V. Hlady, P.A. Tresco, Relative importance of surface wettability and charged functional groups on NIH 3T3 fibloblast attachment, spreading, and cytoskeletal organization, Journal of Biomedical Materials Research. 41 (1998) 422–430.

[69] C. Della Volpe, D. Maniglio, M. Brugnara, S. Siboni, M. Morra, The solid surface free energy calculation: I. In defense of the multicomponent approach, Journal of Colloid and Interface Science. 271 (2004) 434–453. doi:10.1016/j.jcis.2003.09.049.

[70] S. Siboni, C. Della Volpe, D. Maniglio, M. Brugnara, The solid surface free energy calculation: II. The limits of the Zisman and of the "equation-of-state" approaches, Journal of Colloid and Interface Science. 271 (2004) 454–472. doi:10.1016/j.jcis.2003.09.050.

[71] M. Amaral, M.A. Lopes, J.D. Santos, R.F. Silva, Wettability and surface charge of Si3N4-bioglass composites in contact with simulated physiological liquids, Biomaterials. 23 (2002) 4123–4129. doi:10.1016/S0142-9612(02)00155-2.

[72] J.J.M. Ramos, B.J. V Saramago, H. Background, Estimation of the Surface Tension of a Solid: Application to a Liquid Crystalline Polymer, Journal of Colloid and Interface Science. 369 (1997) 361–369.

[73] R. Hanke, T. Fuchs, M. Salamon, S. Zabler, X-ray microtomography for materials characterization, in: Materials Characterization Using Nondestructive Evaluation (NDE) Methods, 2016: pp. 45–79. doi:10.1016/B978-0-08-100040-3.00003-1.

[74] K.R. Awad, M.M.S. Wahsh, A.G.M. Othman, E. Girgis, M.R. Mabrouk, F.A. Morsy, Effect of Mn 2+ doping and SiO 2 coating on magneto-optical properties of CoFe 2 O 4 nano-particles, Smart Materials and Structures. 24 (2015) 115002. doi:10.1088/0964-1726/24/11/115002.

[75] A.W. Burton, K. Ong, T. Rea, I.Y. Chan, On the estimation of average crystallite size of zeolites from the Scherrer equation: A critical evaluation of its application to zeolites with one-dimensional pore systems, Microporous and Mesoporous Materials. 117 (2009) 75–90. doi:10.1016/j.micromeso.2008.06.010.

[76] R. Harrington, R.B. Neder, J.B. Parise, The nature of x-ray scattering from geo-

nanoparticles: Practical considerations of the use of the Debye equation and the pair distribution function for structure analysis, Chemical Geology. 329 (2012) 3–9. doi:10.1016/j.chemgeo.2011.06.010.

[77] sigmaaldrich, No Title, (n.d.). https://www.sigmaaldrich.com/life-science/cell-culture/learning-center/media-formulations/mem.html.

[78] T. Kokubo, H. Takadama, How useful is SBF in predicting in vivo bone bioactivity?, Biomaterials. 27 (2006) 2907–2915. doi:10.1016/j.biomaterials.2006.01.017.

[79] T. Kokubo, H. Kushitani, C. Ohtsuki, S. Sakka, T. Yamamuro, Chemical reaction of bioactive glass and glass-ceramics with a simulated body fluid, Journal of Materials Science: Materials in Medicine. 3 (1992) 79–83. doi:10.1007/BF00705272.

[80] T.L. Riss, R.A. Moravec, A.L. Niles, S. Duellman, H.A. Benink, T.J. Worzella, L. Minor, Cell Viability Assays, Assay Guidance Manual [Internet]. 114 (2013) 785–796. doi:10.1016/j.acthis.2012.01.006.

[81] A.I. Alford, K.M. Kozloff, K.D. Hankenson, Extracellular matrix networks in bone remodeling, International Journal of Biochemistry and Cell Biology. 65 (2015) 20–31. doi:10.1016/j.biocel.2015.05.008.

[82] J.K. Francis Suh, H.W.T. Matthew, Application of chitosan-based polysaccharide biomaterials in cartilage tissue engineering: A review, Biomaterials. 21 (2000) 2589–2598. doi:10.1016/S0142-9612(00)00126-5.

[83] B. Li, Y. Wang, D. Jia, Y. Zhou, Gradient Structural Bone-Like Apatite Induced by Chitosan Hydrogel via Ion Assembly, Journal of Biomaterials Science, Polymer Edition. 22 (2011) 505–517. doi:10.1163/092050610X487800.

[84] National Ambulatory Medical Care Survey 1998-2006. 2006 ed.; U.S. Department of Health and Human Services, C. f. D. C. a. P., Ed. National Center for Health Statistics, (2006).

[85] S. Gas, Biocompatibility of Bioresorbable Poly (L-lactic acid) Composite Scaffolds Obtained by, (2005).

[86] D. Dhanwal, E. Dennison, N. Harvey, C. Cooper, Epidemiology of hip fracture: Worldwide geographic variation, Indian Journal of Orthopaedics. 45 (2011) 15. doi:10.4103/0019-5413.73656.

[87] B. Zanotti, N. Zingaretti, A. Verlicchi, M. Robiony, A. Alfieri, P.C. Parodi, Cranioplasty, Journal of Craniofacial Surgery. 27 (2016) 2061–2072. doi:10.1097/SCS.0000000000003025.

[88] K.A. Hing, S.M. Best, K.E. Tanner, W. Bonfield, P.A. Revell, Mediation of bone ingrowth in porous hydroxyapatite bone graft substitutes, Journal of Biomedical Materials Research. 68A (2004) 187–200. doi:10.1002/jbm.a.10050.

[89] K.-Y. Lee, M. Park, H.-M. Kim, Y.-J. Lim, H.-J. Chun, H. Kim, S.-H. Moon, Ceramic bioactivity: progresses, challenges and perspectives, Biomedical Materials. 1 (2006) R31–R37. doi:10.1088/1748-6041/1/2/R01.

[90] S. Dorozhkin, Calcium Orthophosphate-Containing Biocomposites and Hybrid Biomaterials for Biomedical Applications, Journal of Functional Biomaterials. 6 (2015) 708–832. doi:10.3390/jfb6030708.

[91] S. Bodhak, S. Bose, A. Bandyopadhyay, Role of surface charge and wettability on early stage mineralization and bone cell–materials interactions of polarized hydroxyapatite, Acta Biomaterialia. 5 (2009) 2178–2188. doi:10.1016/j.actbio.2009.02.023.

[92] S. Itoh, M. Kikuchi, K. Takakuda, K. Nagaoka, Y. Koyama, J. Tanaka, K. Shinomiya, Implantation study of a novel hydroxyapatite/collagen (HAp/col) composite into weight-bearing sites of dogs, Journal of Biomedical Materials Research. 63 (2002) 507–515. doi:10.1002/jbm.10305.

[93] S.P. Reddi, M.R. Stevens, S.N. Kline, P. Villanueva, Hydroxyapatite cement in craniofacial trauma surgery: indications and early experience., The Journal of Cranio-Maxillofacial Trauma. 5 (1999) 7–12. http://www.ncbi.nlm.nih.gov/pubmed/11951225.

[94] E. Neovius, T. Engstrand, Craniofacial reconstruction with bone and biomaterials: Review over the last 11 years, Journal of Plastic, Reconstructive & Aesthetic Surgery. 63 (2010) 1615–1623. doi:10.1016/j.bjps.2009.06.003.

[95] B. Laure, J.-M. Besnier, A.-M. Bergemer-Fouquet, N. Marquet-Van Der Mee, F. Damie, R. Quentin, L. Favard, P. Rosset, Effect of hydroxyapatite coating and polymethylmethacrylate on stainless steel implant-site infection withStaphylococcus epidermidis in a sheep model, Journal of Biomedical Materials Research Part A. 84A (2008) 92–98. doi:10.1002/jbm.a.31376.

[96] D.J. Verret, Y. Ducic, L. Oxford, J. Smith, Hydroxyapatite Cement in Craniofacial Reconstruction, Otolaryngology-Head and Neck Surgery. 133 (2005) 897–899. doi:10.1016/j.otohns.2005.09.001.

[97] D.J. Ainbinder, B.G. Haik, M. Tellado, Hydroxyapatite orbital implant abscess: histopathologic correlation of an infected implant following evisceration., Ophthalmic Plastic and Reconstructive Surgery. 10 (1994) 267–70. http://www.ncbi.nlm.nih.gov/pubmed/7865449.

[98] D. Matic, J.H. Phillips, A contraindication for the use of hydroxyapatite cement in the pediatric population., Plastic and Reconstructive Surgery. 110 (2002) 1–5. http://www.ncbi.nlm.nih.gov/pubmed/12087221.

[99] S. Lazarinis, K.T. Mäkelä, A. Eskelinen, L. Havelin, G. Hallan, S. Overgaard, A.B. Pedersen, J. Kärrholm, N.P. Hailer, Does hydroxyapatite coating of uncemented cups improve long-term survival? An analysis of 28,605 primary total hip arthroplasty procedures from the Nordic Arthroplasty Register Association (NARA), Osteoarthritis and Cartilage. 25 (2017) 1980–1987. doi:10.1016/j.joca.2017.08.001.

[100] C. Turk, M. Halici, A. Guney, H. Akgun, V. Sahin, S. Muhtaroglu, Promotion of Fracture Healing by Vitamin E in Rats, Journal of International Medical Research. 32 (2004) 507–512. doi:10.1177/147323000403200508.

[101] E.L. Steinberg, E. Rath, A. Shlaifer, O. Chechik, E. Maman, M. Salai, Carbon fiber reinforced PEEK Optima-A composite material biomechanical properties and wear/debris characteristics of CF-PEEK composites for orthopedic trauma implants, Journal of the Mechanical Behavior of Biomedical Materials. 17 (2012) 221–228. doi:10.1016/j.jmbbm.2012.09.013.

[102] J.M. Toth, M. Wang, B.T. Estes, J.L. Scifert, H.B. Seim, A.S. Turner, Polyetheretherketone

as a biomaterial for spinal applications, Biomaterials. 27 (2006) 324–334. doi:10.1016/j.biomaterials.2005.07.011.

[103] S.W. Ha, M. Kirch, F. Birchler, K.L. Eckert, J. Mayer, E. Wintermantel, C. Sittig, I. Pfund-Klingenfuss, M. Textor, N.D. Spencer, M. Guecheva, H. Vonmont, Surface activation of polyetheretherketone (PEEK) and formation of calcium phosphate coatings by precipitation, Journal of Materials Science: Materials in Medicine. 8 (1997) 683–690. doi:10.1023/A:1018535923173.

[104] L. Petrovic, D. Pohle, H. Münstedt, T. Rechtenwald, K.A. Schlegel, S. Rupprecht, Effect of βTCP filled polyetheretherketone on osteoblast cell proliferation in vitro, Journal of Biomedical Science. 13 (2006) 41–46. doi:10.1007/s11373-005-9032-z.

[105] M.S. Abu Bakar, P. Cheang, K.A. Khor, Mechanical properties of injection molded hydroxyapatite-polyetheretherketone biocomposites, Composites Science and Technology. 63 (2003) 421–425. doi:10.1016/S0266-3538(02)00230-0.

[106] M.S. Abu Bakar, M.H.W. Cheng, S.M. Tang, S.C. Yu, K. Liao, C.T. Tan, K.A. Khor, P. Cheang, Tensile properties, tension–tension fatigue and biological response of polyetheretherketone–hydroxyapatite composites for load-bearing orthopedic implants, Biomaterials. 24 (2003) 2245–2250. doi:10.1016/S0142-9612(03)00028-0.

[107] F.B. Torstrick, D.L. Safranski, J.K. Burkus, J.L. Chappuis, C.S.D. Lee, R.E. Guldberg, K. Gall, K.E. Smith, Getting PEEK to Stick to Bone, Techniques in Orthopaedics. 32 (2017) 158–166. doi:10.1097/BTO.0000000000000242.

[108] A. Kulkarni Aranya, S. Pushalkar, M. Zhao, R.Z. LeGeros, Y. Zhang, D. Saxena, Antibacterial and bioactive coatings on titanium implant surfaces, Journal of Biomedical Materials Research Part A. 105 (2017) 2218–2227. doi:10.1002/jbm.a.36081.

[109] H.-B. Lee, H.-C. Hsu, S.-C. Wu, S.-K. Hsu, P.-H. Wang, W.-F. Ho, Microstructure and Characteristics of Calcium Phosphate Layers on Bioactive Oxide Surfaces of Air-Sintered Titanium Foams after Immersion in Simulated Body Fluid, Materials. 9 (2016) 956. doi:10.3390/ma9120956.

[110] B. Trybuś, A. Zieliński, R. Beutner, T. Seramak, D. Scharnweber, Deposition of phosphate

coatings on titanium within scaffold structure., Acta of Bioengineering and Biomechanics. 19 (2017) 65–72. http://www.ncbi.nlm.nih.gov/pubmed/28869630.

[111] J.D. Jones, M. Saigusa, J.E. Van Sickels, B.D. Tiner, W.A. Gardner, Clinical evaluation of hydroxyapatite-coated titanium plasma-sprayed and titanium plasma-sprayed cylinder dental implants: a preliminary report., Oral Surgery, Oral Medicine, Oral Pathology, Oral Radiology, and Endodontics. 84 (1997) 137–41. http://www.ncbi.nlm.nih.gov/pubmed/9269013.

[112] R.G. Geesink, N.H. Hoefnagels, Six-year results of hydroxyapatite-coated total hip replacement., The Journal of Bone and Joint Surgery. British Volume. 77 (1995) 534–47. http://www.ncbi.nlm.nih.gov/pubmed/7615595.

[113] O. Grassmann, R.B. Heimann, Compositional and microstructural changes of engineered plasma-sprayed hydroxyapatite coatings on Ti6Al4V substrates during incubation in protein-free simulated body fluid., Journal of Biomedical Materials Research. 53 (2000) 685–93. http://www.ncbi.nlm.nih.gov/pubmed/11074428.

[114] K. Teraoka, T. Nonami, Y. Doi, H. Taoda, K. Naganuma, Y. Yokogawa, T. Kameyama, Hydroxyapatite implantation on the surface of pure titanium for orthopedic implants, Materials Science and Engineering: C. 13 (2000) 105–107. doi:10.1016/S0928-4931(00)00183-1.

[115] S. Foppiano, S.J. Marshall, G.W. Marshall, E. Saiz, A.P. Tomsia, Bioactive glass coatings affect the behavior of osteoblast-like cells, Acta Biomaterialia. 3 (2007) 765–771. doi:10.1016/j.actbio.2007.02.011.

[116] K.A. Thomas, J.F. Kay, S.D. Cook, M. Jarcho, The effect of surface macrotexture and hydroxylapatite coating on the mechanical strengths and histologic profiles of titanium implant materials, Journal of Biomedical Materials Research. 21 (1987) 1395–1414. doi:10.1002/jbm.820211205.

[117] W.J.A. Dhert, C.P.A.T. Klein, J.G.C. Wolke, E.A. van der Velde, K. de Groot, P.M. Rozing, Student research award in the graduate degree candidate category, 17th annual meeting of the society for biomaterials, scottsdale, AZ may 1-5,1991. A mechanical investigation of fluorapatite, magnesiumwhitlockite, and hydroxylapatite plasma-sprayed coatin,

Journal of Biomedical Materials Research. 25 (1991) 1183–1200. doi:10.1002/jbm.820251002.

[118] B.C. Wang, T.M. Lee, E. Chang, C.Y. Yang, The shear strength and the failure mode of plasma-sprayed hydroxyapatite coating to bone: The effect of coating thickness, Journal of Biomedical Materials Research. 27 (1993) 1315–1327. doi:10.1002/jbm.820271012.

[119] C.P. Klein, P. Patka, H.B. van der Lubbe, J.G. Wolke, K. de Groot, Plasma-sprayed coatings of tetracalciumphosphate, hydroxyl-apatite, and alpha-TCP on titanium alloy: an interface study., Journal of Biomedical Materials Research. 25 (1991) 53–65. doi:10.1002/jbm.820250105.

[120] K. Hayashi, N. Matsuguchi, K. Uenoyama, T. Kanemaru, Y. Sugioka, Evaluation of metal implants coated with several types of ceramics as biomaterials, Journal of Biomedical Materials Research. 23 (1989) 1247–1259. doi:10.1002/jbm.820231103.

[121] K. Søballe, E.S. Hansen, H. Brockstedt-Rasmussen, C.M. Pedersen, C. Bünger, Hydroxyapatite coating enhances fixation of porous coated implants. A comparison in dogs between press fit and noninterference fit., Acta Orthopaedica Scandinavica. 61 (1990) 299–306. http://www.ncbi.nlm.nih.gov/pubmed/2402977.

[122] B.Y. Chou, E. Chang, Microstructural characterization of plasma-sprayed hydroxyapatite-10 wt% ZrO2 composite coating on titanium., Biomaterials. 20 (1999) 1823–32. http://www.ncbi.nlm.nih.gov/pubmed/10509193.

[123] Z. Zyman, J. Weng, X. Liu, X. Li, X. Zhang, Phase and structural changes in hydroxyapatite coatings under heat treatment, Biomaterials. 15 (1994) 151–155. doi:10.1016/0142-9612(94)90265-8.

[124] R. McPherson, N. Gane, T.J. Bastow, Structural characterization of plasma-sprayed hydroxylapatite coatings, Journal of Materials Science: Materials in Medicine. 6 (1995) 327–334. doi:10.1007/BF00120300.

[125] P. Frayssinet, F. Tourenne, I. Primout, C. Delga, E. Sergent, C. Besse, P. Conte, A. Guilhem, A study of structure and degradation of nonpolymeric biomaterials implanted in bone using reflected and transmitted light microscopy., Biotechnic & Histochemistry : Official

Publication of the Biological Stain Commission. 68 (1993) 333–41. http://www.ncbi.nlm.nih.gov/pubmed/8292657.

[126] M.J. Filiaggi, R.M. Pilliar, N.A. Coombs, Post-plasma-spraying heat treatment of the HA coating/Ti-6Al-4V implant system, Journal of Biomedical Materials Research. 27 (1993) 191–198. doi:10.1002/jbm.820270208.

[127] F. Lusquiños, J. del Val, F. Arias-González, R. Comesaña, F. Quintero, A. Riveiro, M. Boutinguiza, J.R. Jones, R.G. Hill, J. Pou, Bioceramic 3D Implants Produced by Laser Assisted Additive Manufacturing, Physics Procedia. 56 (2014) 309–316. doi:10.1016/j.phpro.2014.08.176.

[128] L.L. Hench, Bioceramics, Stress The International Journal on the Biology of Stress. 28 (1998) 1705–1728. doi:10.1111/j.1151-2916.1998.tb02540.x.

[129] A. Braem, T. Mattheys, B. Neirinck, M. Čeh, S. Novak, J. Schrooten, O. Van der Biest, J. Vleugels, Bioactive glass–ceramic coated titanium implants prepared by electrophoretic deposition, Materials Science and Engineering: C. 32 (2012) 2267–2273. doi:10.1016/j.msec.2012.06.013.

[130] D.. Bloyer, J.. Gomez-Vega, E. Saiz, J.. McNaney, R.. Cannon, A.. Tomsia, Fabrication and characterization of a bioactive glass coating on titanium implant alloys, Acta Materialia. 47 (1999) 4221–4224. doi:10.1016/S1359-6454(99)00280-3.

[131] B.A.J.A. van Oirschot, H.S. Alghamdi, T.O. Närhi, S. Anil, A. Al Farraj Aldosari, J.J.J.P. van den Beucken, J.A. Jansen, In vivo evaluation of bioactive glass-based coatings on dental implants in a dog implantation model, Clinical Oral Implants Research. 25 (2014) 21–28. doi:10.1111/clr.12060.

[132] J.M. Gomez-Vega, E. Saiz, A.P. Tomsia, G.W. Marshall, S.J. Marshall, Bioactive glass coatings with hydroxyapatite and Bioglass particles on Ti-based implants. 1. Processing., Biomaterials. 21 (2000) 105–11. http://www.ncbi.nlm.nih.gov/pubmed/10632392.

[133] J.M. Gomez-Vega, A. Hozumi, E. Saiz, A.P. Tomsia, H. Sugimura, O. Takai, Bioactive glass-mesoporous silica coatings on Ti6A14V through enameling and triblock-copolymer-templated sol-gel processing, Journal of Biomedical Materials Research. 56 (2001) 382–

389. doi:10.1002/1097-4636(20010905)56:3<382::AID-JBM1107>3.0.CO;2-P.

[134] T. Oku, K. Suganuma, L.R. Wallenberg, A.P. Tomsia, J.M. Gomez-Vega, E. Saiz, Structural characterization of the metal/glass interface in bioactive glass coatings on Ti-6Al-4V., Journal of Materials Science. Materials in Medicine. 12 (2001) 413–7. http://www.ncbi.nlm.nih.gov/pubmed/15348280.

[135] N. Saffarian Tousi, M.F. Velten, T.J. Bishop, K.K. Leong, N.S. Barkhordar, G.W. Marshall, P.M. Loomer, P.B. Aswath, V.G. Varanasi, Combinatorial effect of Si4 +, Ca2 +, and Mg2 +released from bioactive glasses on osteoblast osteocalcin expression and biomineralization, Materials Science and Engineering C. 33 (2013) 2757–2765. doi:10.1016/j.msec.2013.02.044.

[136] L. Zhao, P.K. Chu, Y. Zhang, Z. Wu, Antibacterial coatings on titanium implants, Journal of Biomedical Materials Research Part B: Applied Biomaterials. 91B (2009) 470–480. doi:10.1002/jbm.b.31463.

[137] W.-H. Song, H.S. Ryu, S.-H. Hong, Antibacterial properties of Ag (or Pt)-containing calcium phosphate coatings formed by micro-arc oxidation, Journal of Biomedical Materials Research Part A. 88A (2009) 246–254. doi:10.1002/jbm.a.31877.

[138] S.P. Valappil, D.M. Pickup, D.L. Carroll, C.K. Hope, J. Pratten, R.J. Newport, M.E. Smith, M. Wilson, J.C. Knowles, Effect of Silver Content on the Structure and Antibacterial Activity of Silver-Doped Phosphate-Based Glasses, Antimicrobial Agents and Chemotherapy. 51 (2007) 4453–4461. doi:10.1128/AAC.00605-07.

[139] P. Petrini, C.R. Arciola, I. Pezzali, S. Bozzini, L. Montanaro, M.C. Tanzi, P. Speziale, L. Visai, Antibacterial activity of zinc modified titanium oxide surface., The International Journal of Artificial Organs. 29 (2006) 434–42. http://www.ncbi.nlm.nih.gov/pubmed/16705613.

[140] A.H.K. Chou, R.Z. LeGeros, Z. Chen, Y. Li, Antibacterial effect of zinc phosphate mineralized guided bone regeneration membranes., Implant Dentistry. 16 (2007) 89–100. doi:10.1097/ID.0b013e318031224a.

[141] H.Y. Liu, X.J. Wang, L.P. Wang, F.Y. Lei, X.F. Wang, H.J. Ai, Effect of fluoride-ion implantation on the biocompatibility of titanium for dental applications, Applied Surface

Science. 254 (2008) 6305–6312. doi:10.1016/j.apsusc.2008.03.075.

[142] S. Bal, D. Gorth, S. Puckett, T.J. Webster, Rahaman, B. Ercan, Decreased bacteria activity on Si3N4 surfaces compared with PEEK or titanium, International Journal of Nanomedicine. (2012) 4829. doi:10.2147/IJN.S35190.

[143] R.M. Bock, E. Marin, A. Rondinella, F. Boschetto, T. Adachi, B.J. McEntire, B.S. Bal, G. Pezzotti, Development of a SiYAlON glaze for improved osteoconductivity of implantable medical devices., Journal of Biomedical Materials Research. Part B, Applied Biomaterials. 106 (2018) 1084–1096. doi:10.1002/jbm.b.33914.

[144] A. Ilyas, N. V. Lavrik, H.K.W. Kim, P.B. Aswath, V.G. Varanasi, Enhanced Interfacial Adhesion and Osteogenesis for Rapid "bone-like" Biomineralization by PECVD-Based Silicon Oxynitride Overlays, ACS Applied Materials and Interfaces. 7 (2015) 15368–15379. doi:10.1021/acsami.5b03319.

[145] X. Koningsberger, D. C.; Prins, R., absorption: principles, applications, techniques of EXAFS, SEXAFS, and XANES., John Wiley and Sons, New York, NY, 1988.

[146] A. Ilyas, T. Odatsu, A. Shah, F. Monte, H.K.W. Kim, P. Kramer, P.B. Aswath, V.G. Varanasi, Amorphous Silica: A New Antioxidant Role for Rapid Critical-Sized Bone Defect Healing, Advanced Healthcare Materials. 5 (2016) 2199–2213. doi:10.1002/adhm.201600203.

[147] V.G. Varanasi, A. Ilyas, M.F. Velten, A. Shah, W.A. Lanford, P.B. Aswath, Role of Hydrogen and Nitrogen on the Surface Chemical Structure of Bioactive Amorphous Silicon Oxynitride Films, The Journal of Physical Chemistry B. 121 (2017) 8991–9005. doi:10.1021/acs.jpcb.7b05885.

[148] G. Bunker, Interpreting XANES, Text. (2000).

[149] A.B.D. Cassie, Contact angles, Discussions of the Faraday Society. 3 (1948) 11. doi:10.1039/df9480300011.

[150] K.P. Sanosh, M.C. Chu, A. Balakrishnan, T.N. Kim, S.J. Cho, Utilization of biowaste eggshells to synthesize nanocrystalline hydroxyapatite powders, Materials Letters. 63 (2009) 2100–2102. doi:10.1016/j.matlet.2009.06.062.

[151] K.D. Son, D.J. Yang, M.S. Kim, I.-K. Kang, S.Y. Kim, Y.-J. Kim, Effect of alginate as polymer matrix on the characteristics of hydroxyapatite nanoparticles, Materials Chemistry and Physics. 132 (2012) 1041–1047. doi:10.1016/j.matchemphys.2011.12.062.

[152] X. Jia, Y. Zhou, L. Tan, Q. Xie, H. Tang, M. Ma, S. Yao, Hydroxyapitite-multiwalled carbon nanotubes nanocomposite for adhesion and electrochemical study of human osteoblast-like cells (MG-63), Electrochimica Acta. 54 (2009) 3611–3617. doi:10.1016/j.electacta.2009.01.031.

[153] C.C.G. e Silva, E.C. da S. Rigo, J. Marchi, A.H. de A. Bressiani, J.C. Bressiani, Hydroxyapatite coating on silicon nitride surfaces using the biomimetic method, Materials Research. 11 (2008) 47–50. doi:10.1590/S1516-14392008000100009.

[154] S. Wei, Y. Deng, X. Liu, A. Xu, L. Wang, Z. Luo, Y. Zheng, F. Deng, Z. Tang, J. Wei, Effect of surface roughness on osteogenesis in vitro and osseointegration in vivo of carbon fiber-reinforced polyetheretherketone–nanohydroxyapatite composite, International Journal of Nanomedicine. (2015) 1425. doi:10.2147/IJN.S75557.

[155] V.G. Varanasi, T.M. Besmann, R.L. Hyde, E.A. Payzant, T.J. Anderson, MOCVD of YSZ coatings using β-diketonate precursors, Journal of Alloys and Compounds. 470 (2009) 354–359. doi:10.1016/j.jallcom.2008.02.103.

[156] V.G. Varanasi, T.M. Besmann, E.A. Payzant, B.A. Pint, J.L. Lothian, T.J. Anderson, High-growth rate YSZ thermal barrier coatings deposited by MOCVD demonstrate high thermal cycling lifetime, Materials Science and Engineering: A. 528 (2011) 978–985. doi:10.1016/j.msea.2010.09.063.

[157] Y. Hu, Z. Gao, W. Sun, X. Liu, Anisotropic surface energies and adsorption behaviors of scheelite crystal, Colloids and Surfaces A: Physicochemical and Engineering Aspects. 415 (2012) 439–448. doi:10.1016/j.colsurfa.2012.09.038.

[158] Z.Y. Gao, W. Sun, Y.H. Hu, X.W. Liu, Anisotropic surface broken bond properties and wettability of calcite and fluorite crystals, Transactions of Nonferrous Metals Society of China (English Edition). 22 (2012) 1203–1208. doi:10.1016/S1003-6326(11)61306-X.

[159] Z.Y. Gao, W. Sun, Y.H. Hu, Mineral cleavage nature and surface energy: Anisotropic

surface broken bonds consideration, Transactions of Nonferrous Metals Society of China (English Edition). 24 (2014) 2930–2937. doi:10.1016/S1003-6326(14)63428-2.

[160] H. Turkez, M.I. Yousef, E. Sönmez, B. Togar, F. Bakan, P. Sozio, A. Di Stefano, Evaluation of cytotoxic, oxidative stress and genotoxic responses of hydroxyapatite nanoparticles on human blood cells, Journal of Applied Toxicology. 34 (2014) 373–379. doi:10.1002/jat.2958.

[161] S. Ramesh, C.Y. Tan, I. Sopyan, M. Hamdi, W.D. Teng, Consolidation of nanocrystalline hydroxyapatite powder, Science and Technology of Advanced Materials. 8 (2007) 124–130. doi:10.1016/j.stam.2006.11.002.

[162] Paul W. Brown, B. C., Hydroxyapatite and Related Materials., CRC Press: Technology & Engineering, 2017.

[163] K. Nitiputri, Q.M. Ramasse, H. Autefage, C.M. McGilvery, S. Boonrungsiman, N.D. Evans, M.M. Stevens, A.E. Porter, Nanoanalytical Electron Microscopy Reveals a Sequential Mineralization Process Involving Carbonate-Containing Amorphous Precursors, ACS Nano. 10 (2016) 6826–6835. doi:10.1021/acsnano.6b02443.

[164] T. Kokubo, Formation of biologically active bone-like apatite on metals and polymers by a biomimetic process, Thermochimica Acta. 280–281 (1996) 479–490. doi:10.1016/0040-6031(95)02784-X.

[165] J.Y. Martin, Z. Schwartz, T.W. Hummert, D.M. Schraub, J. Simpson, J. Lankford, D.D. Dean, D.L. Cochran, B.D. Boyan, Effect of titanium surface roughness on proliferation, differentiation, and protein synthesis of human osteoblast-like cells (MG63), Journal of Biomedical Materials Research. 29 (1995) 389–401. doi:10.1002/jbm.820290314.

[166] K.E.M. Benders, P.R. van Weeren, S.F. Badylak, D.B.F. Saris, W.J.A. Dhert, J. Malda, Extracellular matrix scaffolds for cartilage and bone regeneration, Trends in Biotechnology. 31 (2013) 169–176. doi:10.1016/j.tibtech.2012.12.004.

[167] S.F. El-Amin, H.H. Lu, Y. Khan, J. Burems, J. Mitchell, R.S. Tuan, C.T. Laurencin, Extracellular matrix production by human osteoblasts cultured on biodegradable polymers applicable for tissue engineering, Biomaterials. 24 (2003) 1213–1221.

doi:10.1016/S0142-9612(02)00451-9.

[168] C.J.C. Fernandes, F. Bezerra, M.R. Ferreira, A.F.C. Andrade, T.S. Pinto, W.F. Zambuzzi, Nano hydroxyapatite-blasted titanium surface creates a biointerface able to govern Src-dependent osteoblast metabolism as prerequisite to ECM remodeling, Colloids and Surfaces B: Biointerfaces. 163 (2018) 321–328. doi:10.1016/j.colsurfb.2017.12.049.

[169] O.G. Davies, S.C. Cox, R.L. Williams, D. Tsaroucha, R.M. Dorrepaal, M.P. Lewis, L.M. Grover, Annexin-enriched osteoblast-derived vesicles act as an extracellular site of mineral nucleation within developing stem cell cultures, Scientific Reports. 7 (2017) 1–13. doi:10.1038/s41598-017-13027-6.

[170] R. Megat Abdul Wahab, N.A. Mohamed Rozali, S. Senafi, I.Z. Zainol Abidin, Z. Zainal Ariffin, S.H. Zainal Ariffin, Impact of isolation method on doubling time and the quality of chondrocyte and osteoblast differentiated from murine dental pulp stem cells, PeerJ. 5 (2017) e3180. doi:10.7717/peerj.3180.

[171] W. Zhang, Z.L. Huang, S.S. Liao, F.Z. Cui, Nucleation sites of calcium phosphate crystals during collagen mineralization, Journal of the American Ceramic Society. 86 (2003) 1052–1054. doi:10.1111/j.1151-2916.2003.tb03422.x.